Thesis

Doctor of Philosophy

Solid State Batteries: Materials and Interfaces

POOJA VADHVA

ACADEMIC SUPERVISORS

DR. ALEXANDER J. E. RETTIE

PROF. PAUL R. SHEARING

Submitted in part fulfilment of the requirements for the degree of Doctor of Philosophy

2023

Electrochemical Innovation Lab
Department of Chemical Engineering
Torrington Place, London, WC1E 7JE

Declaration

I, *Pooja Vadhva*, confirm that the work presented in this thesis is my own. Where information has been derived from other sources, I confirm that this has been indicated in the thesis.

Signature

26/05/2023…….

Date

Acknowledgements

I would like to express my gratitude and warmest thanks to my supervisor, Alex Rettie, for his continued support, supervision, interesting battery discussions, and knowledge in the field of electrochemistry. His attention to detail, vast knowledge and encouraging feedback has been highly influential in shaping me into the researcher I am today. I would also like to thank my secondary supervisor, Paul Shearing, for his support, guidance, and breadth of wisdom in energy storage systems. Additionally, I would like to thank my acting supervisor at Imperial College London, Gregory Offer, for his guidance and for making me continually analyse and critique my work in the pursuit of high-quality academic research. I am also grateful to Anisha Patel for her mentorship and helping to familiarise me with the experimental methods and procedures at Imperial College London. I would also like to extend my thanks to Toby Neville for laboratory training at UCL and the Engineering and Physical Sciences Research Council (EPSRC) for funding acquisition and industry collaborators, for their solid-state battery cells and useful industry advice during catch-up meetings. I would also like to express special thanks to Ann-Christin Dippel, the beamline scientist at the German Synchrotron for her guidance and positive feedback.

I would like to express my sincerest thanks to Adam Boyce, for his mechanical knowledge and mentorship, without which the modelling efforts in this thesis would not possible. I am eternally grateful to Mei-Chin Pang for her efforts to foster a collaboration with Imperial and continuous guidance despite graduating with her PhD and moving into industry. I am particularly grateful to Marco Siniscalchi for his help in setting up and using the Li deposition equipment at Oxford and Sudarshan Narayanan for his in-situ XPS data collection and assistance. I am indebted to Thomas Gill, who helped conduct thin film testing whilst I was on an internship at Tesla. I would like to express my thanks to others within the research group especially Joshua Cruddos, Samia Said, Ji Hui, Michael Johnson, Joshua

Bailey, Jen Hack and Roby Soni for their help and support in the labs at UCL. Equally, at Imperial, I would like to thank Alastair Hale for his help on pulse power data extraction and Gavin White for moral support in the labs. I am indebted to the humor, coffee conversations, practical advice, and friendship bestowed upon me by these individuals: Mateen Mirza, Alex Dimitri, Francesco Iacoviello, Elias Galiounas, Tom Heenan and Nicholas Yiu. Additionally, I would like to thank all the academic and departmental members of the Electrochemical Innovation Lab (EIL) at UCL, with particular thanks to Tom Miller, Rhod Jervis and Claire Saunders for their encouragement and support.

I would like to thank my close friends in particular Ting Chang, outside of my PhD environment as well as Ed Brook and Elliot Heather for their neighbourly conversations, patience and encouragement throughout the COVID-19 pandemic which helped to keep me sane and positive. I would be remiss if I didn't acknowledge my team members and technicians at Tesla who supported my PhD commitments such as meetings and in attending an international conference presenting my PhD work, whilst working for the cell engineering team as an intern. The impact of coffee on my thesis should not be left out and my love for Muay Thai and martial arts which helped to release my PhD frustrations. Finally, I would like to thank my loving family in particular my mother, Mukta Vadhva, whose constant support, love and guidance has made writing this thesis possible, she has always inspired and motivated to do my best, and my loving fiancée Robert Cushworth for his feedback, listening to me incessantly talking about my battery research and for his affection. I dedicate this PhD thesis to my mother, who taught me to always pursue my passion.

UCL Research Paper Declaration Forms

1. For a research manuscript that has already been published (if not yet published, please skip to section 2)**:**		
a) Where was the work published? (e.g. journal name)	ChemElectroChem	
b) Who published the work?	Chemistry Europe	
c) When was the work published?	08/04/2021	
d) Was the work subject to academic peer review?	Yes	
e) Have you retained the copyright for the work?	Yes	
[If no, please seek permission from the relevant publisher and check the box next to the below statement]: ☒ *I acknowledge permission of the publisher named under 1b to include in this thesis portions of the publication named as included in 1a.*		
2. For a research manuscript prepared for publication but that has not yet been published (if already published, please skip to section 3)**:**		
a) Has the manuscript been uploaded to a preprint server? (e.g. medRxiv):	No	
b) Where is the work intended to be published?	Click or tap here to enter text.	
c) List the manuscript's authors in the intended authorship order:	Click or tap here to enter text.	
d) Stage of publication	Please select.	
3. For multi-authored work, please give a statement of contribution covering all authors (if single-author, please skip to section 4**):**		
Vadhva, P.; Hu, J.; Johnson, M. J.; **Contributed equally to this work: Investigation, Visualisation, Conceptualisation, Formal analysis, Writing – Original Draft and Review & Editing**. Stocker, R. - Formal analysis, Review & Editing; Braglia, M.- Formal analysis, Review & Editing; Brett, D. J. L.- Funding acquisition, Formal analysis, Review & Editing; Rettie, A. J. E. - Supervision, Funding acquisition, Formal analysis, Writing – Review & Editing.		
4. In which chapter(s) of your thesis can this material be found?		
Chapter 2 (section 2.2.2 Electrochemical Impedance Spectroscopy)		
5. e-Signatures confirming that the information above is accurate (this form should be co-signed by the supervisor/ senior author unless this is not appropriate, e.g. if the paper was a single-author work):		

Candidate:	Pooja Vadhva	**Date:**	18/04/2023
Supervisor/ Senior Author	Alex Rettie	**Date:**	26/05/2023

1. For a research manuscript that has already been published (if not yet published, please skip to section 2)**:**			
a) Where was the work published? (e.g. journal name)	Journal of Electrochemical Society		
b) Who published the work? (e.g. Elsevier/Oxford University Press):	Electrochemical Society		
c) When was the work published?	19/10/2022		
d) Was the work subject to academic peer review?	Yes		
e) Have you retained the copyright for the work?	Yes		
[If no, please seek permission from the relevant publisher and check the box next to the below statement]: ☒ *I acknowledge permission of the publisher named under 1b to include in this thesis portions of the publication named as included in 1a.*			
2. For a research manuscript prepared for publication but that has not yet been published (if already published, please skip to section 3)**:**			
a) Has the manuscript been uploaded to a preprint server? (e.g. medRxiv):	Yes	Ecsarxiv	
b) Where is the work intended to be published?			
c) List the manuscript's authors in the intended authorship order:	.		
d) Stage of publication	Please select.		
3. For multi-authored work, please give a statement of contribution covering all authors (if single-author, please skip to section 4**):**			
The model equations and implementation into COMSOL Software was carried out equally by A. Boyce **and P. Vadhva.** Pulse testing and equivalent circuit modelling was conducted by **P. Vadhva** using code written by R. Tomlin and RC parameters extracted by A. Hales. All other experimental testing and analysis was carried out by **P. Vadhva** with assistance from A. Patel and initial project guidance from M. Pang. Funding acquisition and project supervision by P. Shearing, G. Offer and A. Rettie.			
4. In which chapter(s) of your thesis can this material be found?			
Chapter 3			
5. e-Signatures confirming that the information above is accurate (this form should be co-signed by the supervisor/ senior author unless this is not appropriate, e.g. if the paper was a single-author work):			
Candidate:	Pooja Vadhva	**Date:**	18/04/2023
Supervisor/ Senior Author	Alex Rettie	**Date:**	26/05/2023

1. For a research manuscript that has already been published (if not yet published, please skip to section 2)**:**		
a) Where was the work published? (e.g. journal name)	Chemistry of Materials	
b) Who published the work? (e.g. Elsevier/Oxford University Press):	American Chemical Society	
c) When was the work published?	18/01/2023	
d) Was the work subject to academic peer review?	Yes	
e) Have you retained the copyright for the work?	Yes	
[If no, please seek permission from the relevant publisher and check the box next to the below statement]: ☒ *I acknowledge permission of the publisher named under 1b to include in this thesis portions of the publication named as included in 1a.*		
2. For a research manuscript prepared for publication but that has not yet been published (if already published, please skip to section 3)**:**		
a) Has the manuscript been uploaded to a preprint server? (e.g. medRxiv):	Yes	ChemRxiv
b) Where is the work intended to be published?		
c) List the manuscript's authors in the intended authorship order:		
d) Stage of publication	Please select.	
3. For multi-authored work, please give a statement of contribution covering all authors (if single-author, please skip to section 4**):**		
Experimental characterisation and analysis was carried out by **P. Vadhva** with help from S. Said on AFM testing and S. Narayanan on in-situ XPS. In addition, Li deposition training and testing was carried out by M. Siniscalchi, in conjunction with **P. Vadhva**. Assistance in film synthesis and electrochemical testing on the phase space of LAPO, was supported by T. Gill and J. Cruddos. Funding acquisition and project supervision by A. Rettie, M. Pasta and T. Miller.		
4. In which chapter(s) of your thesis can this material be found?		
Chapter 5		
5. e-Signatures confirming that the information above is accurate (this form should be co-signed by the supervisor/ senior author unless this is not appropriate, e.g. if the paper was a single-author work):		

Candidate:	Pooja Vadhva	**Date:**	18/04/2023
Supervisor/ Senior Author	Alex Rettie	**Date:**	26/05/2023

1. For a research manuscript that has already been published (if not yet published, please skip to section 2)**:**		
f) Where was the work published? (e.g. journal name)		
g) Who published the work? (e.g. Elsevier/Oxford University Press):		
h) When was the work published?		
i) Was the work subject to academic peer review?		
j) Have you retained the copyright for the work?		
[If no, please seek permission from the relevant publisher and check the box next to the below statement]: ☐ *I acknowledge permission of the publisher named under 1b to include in this thesis portions of the publication named as included in 1a.*		
2. For a research manuscript prepared for publication but that has not yet been published (if already published, please skip to section 3)**:**		
e) Has the manuscript been uploaded to a preprint server? (e.g. medRxiv):	Yes	ChemRxiv
f) Where is the work intended to be published?	Applied Materials and Interfaces	
g) List the manuscript's authors in the intended authorship order:	Pooja Vadhva, Adam M. Boyce, Paul R. Shearing, Gregory Offer, Anisha N. Patel, Alexander J. E. Rettie	
h) Stage of publication	Submitted (09/05/2023)	
3. For multi-authored work, please give a statement of contribution covering all authors (if single-author, please skip to section 4**):**		
Model simulations and data analysis was conducted by **P. Vadhva** with advice and direction from A. Boyce, G. Offer and A. Patel. Funding acquisition by A. Rettie and P. Shearing.		
4. In which chapter(s) of your thesis can this material be found?		
Chapter 4		
5. e-Signatures confirming that the information above is accurate (this form should be co-signed by the supervisor/ senior author unless this is not appropriate, e.g. if the paper was a single-author work):		

Candidate:	Pooja Vadhva	**Date:**	18/04/2023
Supervisor/ Senior Author	Alex Rettie	**Date:**	26/05/2023

Abstract

In recent years, solid-state batteries (SSBs) have garnered not only academic research attention but also of that of the electric vehicle (EV) and consumer electronics industry. The use of a solid electrolyte (SE) in a SSB, in place of the flammable liquid electrolyte (LE) used in conventional lithium-ion batteries (LIBs) could result in improved safety. Additionally, SSBs are promising alternatives to the incumbent LIB which contains a LE, due to their higher energy densities by pairing the SE with lithium (Li) or silicon (Si) negative electrodes (NEs). These offer a $\approx 10x$ theoretical energy density compared to the graphite NE used in LIBs. However, SSBs are plagued by a unique set of challenges which must be overcome to enable the widespread adoption of this technology: solid-solid interfaces which are highly resistive, slow kinetics, and the formation of interfacial voids leading to Li penetration, which ultimately results in capacity loss and low cycle life.

In this work, electrochemical testing, physical characterisation and an electro-chemo-mechanical (echem-mech) model is used to investigate and analyse the solid-solid interface, predominantly at the NE|SE interface. First, experimental testing of a commercial thin film Si based SSB is used to parameterise and validate an echem-mech model at the continuum level. Then, the validated model is used to explore the interplay between electrochemistry and mechanics by probing the relationship and between C-rate, applied pressure and capacity on the stress-strain response of the cell. Complex evolution of concentration gradients at high C-rates is found to influence the internal stresses and could point towards sites for fracture propagation within the electrode. Finally, this thesis addresses a key shortcoming of lithium phosphorus oxynitride (LiPON) SE - the requirement for vacuum deposition techniques, to a new non-crystalline (NC) material albeit synthesised using scalable processing methods. Electrochemical testing and physical

characterisation of this material $Li_{2.8}AlP_{1.25}O_x$ (LAPO) and its stability against Li-metal for use in an "anode-free" battery is explored. The methods and characterisation tools presented in this thesis are designed so that they can be implemented for future testing across different SE battery systems.

Impact Statement

Transitioning global dependence on fossil-fuel energy to sustainable energy systems is paramount in our current climate. There is a pressing need for advanced energy storage and technologies such as SSBs are highly promising due to their higher energy densities through the use of a high specific capacity NE (e.g., Li) than the incumbent lithium-ion batteries which commonly employ a graphite NE. The commercialisation of large-format SSBs and demonstration in grid storage or as a power source for EVs has not yet been demonstrated. The challenges surrounding the solid-solid resistive interfaces, sluggish Li^+ ion transport and large strains in the SSBs must be addressed to help the development of this technology.

This research aims to provide insight into the high SSB interfacial resistances using a suite of electrochemical techniques which is not routine for SSBs. These techniques can be applied to a wide range of SE chemistries and SSB configurations. It is intended that the research output from this thesis will garner further interest in SSBs and highlight the challenges and potential solutions to improve the cell cycle life by reducing the stress-strain response within the SSB, for example by altering electrode thickness and SE material properties. It is envisioned that this thesis will help to motivate future research on NC SE materials due to their desirable mechanical and electrochemical properties. This research is anticipated to be of interest to researchers not only in academia but also industry companies that are trying to manufacture large-format SSBs for EVs. In addition, it is hoped that governmental bodies will find this thesis useful as it focusses on scalable and low-cost synthesis of SE materials.

During this PhD research, a strong collaboration was formed between University College London (UCL), Imperial College London and a UK battery manufacturer of SSBs with success of this project leading to a government grant from Innovate UK to continue further research in this area. The project focus was on the company's thin film SSB technology which is used in medical devices and learnings from the simulated model will help when designing thin film SSBs for

optimal stress-strain response. The funding will enable work on the company's large format SSBs to help the scale-up of these cells for use in EVs. In addition to this work, a low-cost, scalable and novel SE material was synthesised, LAPO which has the potential to be used in an "anode-free" configuration for use in advanced battery systems. Not only is the synthesis method extremely low cost, the mechanical and electrochemical properties are highly desirable, with work in this area being awarded additional funding to enable more researchers to continue to scale-up this material and demonstrate superior performance at a device level. A patent has been filed for this SE with the hope of more SE materials in this phase space to be discovered and subsequently patented.

The work in this thesis has been published in leading academic journals and presented at national and international conferences which has garnered interest in the academic community. The author has been a recipient of multiple awards to support their research and to help with travel to international conferences to present their work. The author is a battery enthusiast, engaging in battery networks such as battery brunch where they have led virtual meeting rooms to facilitate discussion on advanced battery systems. Additionally, the author is a battery consultant for Intercalation Station and a battery ambassador at Battery Associates, promoting battery research to the scientific and business community and the public. The author also engages with the public via the student-led research society, UCELL, where they have engaged with primary and secondary school members, champion women in STEM, promote sustainability and discuss the importance of shifting away from fossil fuel reliance. The author is a keen activist for climate change and has run a half marathon (London Half Parks Marathon 2021) to raise money for world wildlife fund (WWF) to help climate solutions and raise awareness.

Contents Page

List of Figures

List of Tables

Nomenclature

Abbreviation Definitions

SSB	Solid state battery
LIB	Lithium-ion battery
SE	Solid electrolyte
PE	Positive electrode
NE	Negative electrode
Li	Lithium metal
Si	Silicon
***a*-Si**	Amorphous Silicon
NC	Non-crystalline
XRD	X-ray diffraction
SEM	Scanning electron microscopy

XPS	X-ray photoelectron spectroscopy
LFP	Lithium iron phosphate
NMC	Lithium nickel manganese cobalt oxide
LMO	Lithium manganese oxide
EIS	Electrochemical impedance spectroscopy
EDX	Energy dispersive X-ray spectroscopy
AC/ DC	Alternating/ direct current
LLZTO	Lithium lanthanum zirconium tantalum oxide, $Li_{6.4}La_3Zr_{1.4}Ta_{0.6}O_{12}$
LPSCl	Lithium phosphorus sulfur chloride, Li_6PS_5Cl
LCO	Lithium cobalt oxide, $LiCoO_2$
LiPON	Lithium phosphorous oxynitride
R_{ct}	Charge transfer resistance
R_b	Bulk resistance
W	Warburg diffusion

CPE	Constant phase element
C	Capacitor
R	Resistor
GI-XTS	Grazing incidence X-ray total scattering
Echem-mech	Electro-chemo-mechanical
OCV	Open circuit voltage
GITT	Galvanostatic intermittent titration technique
SoC/SOC	State of charge
PEIS	Potentiostatic electrochemical impedance spectroscopy
AFM	Atomic force microscopy
HPPC	Hybrid pulse power characterisation
DRT	Distributed relaxation time
Li^+ ion /Li^+	Lithium ion
RT	Room temperature

Chapter 1

Introduction

1.1 The Lithium-ion Battery

The discovery of intercalation electrodes in 1970s[1] by Stanley Whittingham led to the creation of the first rechargeable lithium-ion battery (LIB) consisting of a lithium disulfide positive electrode (PE) and lithium-aluminum NE. However, it was not until the 1980s with the substitution of lithium cobalt oxide (LCO) as the PE, was the modern LIB discovered. Following this, LIBs were prototyped with LCO PE and a graphite NE due to safety concerns surrounding the highly reactive nature of lithium metal in conjunction with a flammable organic LE. In 1991, Sony commercialised the first LIB[2] using the graphite NE pioneered by Akira Yoshino in combination with LCO PE discovered by John Goodenough. Despite this historic achievement it was not until much later that Yoshino, Goodenough and Whittingham won the Nobel prize in Chemistry in 2019. Their research contributions have laid the foundations toward a green economy, without which the electrification of transport or energy storage would not be possible. Moving to the

present day, the LIB industry is highly profitable, and LIBs are used globally and in a wide range of applications such as grid storage, portable electronics, and electric vehicles (EVs).

Although LCO was used in the earliest LIBs as the PE, recent focus has shifted away from using expensive and unethically mined cobalt to include lithium iron phosphate (LFP), lithium nickel manganese cobalt oxide (NMC) with reduced ratios of cobalt and lithium manganese oxide (LMO). In a conventional LIB, the PE and NE electrodes are at opposite ends of the battery with metallic current collectors (CCs) either side to allow electrons to flow in an out of the system via an external circuit. The active material within the electrodes is commonly mixed with a binder to keep the particles in contact with one another and a conductive carbon network which provides electrical charge extraction. The battery is filled with a LE which allows the movement of lithium ions (Li^+ ions) through the battery to lithiate (or de-lithiate) the electrodes during cell cycling. The most common LE consist of fluorinated salts dissolved in organic solvents such as ethylene carbonate. A solid electrolyte interface (SEI) layer can build up on the NE, known as a cathode electrolyte interface (CEI) on the PE. This layer occurs due to LE decomposition and can act as a passivation layer by blocking electron transport thereby preventing further decomposition and only allowing the movement of Li^+ ions. However, the formed SEI/CEI can be highly resistive, and might not be stable hence impacting the cyclability and performance of the LIB. A polymeric separator is placed between the electrodes to prevent build-up of metallic lithium from one electrode to another causing the battery to short-circuit and fail.

During the charging process, an electrical potential is applied via the external circuit which causes electrons to from the PE to the NE, via this external circuit. Oxidation (loss of electrons) at the PE occurs causing Li^+ ions to be liberated (Li oxidation state changes from 0 to +1). To counteract the charge imbalance posed by the movement of electrons, the positively charged Li^+ ions move from the PE through the electrolyte and are reduced (gain of electrons) at the NE (Figure 1.1). The reverse of this occurs during discharge, whereby the potential difference between the PE and NE drives a spontaneous redox reaction (Gibbs free energy is

negative) at the electrodes. This spontaneous redox reaction can occur due to the NE being at a higher potential than the PE. Therefore, oxidation now occurs at the NE and reduction occurs at the PE. Li^+ ions migrate through the electrolyte from the NE to the PE. Electrons flow via the external circuit from the NE to the PE providing an electric current which can be used to power a device. The half-cell and full cell reactions are displayed for a graphite NE and LCO PE system:

NE half reaction $\quad LiC_{6\,(s)} \rightleftharpoons C_{6\,(s)} + Li^+ + e^-$

PE half reaction $\quad CoO_{2\,(s)} + Li^+ + e^- \leftrightharpoons LiCoO_{2\,(s)}$

Full cell reaction $\quad LiC_{6\,(s)} + CoO_{2\,(s)} \leftrightharpoons C_{6\,(s)} + LiCoO_{2\,(s)}$

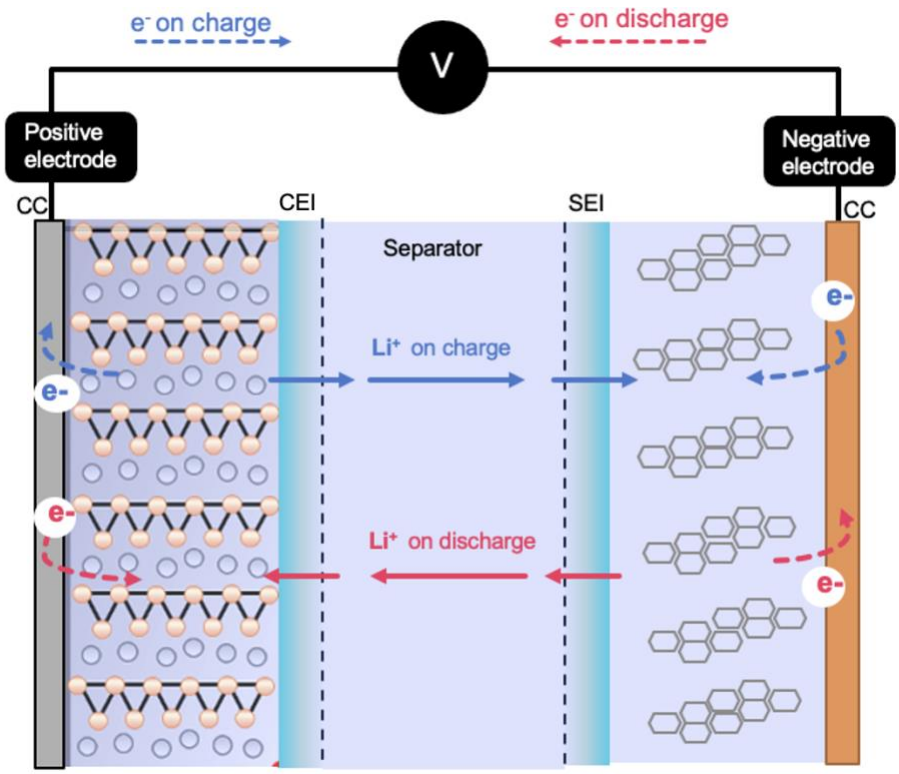

Figure 1.1 Illustration of the migration of Li^+ ions and electrons during charge and discharge in a LIB.

Research towards optimising and discovering electrodes with earth-abundant materials is ongoing, with the goal of improving energy density and safety due to the flammable nature of LEs used. In addition, there is an effort towards replacing

the LE with a non-flammable SE which provides the subject area of this thesis. SEs can provide an advantage in terms of energy density by enabling a Li metal or Li alloy NE.

The energy density of a battery can be expressed by:

$$E_{grav} = C_{grav}\,\Delta V \tag{1.1}$$

$$where, \qquad C_{grav} = \frac{zF}{3600 \times M_{AM}} \tag{1.2}$$

where E_{grav} is the gravimetric energy density [Wh kg^{-1}], C is the gravimetric capacity which is the charge that can be stored per unit mass [Ah kg^{-1}], ΔV is the cell voltage [V] which is the difference in chemical potential between the NE and PE, including any overpotentials (voltage losses) and M_{AM} is the active material molar mass of the electrode [kg mol^{-1}]. The gravimetric capacity can be expressed as the product of the Faraday's constant, $F = 96\,485$ [C mol^{-1}] and the number of charges which are involved in the redox reaction, z. As the capacity in battery applications is commonly expressed in units of mAh, the Faraday constant is divided by 3600, $F/3600$ = 26.801 [Ah mol^{-1}].

Similarly, the volumetric energy density, E_{vol} [Wh L^{-1}] can be expressed as:

$$E_{vol} = C_{vol}\Delta V \tag{1.3}$$

$$where, \qquad C_{vol} = \frac{zF\rho_{AM}}{3.6 \times M_{AM}} \tag{1.4}$$

the volumetric capacity C_{vol} [Ah L^{-1}] is expressed in terms of the active material density, ρ_{AM} [kg m^{-3}].

The active material specific capacity directly influences the energy density as well as the cell voltage ΔV. Since the cell voltage depends on the chemical potential between the NE and PE, a wide electrochemical window between the two electrodes is beneficial as well as reducing overpotentials (voltage losses). These overpotentials can be due to ohmic losses from ionic and electronic resistances in the electrode and electrolyte, kinetic losses due to charge transfer resistance at the electrode interface and transport losses due to charge diffusion.

As there is an increasing need for energy storage devices to electrify transport and enable green energy to mitigate climate change and combat air pollution, it is paramount to concentrate research efforts into the discovery of materials that will enable batteries with higher capacities. Current LIB technology has reached its maturity in that it is limited in enabling higher energy density electrodes due to the narrow electrochemical stability of the employed LE. Therefore, advancements in batteries are sorely needed and a potentially promising advanced battery system: the all SSB, will be discussed in the next section.

1.2 All-Solid-State Battery

SSBs are analogous to conventional Li-ion batteries in that they have an NE (preferably Li metal or Li metal alloy such as Si) and a PE, however instead of having a LE they use a SE. There is also the matter of the separator which in conventional LIBs consists of a porous material through which the LE propagates. In a SSB the SE assumes the role of the separator [3] as illustrated in Figure 1.2 by Janek and Zeier[3] when Li metal is used as the NE with a SE and PE composite (PE powder mixed with SE), the volumetric and gravimetric energy density is increased by 70% and 40% respectively, compared to a LIB. If a graphite NE is used instead, there is 0% and -10% increase in the volumetric and gravimetric respectively.[3] The reason for the reduction in gravimetric energy density in the graphite NE system compared to a LIB is due to the additional weight of the SE (compared to a LE) which does not contribute to the cell's overall energy density.

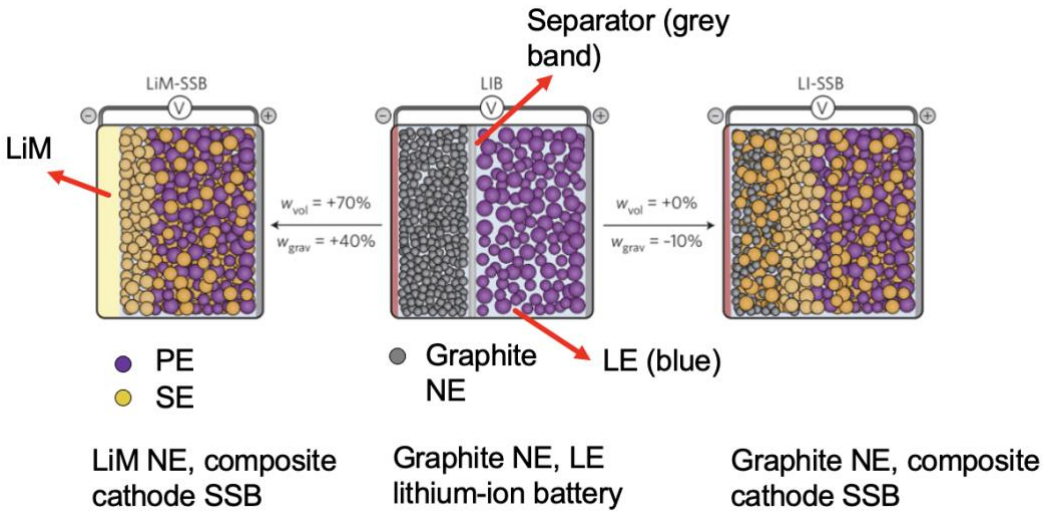

Figure 1.2 SSB diagram on the left-hand side with Li metal (LiM as light-yellow band) and a PE indicated as purple circles mixed with SE particles (dark yellow circles). W_{vol} and W_{grav} represent volumetric and gravimetric energy densities of the battery. A conventional LIB (middle diagram) contains a LE (light blue) with a thin separator (grey band) paired with a graphite NE (grey circles), whereas in the two solid state cells, the SE assumes the role of the separator. The diagram on the right-hand side displays a composite PE SSB paired with a graphite NE. Reprinted with permission from ref.[3]

As displayed in Figure 1.2, the key benefit of incorporating a SE in a SSB is to enable a Li metal electrode. This is because metallic Li has a 10*x* theoretical specific capacity (3860 mAh g^{-1}) compared with a conventional graphite NE (372 mAh g^{-1}). To realise a metallic Li electrode, the electrolyte instability against Li metal must be overcome and conventional LEs are not electrochemically stable against Li. There is a plethora of research,[4–7] material synthesis and on-going elementary understanding to try to comprehend the mechanisms that reduce the chemical instability with a Li metal NE.[8] It is thought that SEs can enable the safe operation of a Li metal NE as many have a larger electrochemical window than LEs, although issues around the Li|SE interfacial stability remain a challenge. The instability against Li often leads to SE decomposition which results in capacity loss. Li dendrites (metallic Li filaments) can grow within SE voids or grain boundaries, accelerating capacity fade. Si is a Li metal alloy and another candidate when considering high energy density NEs without the issue of dendrite formation.

However, Si electrodes exhibit a large volumetric expansion ≈300-400%[9] during (de)lithiation which reduces its capacity and cycle life. In a LIB, the large Si expansion pulverises the SEI which results in further electrolyte decomposition over subsequent cycles and a stable SEI is not able to form, severely limiting the capacity and cycle life. As a result, Si stability issues mainly arise from the LE interface, and it is thought that the mechanical integrity of a SE can limit the Si expansion and enable steady operation by forming a more mechanically stable interface at the Si|SE.

1.3 Introduction to Silicon Electrodes

Si is relatively more abundant than Li metal, easier to manufacture roll-to-roll, does not require moisture-free processing whilst exhibiting a similar specific capacity to Li (>3500 mAh g^{-1} for $Li_{3.75}Si$) and therefore could be an alternate cost-effective NE. However, this does not resolve the issue of electrochemical and mechanical degradation, which is augmented by Si's high volumetric expansion (as much as 300-400%) upon (de)lithiation. During solid-state cycling, these large volumetric changes can induce mechanical stresses within the SSB components, resulting in mechanical degradation, active material delamination and fracture.[10–13] Therefore control of the Si|SE interface is critical to prevent delamination between the Si and SE.

There is evidence that pairing a SE with Si could be beneficial when suppressing Si expansion compared to a LE as demonstrated by Ping et al.[9] using an oxide-based SE, attributing the lower Si volumetric expansion to the mechanical rigidity of the SE. Furthermore, a stable interphase at the SE|Si interface could be formed, which has recently been achieved by Tan et al.[14] using a sulfide SE with a composite PE (NMC), with over 500 cycles[14]. They attributed the high cycle life to the removal of carbon from Si and the porous structure of the delithiated Li-Si alloy which prevents delamination from the SE matrix. Their study concluded possible plastic deformation of Li-Si under 50 MPa applied stack pressure, which helps to maintain contact with the SE. At lower stack pressures, the cell exhibited lower

discharge capacity likely due to the poor contact between the Li-Si and the SE, resulting in increased cell impedance and polarisation.

This opens room for SE material design when paired with a Si electrode rather than Li for which there are very few SEs that are chemically stable. Sulfide SEs, for example, can be more easily integrated in a PE composite forming a much lower impedance than oxide SEs. Furthermore, sulfide SE materials can be employed directly against Si which would not be possible for a Li NE without the addition of coatings or buffer layers to prevent continuous decomposition. The role of plastic deformation and applied pressure is important for SSB systems which can be probed using physical models to understand the material deformation and stress-strain build up. The ranges of SE mechanical properties are displayed in Table 1.1, with focus on common inorganic SEs: crystalline sulfides/oxides and amorphous or NC sulfides/oxides. The Young's modulus gives an idea of how easily a material can be stretched or deformed and is defined as the ratio of tensile stress to tensile strain. The stress is the applied force over a given material area and the strain is the extension of the material as a result of the stress, divided by the original material length. The stress can be tensile in nature if the material is being elongated and compressive if the material is being compressed (shortened). Tensile stresses are positive, whilst compressive stresses are negative. The yield strength is defined as the maximum stress a material will undergo before plastic deformation begins whilst the Poisson's ratio is the material deformation perpendicular to the loading direction and is described as the negative ratio of the lateral strain to axial strain.

Table 1.1 *Ranges of inorganic SE mechanical properties, at room temperature*

SE material	***Crystalline sulfides***	***Crystalline oxides***	***Amorphous oxide (e.g., LiPON)***	***Amorphous sulfide (e.g., Li_2S-P_2S_5)***
Young's modulus (GPa)	~ 15-25 [136]	~ 80-200 [136]	~ 50-80 [136]	~ 10-18 [15]

Yield's strength (GPa)	~ 0.3-0.7 [136]	~ 2-5 [136]	~ 1-2 [136]	~ 0.4 – 0.6 [15]
Poisson's ratio	~ 0.27- 0.35 [16]	~ 0.25 –0.28 [16]	~ 0.27 [16]	~ 0.3 [15]

A detailed discussion into different SEs which can enable a Li or Si NE will be reviewed in this work, in addition to the interfacial stability at the NE|SE interface. Electrochemical techniques such as electrochemical impedance spectroscopy (EIS) can be used to study the different electrochemical processes occurring at this interface as well as validate SSB physical models. These electro-chemo-mechanical (echem-mech) models can provide an insight into the electrochemistry and mechanics occurring at the interface and how they influence each another. An emerging class of SEs which are promising candidates due to their stability against Li metal, will be explored. They are non-crystalline (NC) in nature and their local structure is believed to play an important role in their ionic conductivity.

1.4 Thesis Goals and Structure

From the extensive research discussed in the previous sections, to enable adoption of SSBs several challenges need to be appropriately addressed. To ensure successful SSB commercialisation, improving the high interfacial impedance at the SE|electrode, is of great importance.[17] In order to exceed the LIB gravimetric energy density on a cell and module level, pairing the SE with a high energy density NE (Li or Li alloy material such as Si) and stack pressure needs to be carefully tuned. Maintaining a degree of pressure on SSB systems is vital for improved contact between the solid-solid interfaces and too high a stack pressure is unfeasible for practical applications. Other challenges include improvement in manufacturing and scaling of SEs and composite electrodes. This thesis looks to address some of these challenges and whilst large scale manufacturing processes is out of the scope

of this thesis, it does include synthesis of a NC SE produced using scalable methods.

Chapter 3 lays the foundations of probing the solid-solid interfaces in a commercial thin film SSB using an assortment of electrochemical techniques: differential capacity analysis, EIS, distributed relaxation times (DRT), galvanostatic intermittent titration technique (GITT) and hybrid pulse power characterisation (HPPC). An echem-mech model is created and validated using parameters from the experimental data. The thin film SSB consists of an amorphous Si NE, a LiPON SE and LCO PE.

Following the validation of the echem-mech model, Chapter 4 builds on the model results and investigates the effect of applied pressure and C-rate on the SSB performance. Electrochemical factors such as Si diffusion as well as mechanical properties of the Si and different SEs chemistries are probed. Their influence on the SSB voltage profile, concentration gradients and stress-strain response are analysed. Maximum principal stress and strains are observed at the SE|NE boundary which is used to generate a map of stress and strain as a function of C-rate and applied pressure. The SE material is altered to study the effect of the SE mechanical properties on the SSB response. Three different SE material are chosen: a NC SE LiPON, a sulfide SE and an oxide SE which have a differing Young's Moduli and yield strengths. Optimised SEs with desirable mechanical properties to reduce the maximum principal stress in the Si and SE is reported.

Chapter 5 looks beyond LiPON towards another NC material which can be engineered using scalable solution-based methods. In this work, a scalable SE is optimised with the highest ionic conductivity of a lithium aluminophosphate NC, LAPO, and the structure-conductivity relationship investigated. Further, chemical and electrochemical measurements are conducted on LAPO to reveal its electronic conductivity, Young's modulus, activation energy, surface roughness and chemical composition. LAPO's stability with Li metal is probed using in-situ X-ray photoelectron spectroscopy (XPS) and a stable passivation layer found to occur at the interface.

A summary of the key objectives of each chapter (Chapter 3-5) is outlined:

1. Chapter 3: experimentally validate an echem-mech model under dynamic operating conditions and use the model to probe the stress-strain response on altering cell design, e.g., electrode thickness.
2. Chapter 4: use the validated model (in Chapter 3) to understand the interplay between the electrochemistry and mechanics in the SSB domains. Focus on the build-up of concentration gradients, stress-strain and averaged cell capacity as applied pressure and C-rate are varied. Understand how the SE material properties influence the cell stress-strain response.
3. Chapter 5: address a key shortcoming of LiPON, the SE used in the commercial SSB, which uses slow and expensive deposition techniques to a new SE that can be synthesised using low cost and more scalable methods.

Electrochemical and modelling techniques are brought together in this thesis to probe the SE|NE interface. Initially, a Si NE is deployed in a commercial thin film SSB which is then extended to a scalable NC SE (LAPO). The properties and local structure of LAPO is probed and contrasted with LiPON SE which is used in the earlier study. LAPO's stability with Li metal is compared, with potential use as a NE or PE passivation layer to enable stable plating and stripping of Li in a SSB or LE system. The interplay of externally applied pressure and electrochemical stability at the SE|NE interface is used to provide an outlook for the desired electrochemical and mechanical properties of a scalable SE.

The next chapter presents a literature review on Si based SSB echem-mech models, different classes of SEs, instability at the electrode interfaces, and overall SSB cell design including stack pressure consideration. First, Section 2.1 discusses electrochemical mechanical models that can be used to understand the processes occurring within SSBs especially at the NE and SE interface. The following section delves into state-of-the-art SEs which are promising candidates to enable a high energy density NE. Their ionic conduction mechanisms and structure properties are discussed, which is important in permitting fast reaction kinetics through the SSB.

Next, studies on the solid-solid interface at the respective electrodes are reviewed as well as techniques such as EIS which can help to probe these interfaces, with a focus in literature on the NE|SE interface. Finally, effect of applied pressure to reduce volumetric expansion of SSB cells with Li or Li alloy containing NEs is studied (Section 2.4).

Chapter 2

Literature Review

2.1 Electro-chemo-mechanical Models

The electrochemical behaviour of SSBs is hard to examine using experimental techniques such as EIS (Section 2.3.2) alone due to the convolution of processes occurring within the solid-state cell. The solid-solid interfaces are extremely difficult to probe under cell operation using non-desctructive experimental techniques and yet the high interfacial impedance at the electrode and SE interface is one of the main challenges limiting the commercialisation of SSBs.[18–21] Electrochemical models within a finite element framework, such as COMSOL Multiphysics, can probe the behaviour of such batteries by allowing the implementation of partial and ordinary differential equations that describe cell charge transfer kinetics, faradaic and non-faradaic processes. These models can be

experimentally validated by cell cycling, impedance spectroscopy and charge/discharge curves.

There are studies on thin film SSBs with a Li NE that are commonly modelled as 1D electro-chemical models. Here the SE transport mechanisms are simplified to Ohm's law due to near unity transference number of the SE. Fabre et al., [22] used constant current experimental measurements to validate their modelling results but it was only in work by Pang et al.,[23] where the rate limiting mechanisms due to different cell components under pulse operating conditions was investigated. The solid diffusion in the PE was shown to be the rate limiting step and the importance of decreasing the non-porous PE thickness was highlighted for future cell designs. This presented a new outlook that SE ionic conductivity alone was not the sole area of improvement for SSBs and that an ionic conductivity of $\approx 10^{-4}$ S cm^{-1} is sufficient for applications with more focus on the Li diffusion in the PE. However, this work did not consider mechanics in their model with a Li NE, likely due to the lower volumetric expansion during cycling which cannot be overlooked in Si based SSBs even in a thin film format.

There are limited experimental studies of Si-based SSBs that are paired with conventional PE materials which is vital to validate these models. Therefore, there is a gap in research on how to improve these systems and their electrochemical and modelling parameters which is required to design accurate models to improve cell performance.[14,24–28] Further, the sensitivity of SSB material parameters and electrode thickness on rate performance as a function of applied pressure and its echem-mech response is not well-known. Therefore, understanding the echem-mech behavior of SSBs is critical in these solid-state architectures.

Prior echem-mech studies in a SSB system are often limited to thin films,[24,29,30] however due to the simplistic nature of thin films and their planar geometry, non-porous nature, they are an excellent learning platform to better understand the[23] complex interplay of the mechanical deformation and electrochemical performance. Recent work is suggestive of high-rate capability of Si NE SSBs using a thin film format, [24,30–33] however the severity of the complex stress-field generated during particle (de)alloying at the Si|SE interface is not fully understood. A

validated echem-mech model is extremely useful to investigate the internal stress-field of thin film SSBs during realistic C-rates under applied pressure, in a non-destructive and non-invasive way. To date, comprehensive thin film SSB continuum-level models with Si NEs that have been extensively validated using robust experimental data,[33] are limited.

Studies[24,29,30] have shown that modelling the plastic deformation of Si better represents the cell behavior than a linear elastic solid. The inclusion of plasticity enables higher NE lithiation as the Si plastically deforms and relaxes the stress generated at the Si|SE interface.[34] Pioneering modelling work by Bucci et al.[35–37] have addressed the electrochemical-mechanical interplay for Si NEs SSBs and have tried to understand material properties that cause SE to fracture. A bulk-type SSB is simulated with the composite PE made of active material particles embedded within a SE and conductive carbon matrix. They concluded that softer and more compliant SEs (Young's modulus < 15 GPa, see Table 1.1) deform plastically, thereby allowing larger deformations[35] and so were more prone to microcracking (Figure 2.1). An elastoplastic behaviour is assumed for the SE, whereby the SE shell at the PE electrode interface, can undergo plastic flow. Depending on the yield stress (point at which irreversible plastic deformation occurs) and fracture strength (fracturing of the material), the SE will either undergo plastic deformation or fracture (contour lines in Figure 2.1). The contour lines exhibited in Figure 2.1, increase with increasing amounts of active material (ϕ_{AM}) in the PE in the range 0.4-0.7. Fracture can be prevented if the yield stress is not greater than half the fracture strength for any value of the SE's Poisson's ratio.[35]

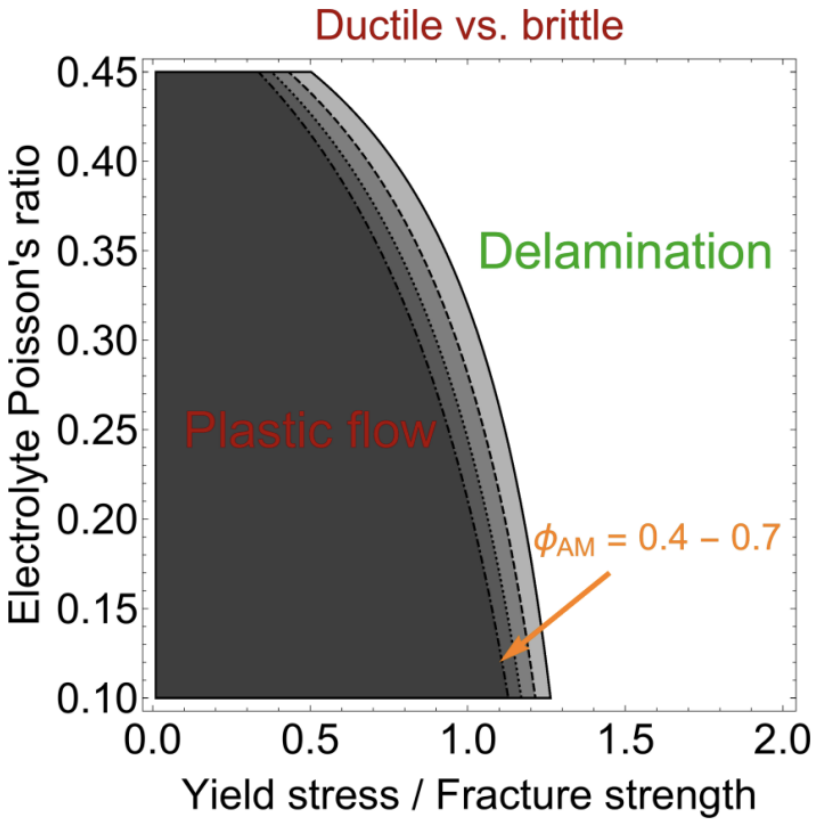

Figure 2.1 Plastic flow and delamination region for a SE given its yield stress and fracture strength. Fracture can be prevented for a SE with any value of the Poisson's ratio, provided the yield stress is not greater than half of the fracture strength. Reprinted with permission from ref.[35]

On the other hand, previous findings have argued the case for softer sulfur or solid polymer[38] SEs exhibiting higher mechanical ductility which can help to alleviate Si stress, thereby resulting in high cycle life.[14,31,39,40] These studies model a composite electrode using a continuum framework but do not consider the full cell, and the results have not been experimentally validated on full cell cycling data. This thesis (Chapter 3 and 4) will look to fill this gap by presenting a continuum scale model of a full cell SSB which is validated against experimental cycling data: 1C cycling and pulse behaviour. However, it is still not clear what mechanical properties are desired of SEs to enable optimal cell performance and lifetime. The next section will introduce different classes of SEs and discuss their

electrochemical properties and some of the challenges they face at the NE|SE interface.

2.2 Solid Electrolytes

2.2.1 Ionic Conduction in Solid Electrolytes

The understanding of ionic transport mechanisms within a LE system in a LIB is well established.[41] Li^+ ions are facilitated through the LE via lithium-containing dissolved salts. By contrast, the ion conduction mechanism of SEs occurs via their crystal lattice structure. For amorphous or NC SEs, the ion conduction mechanisms are less understood.[42] Nevertheless, it is known that the physical structure of SEs strongly influences its ionic conductivity. Focusing on the crystalline SE case, both cations and anions within a crystal lattice can move and in the case of LEs, Li^+ ions movement is favoured due to the cations' small ionic size. Both cationic and anionic conduction is seen in LEs containing lithium salts. Superionic SE conductors such as lithium-rich phosphidosilicates[43] exhibit low activation energies and high ionic conductivities (σ_{ion}) which can be related to their structure. These compounds tend to have diffusion pathways of interconnected polyhedra, preferably between face-sharing tetrahedral and octahedral voids, which leads to mobile movement of selected ions.[43]

There are three main types of ion migrations in a crystalline structure which occur at the atomic scale. The first being vacancy diffusion in which an ionic species can migrate to a vacant site in the neighbouring environment. The second, a direct interstitial mechanism which is a distortion of the lattice structure due to an excess or lack of an ionic particle. The third, a correlated interstitial migration which is a combination of the first and second; the interstitial ion displaces an ion in the neighbouring lattice which then moves this neighbouring lattice to a vacancy site. The solid-state battery impedance is then the summation of these migration mechanisms (atomic to device scale migrations).[44,45]

The conductivity of the SE is given by Equation 2.1, where *q, n, u* are the charge, concentration, and mobility respectively.

$$\sigma = q\ n\ u = \sigma_0 T^m e^{-E_a/k_B T} \qquad (2.1)$$

The equation shows an Arrhenius relationship as the conduction of the ions has an exponential dependence on *T,* temperature. The mass is represented as *m,* and k_B is the Boltzmann constant. E_a is the activation energy that is needed to be overcome to enable ionic conduction and $\sigma_0$is related to the entropy of migration, the jump distance and attempt frequency which is the probability for the ion to hop to nearest defect in unit time. This is for the simplest case of ion-hops along the lattice sites.[44,45]

In fact, the mechanism of ionic transport can be broken down into two phases; diffusion and migration of ions via defects which is the fundamental process of conduction in ions of crystalline and amorphous materials. Diffusion is often neglected in the case of a SE with a transference number ≈1. The transference number is defined as the ratio of the electric current as a result of the cations to the total current. A transference number equal to 1 implies that the ion conduction in the SE is only due to cation. The migration arises from an electric field imposed onto the solid (for example during battery cycling), which causes random motion of the individual ions but an overall movement migration of the ions along the electric field direction. The diffusion coefficient is found to be dependent on state of charge (SoC) in the SSB electrodes.[46]

In the case of amorphous polymers (transference number not equal to unity), the diffusion is realised through the motion of polymer chains. Lengths of chains can alter the conductivity properties which is dependent upon temperature (typically acceptable conductivity values at temperatures greater than room temperature >~80 ^{o}C) and this limits polymer SEs for temperature dependent applications. The theory for ionic conduction in a crystalline versus amorphous or NC structure is controversial.[42] Controlling the degree of crystallinity is a key enabler in increasing the ionic conductivity. It is commonly noted for NC lithium-containing oxide materials that they exhibit a higher σ_{ion} than their crystalline counterparts due to disorder in the NC structure (lack of long-range order) enabling facile Li^+ ion conducting pathways.[47,48]

2.2.2 Lithium Phosphorous Oxynitride (LiPON)

As seen in the previous section, understanding the pathways for conduction plays a key role in the ionic conductivity of inorganic SEs as the lithium ions are the only mobile ions that contribute to the ion transport (transference number ≈1). There have been significant developments to discover SEs with σ_{ion} equivalent to or within an order of magnitude of the LE σ_{ion}. One of the most successful SEs, LiPON was discovered in 1992 at Oak Ridge National laboratory.[49] LiPON has been commercially successful for thin film SSBs, exhibiting excellent cycling performance even at high current densities >3 mAh cm^{-2}.[23,33,50,51] The reported I-V curves of LiPON display a wide electrochemical stability window of 0-5.5 V (*vs.* Li/Li^+) compared to other lithium oxide and sulfide NC or amorphous electrolytes.[52] While LiPON exhibits many desirable qualities such as ability to resist dendrite propagation,[51] it is hindered by its relatively low ionic conductivity (lower than ≈4 orders of magnitude than LEs) and costly vacuum deposition methods. Its lower ionic conductivity can be justified in thin film format (μm thickness) which lends it to achieve these appreciable current densities. However, the magnetic sputtering synthesis techniques for these films is not only costly but time consuming, making it difficult to scale to large format cells.[53] Nevertheless, due to the lack of commercial large format SSBs, commercial thin film SSBs with a LiPON SE are an excellent tool to understand the SE interfaces as they display high cycle life and rate capability. They will be used as a learning platform to design and optimise thin film SSBs in this thesis, with the exploration of similar NC materials that are less costly than LiPON and highly scalable as promising SEs for large format advanced battery systems.

Following the discovery of LiPON there has been number of studies on thin film NC SEs.[29,54–61] Thin film SEs have generated a lot of interest compared to bulk NC materials as excess SE material lowers the overall cell energy density. By keeping the SE layer very thin, tens of μms, the cell energy density can be increased. This

is because the SE does not contribute to the overall capacity of the cell. Furthermore, despite the lower SE ionic conductivity, very thin SE and electrodes allow for shorter diffusion pathways which enables high-rate capability. This has led to the commercialisation of thin film SSBs, and it is important that the synthesis methods of these films can be scaled at a low cost, compared to the expensive sputtering and vacuum deposition methods, to scale these into large format cells. One such study by Clayton et al.[62] explored lithium oxide NC materials, using a scalable prompt inorganic condensation (PIC) method, which uses spin coating and a mild annealing process to create a dense film. The ionic conductivity (σ_{ion}) of these lithium oxide containing NC films produced using this PIC scalable method was found to be comparable to the expensive vacuum deposition methods.[62]

2.2.3 Non-Crystalline Solid Electrolytes

Non-crystalline SEs encompass amorphous, glassy solids and partially or nano-crystalline materials. As discussed in the previous section, LiPON is a NC material, however there are other NC materials such as lithium thiophosphate (xLi_2S-$(100-x)P_2S_5$, LPS). LPS has a superior σ_{ion} than LiPON (≈3 orders of magnitude greater ≈10^{-3} Scm^{-1})[63,64] but its electrochemical stability window is much lower hampering its interfacial compatibility with a lithium NE. The reason behind LiPON's unique ability to block lithium dendrite propagation is not fully understood, but a theory by Han et al.[7] pertaining to its lower electronic conductivity (σ_e ≈10^{-12} S cm^{-1}) compared to its ionic conductivity is likely one reason.

The ionic conductivity of NCs are also largely influenced by their local structure. LiPON for example, displays an increase in σ_{ion} with increasing Li and N content which increases the disorder of the PO_4 units. By increasing the N in bridging sites (bridge between PO_4 units) the Li^+ ion mobility in LiPON was maximized.[65,66] Both LPS and LiPON have been shown to increase their σ_{ion} through their network disorder. Annealing temperature and duration[54], precursor ratios, thickness of the SE film[55] and processing atmosphere all play a role in altering the ionic conductivity of NC SEs.[42,65,67] It has recently been observed in the research

community that the amorphisation of lithium lanthanum zirconium oxide (LLZO), which is commonly synthesised as a crystalline material, can hinder dendrite formation.[56,58,68] Kim et al.[58] showed that by laser annealing a bulk LLZO pellet, the amorphised surface blocked electron injection and significantly increased the critical current density (the current density above which lithium dendrites are thought to form). Sastre et al.[58] demonstrated homogenous, grain-boundary free, amorphous LLZO with stable plating and stripping in a Li symmetric cell at appreciable current densities (> 3.2 $mAcm^{-2}$). It should be noted that the bulk LLZO material exhibits a higher conductivity in its fully crystalline version compared to its thin film amorphised counterpart (≈2 orders of magnitude lower) but this can be justified by its thickness in a thin film being ≈2 orders of magnitude lower.

Figure 2.2 illustrates the ionic conductivities as a function of temperature for three main classes of SE materials characterised in their local structure: crystalline, ionic liquid, amorphous and glassy ceramic (NC). NCs materials do not exhibit comparable σ_{ion} to LEs at RT, and bulk crystalline SEs and ionic liquids may be more comparable.

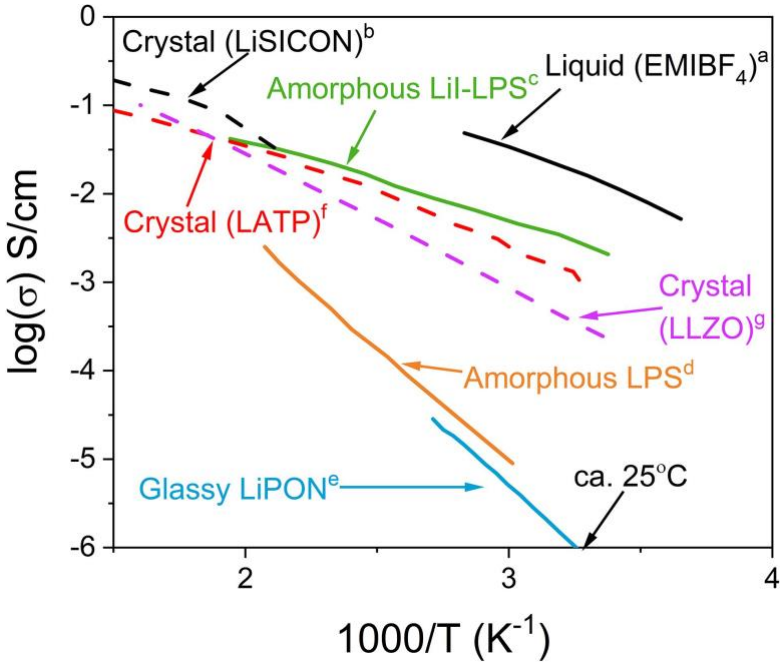

Figure 2.2 Ionic conductivity as a function of temperature for a range of SEs. Reprinted with permission from ref.[42]

Lithium-conducting bulk SE sulfide glasses have been reported with conductivities greater than 10^{-4} S cm^{-1} at RT. Hayashi et al.[69] looked at the advantages of adding oxysulfide glasses to lithium thiosilicate glasses to increase the ionic conductivity to $\approx 10^{-3}$ S cm^{-1}, and in particular the Li_3BO_3 addition was the most electrochemically stable over 100 cycles. Glass electrolyte properties can be optimised by altering the chemical compositions and creating homogenous pathways for ionic transport. Mizuno et al.[70] reported $70Li_2S$-$30P_2S_5$, thio-LiSICON structure with a conductivity equal to 3.2×10^{-3} S cm^{-1} due to the formation of crystalline phases thereby increasing the conductivity. These nanocrystalline compounds which exhibit a degree of crystallinity seem to have higher conductivity than their completely fully amorphous versions.[19] This thesis predominantly focusses on amorphous or NC SEs in a thin film format, however the mechanical properties of commonly used bulk inorganic SEs are addressed in Chapter 4 where they are simulated in a Si based SSB. Therefore, the following section briefly discusses commonly used crystalline bulk SE materials which are typically used in large format SSBs.

2.2.4 Crystalline Solid Electrolytes

As seen for NC, glassy or glass-ceramic materials, a degree of crystallinity is optimal for high ionic conductivity. However, this is not the case for all classes of materials, for example ceramic inorganic materials in a bulk format which exhibit highest ionic conductivity when fully crystallised. In the pursuit of SEs with higher ionic conductivity, bulk crystalline inorganic SE materials have been the area of recent focus. Organic SEs have also been studied; though they are plagued by their low σ_{ion} and low electrochemical window which limits their stability against lithium NE.[71,72] Inorganic SEs consisting of sulfide and halide SEs have higher room temperature (RT) σ_{ion}, $\approx 10^{-2}$ - 10^{-3} S cm^{-1},[5,43,73]which contrasts well with LEs ($\approx 10^{-2}$ Scm^{-1}) and they are mechanically softer, ductile materials with a lower Young's modulus (E). Sulfides have a higher polarizability of sulfur, compared to oxygen which increases the mobility of the lithium ions across the SE. However,

although their lower Young's modulus compared to oxide SEs can increase their interfacial contact with the electrode surface, they face problems such as dendrite formation at the NE and interfacial instability at both electrodes due to their limited electrochemical potential window. These issues could be solved by modifying the SE interface (e.g., adding coatings or buffer layers [74] between SE and electrodes) to expand the electrochemical window of the SE to match that of the cell operating voltage range and prevent decomposition of the SE. In addition, cycling the cell with applied pressure could ensure better contact between the SE and PE (Figure 2.3).

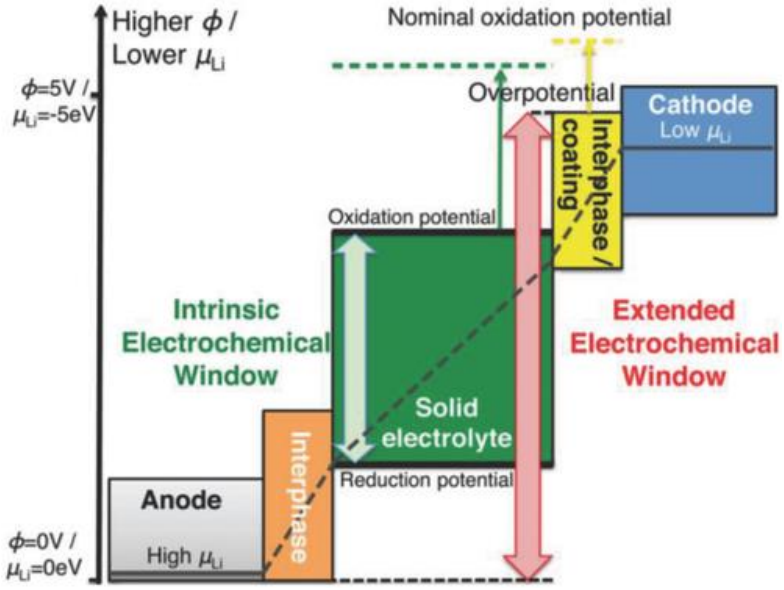

Figure 2.3 Solid electrolyte electrochemical window, with the inclusion of coating layers to extend the electrochemical window of the SSB. Reprinted with permission from ref.[74]

Resistances in the electrolyte layer can limit the performance of the SSBs with sulfide and halide SEs exhibiting a much lower grain boundary resistance at lower sintering temperatures (synthesised by cold-pressing methods) compared to oxide-based SEs. The main multiphysics properties of inorganic SEs are displayed as a traffic light colour scheme in Figure 2.4, whereby green signifies a highly desirable and red an undesired SE property to enable high performance SSBs.[75] It should be

noted that Li dendrite inhibtion has a higher weighting factor than the other SE material properties as only a handful of SEs are stable against Li. Oxide SEs can be synthesised using a more scalable method via sol-gel or other wet chemical methods.

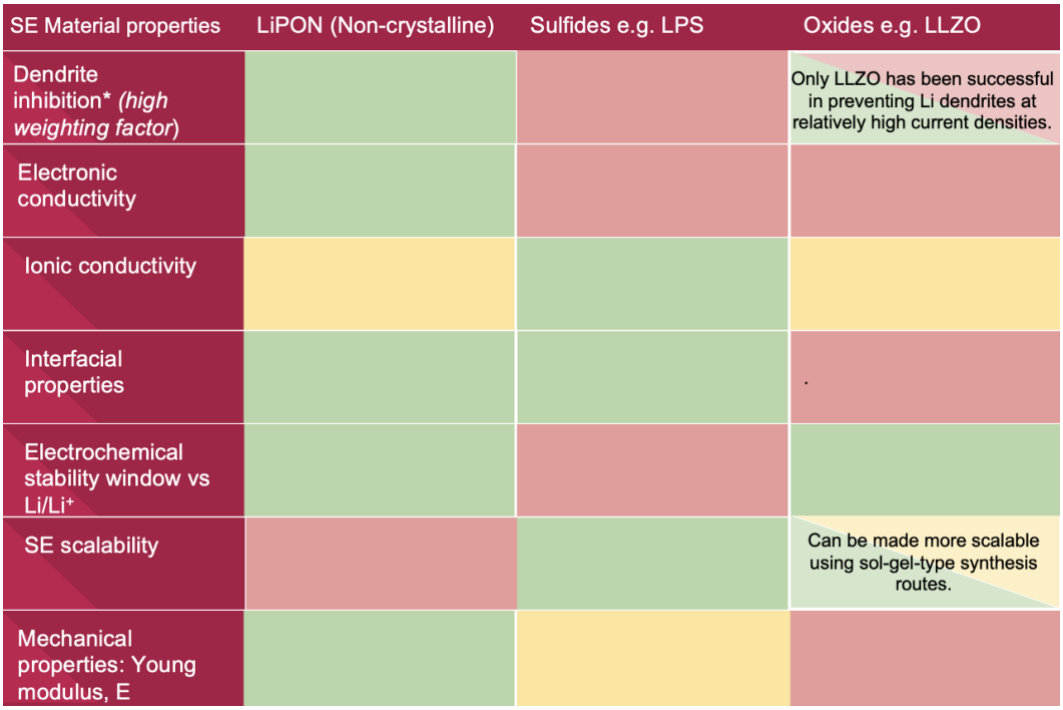

Figure 2.4 Summary of inorganic SEs properties with a traffic light colour scheme to highlight the desired material properties (in green) in each category.

Oxide SEs namely LLZO is a promising SE due to its large electrochemical stability window. Oxide SEs are relatively stable in air do not require strict air-sensitive processing methods as is the case for sulfide and halide SEs. The high Young's modulus of oxide materials and brittle nature can be detrimental to its cycling performance and cause fracturing in which lithium metal can deposit. Oxides can be characterised by three commonly reported classes: NASICON, perovskite and garnet type SEs. LLZO falls into the garnet class, and its high σ_{ion} ($\approx 10^{-4}$ S cm^{-1})[76] at RT, especially the cubic phase, is not common for this class of materials. A lower σ_{ion} of $\approx 10^{-5}$- 10^{-6} S cm^{-1} (at RT) is more commonly reported with costly high temperature sintering (>1000 ^{o}C). Though, even after high

temperature sintering, oxide-based SEs show high grain boundary resistance; one of their greatest disadvantages. An inherent problem of garnet materials is their rigidity and poor lithium wettability which causes issues at both electrode interfaces.

2.3 Solid Electrolyte and Electrode Interface

2.3.1 Lithium Metal Interface

As examined in the previous sections, the requisite properties of a SE should include: (1) a suitably high σ_{ion} to enable high current densities, (2) a wide electrochemical window to increase interfacial stability against high voltage electrodes and (3) form a low impedance interface at both electrodes. So far, as the focus has been mainly on (1) and (2), this section will investigate (3): the SE|electrode interface. It is important that a low impedance SE layer is formed at the NE|SE interface, which is homogenous and exhibits low grain boundaries to enable the stable plating and stripping of lithium. It is often observed that in the presence of an externally applied pressure (stack pressure), cycle life can be improved as a result of improved contact between the SE|electrode interface.[77–79] Nevertheless, if too much stack pressure is applied which results in high amounts of compressive stress, it could be detrimental to SSB performance due to possible fracturing.

A critical current density has been identified by Kasemchainan et al.[80] whereby if lithium is removed (stripped) from the interface faster than it can be replaced (plated) then voids can occur leading to dendrite formation. Moreover, a pressure dependence on the stripping shows that lithium creep becomes the principal mechanism, rather than diffusion (Figure 2.5). This means that dendrite formation can occur at current densities lower than the critical current density due to the Li not being replaced at the surface fast enough during stripping which leads to void formation and Li plating within these voids during the subsequent plating step. Increasing the stack pressure can increase the critical current density at which dendrites can form by increasing the contact between the interfaces thereby

delaying the onset of void formation. Other factors that influence the critical current density include the SE surface chemistry and microstructure as well as mechanical properties such as the compressive yield strength and Young's modulus of the Li metal and SE.

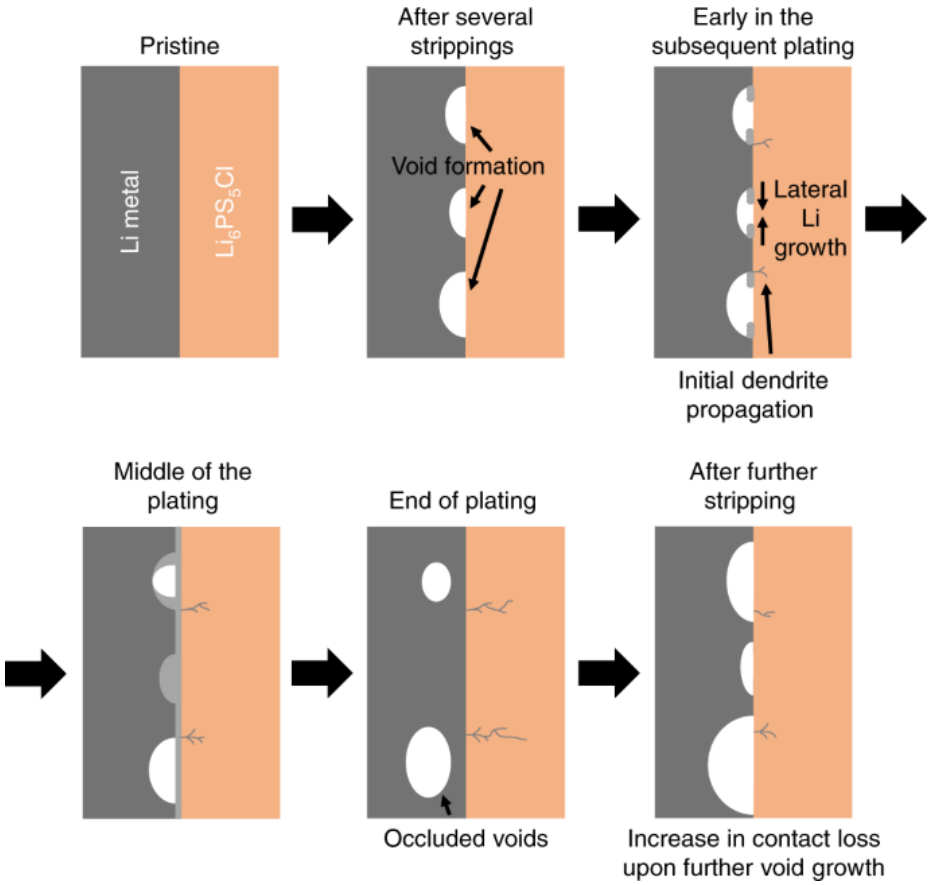

Figure 2.5 Illustrates plating and stripping cycles of lithium metal with voids occurring on stripping resulting in lateral Li filaments growing on the subsequent plating cycle. A few voids are eliminated during the plating cycle however some occluded voids remain which leads to further void growth and contact loss. Reprinted with permission from ref.[80]

The surface chemistry and homogeneity of the SE is crucial for stable SSB performance as investigated by Westover et al.[51] when studying LiPON's ability to suppress Li penetration. The mechanical properties of LiPON also play an important role in reducing the probability of lithium penetration due to its ductility compared to brittle NASICON SEs.[81] Studying the problematic electrode|SE

interface in terms of its interfacial resistance as a function of SoC, temperature and applied pressure can be extremely insightful. EIS can be deployed to characterise this interfacial impedance.

2.3.2 Electrochemical Impedance Spectroscopy

This chapter is adapted from the work published in "Vadhva, P.; Hu, J.; Johnson, M. J.; Stocker, R.; Braglia, M.; Brett, D. J. L.; Rettie, A. J. E. Electrochemical Impedance Spectroscopy for All-Solid-State Batteries: Theory, Methods and Future Outlook. *ChemElectroChem* **2021**, *8* (11), 1930–1947. https://doi.org/10.1002/CELC.202100108."

Electrochemical tools can be deployed to characterise the SE and electrode interface, particularly between the lithium NE and SE which has problematic dendrite issues as discussed in the previous section. One such tool: EIS can be used to investigate new SE materials and probe the stability at the SE|electrode interface. It is a particularly useful tool as the bulk and interfacial transport processes that determine battery performance take place over many length- and time- scales. EIS is a non-destructive technique that can span $\sim 10^9$ orders of magnitude in the frequency domain (mHz to MHz). In a typical EIS experiment, a small sinusoidal perturbation voltage is applied to an electrochemical system. The resulting linear current density shares the frequency of the input, but its phase, φ, and amplitude may differ. The ratio of voltage amplitude, U of the wave to the current amplitude, i, is a complex number that depends on frequency, also known as the impedance, $Z(\omega)$:

$$Z(\omega) = \frac{U}{i} = Z^0(cos\varphi + \sin\varphi) \tag{2.2}$$

where Z^0 is the magnitude of the complex impedance $Z(\omega)$. When plotting impedance graphs in a complex plane with polar co-ordinates, this results in an imaginary and real impedance axes, also known as the Nyquist plot. Linear EIS

uses small amplitude perturbations to stay within the linear response regime and therefore can only probe the linear processes in a battery.

The amplitude of the impedance on the Nyquist plot is calculated by the modulus of the impedance:

$$|Z(\omega)| = \sqrt{Z_{real}^2 + Z_{imaginary}^2} \tag{2.3}$$

EIS measurements are conducted by sweeping over a wide frequency range, taking measurements for each perturbation. The frequency range of the impedance analyser is important as a wide range is needed to capture both the fast and slow kinetics and transport mechanisms respectively.[82–85] Information about the timescales of these parameters can be estimated from the EIS plot as they are inversely linked to the frequency. Sample and interfacial contributions to the impedance can be separated and tracked with respect to temperature, applied pressure, SoC and ageing.

Equivalent circuit modelling (ECM) is commonly used to fit the EIS data using an electrical circuit. ECM requires a quantitative understanding of the chemical processes which draws upon previous experience to fit elementary components (resistors, capacitors etc.) into a general circuit which will fit the data. Generalized impedance parameters have been developed from physics principles to better fit the data under real conditions; porosity and tortuosity of electrodes modelled by a constant phase element (Q) instead of a capacitor have been realised.[86]

A resistor is often used to describe the charge transfer resistance or model the electrolyte ion conductance and a capacitor is used to model the double layer capacitance which occurs at the electrode|electrolyte interface due to charge accumulation and depletion. A Warburg element, (W) is commonly used to express the resistances due to mass transfer, i.e., diffusion which occurs in the limiting electrode (usually the PE).[87] Warburg elements drop out at high frequencies as the diffusion time scale is too short to influence the current and other effects such as the inductance can dominate. At high frequencies inductance is due to the electrical

resistance of wires and at low frequencies it is due to any degradation processes occurring within the cell.[88,89] Combining these generalised impedance parameters with the elementary components enables the value of ionic conductivity and interfacial impedances of vital systems to be evaluated.

With some exceptions, the generic ECM for a full cell SSB with a Li NE consists of (from high to low frequency): $(RQ)_b(RQ)_{gb}(RQ)_{NE}(RQ)_{PE}$ and a CPE or Warburg element for diffusion processes into the electrodes[90–92] where $(RQ)_b$ represents the bulk SE and $(RQ)_{gb}$ the SE grain boundary resistance and capacitive terms. The SoC-dependent impedance is important to fully understand battery behaviour occurring at the solid-solid interfaces during operation. Figure 2.6 shows the evolution of a In|LGPS|LCO cell during charge and discharge,[93] with three distinct processes identified in high, mid and low frequency ranges (Figure 2.6a). Upon charging, the In NE interface resistance (low frequency) was largely unchanged, but the PE interface resistance (mid frequency) increased. This is the opposite assignment of the NE and PE interfacial impedances observed in full cells with an Li NE (with respect to frequency). This trend on charging was attributed to loss of interfacial contact in the composite PE due to volumetric expansion and the formation of a decomposition layer on exposed LCO (Figure 2.6b). At higher SoCs, a more noticeable Warburg impedance began to appear which was assigned to the diffusion of Li^+ ions in the PE material. However, during discharge the NE interface resistance increases becoming greatest at the end of discharge (Figure 2.6c). This increase in interfacial resistance at the In|SE interface was ascribed to the degree of lithiation of the In−Li alloy NE, which becomes more In-rich during discharge.

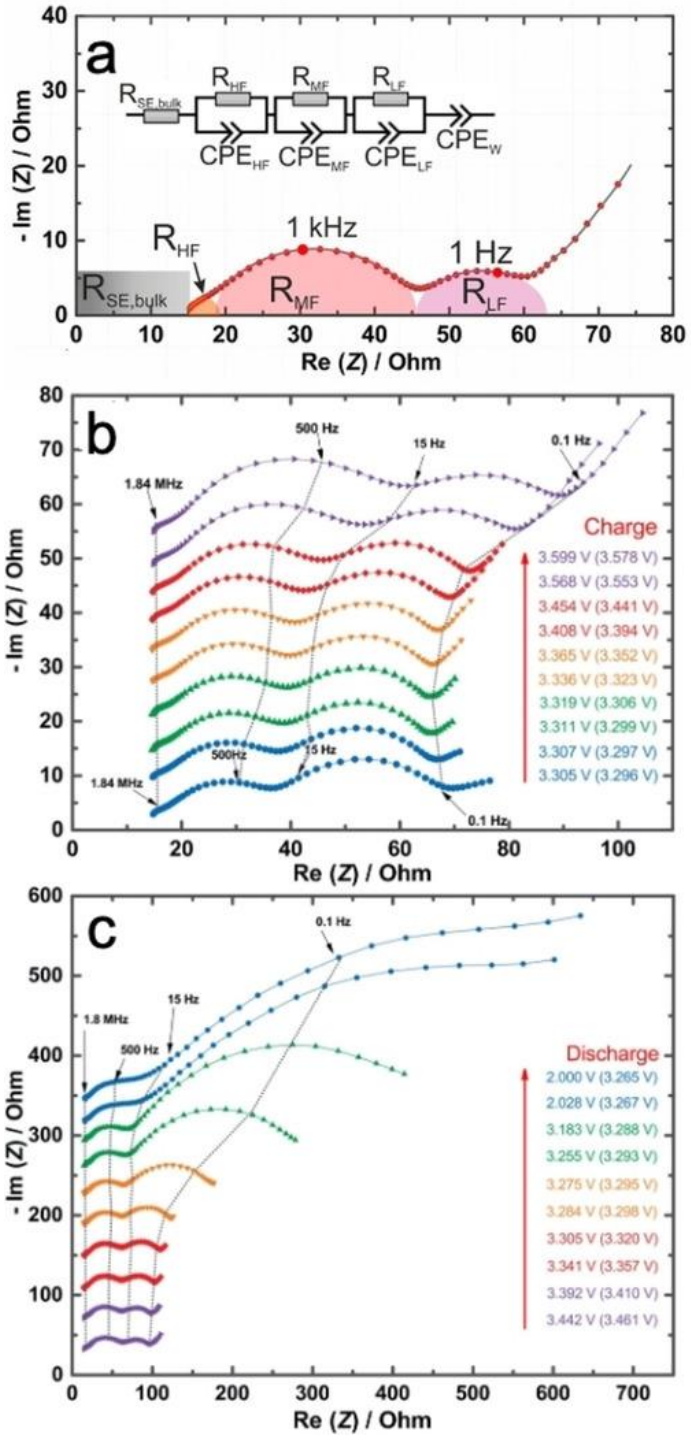

Figure 2.6 Stacked Nyquist plots of In|LGPS|LCO cell with $LiNb_{0.5}Ta_{0.5}O_3$ (LNTO)-coated LCO as the active material. **a)** ECM and EIS during **b)** charge and **c)** discharge at different SoC points. The low-frequency semicircle is assigned to the NE interface. Reprinted with permission from ref.[93]

Oxide SEs commonly exhibit large impedances at the Li|LLZO interface which can be ameliorated using interfacial layers and the removal of Li_2CO_3, which forms on the surface of LLZO in ambient conditions.[94] Recently, Krauskopf and co-workers[95] used a Li|LLZO|Li symmetric cell to analyse the influence of applied pressure on the Li|LLZO interface. They showed that, with careful surface preparation and handling under inert gas to avoid Li_2CO_3 formation, sufficient applied pressure reduced the interfacial impedance to a negligible value (<1 Ω cm^2), which remained after the pressure was removed. Interfacial modification can also be helpful at the PE|LLZO interface as well; for example, a Nb-containing interlayer resulted in significantly reduced interfacial resistance in an LCO|LLZO|Li battery.

2.4 Applied Pressure

As emphasis is drawn to full-cell SSB design, the role of cell stacking, and externally applied stack pressure becomes increasingly important to consider. The role of externally applied stack pressure has received increased attention and yet interestingly there is no clear consensus on what the optimal stack pressure should be for SSBs.[96] In contrast to LIBs, SSBs require a certain amount of pressure for high cycle life to enable sufficient contact between the notorious SE|electrode interface. Previous studies have used stack pressures ranging from as little as ≈3 MPa to 250 MPa[12,77,78,96] for Li-alloy based NEs. At the lower end of the stack pressure spectrum, Li NEs are commonly reported due to the lower Young's modulus of metallic Li, versus higher stack pressures for Li-alloy NEs which have a higher Young's modulus, albeit exhibit much larger volumetric expansion upon lithiation. Furthermore, as we look towards commercilising SSBs, due to their mechanical rigidity a pouch cell form factor is likely to be adopted. Stack pressure will play an increasingly important role as synthesis of SSBs moves away from pellet size set ups (designed inhouse with lack of standardisation between research groups), to large format pouch cells. The areal homogeneity will be of significance

in the 2D pouch cell geometry and creating a homogenous pressure distribution throughout the SSB will be more challenging. Sandwiching cell layers inside a stack to provide a uniform pressure will require sophisticated engineering.

Currently, standardisation of such a stack design has not been achieved.[96] There is considerable variation in the SSB pressure depending on whether a spring and gasket are used together to clamp each of the pouch cell corners (Figure 2.7a-b).[96] From Figure 2.7b it can be concluded that a uniform pressure distribution occurs using both springs and gaskets. Furthermore, for this particular stack design, when considering the stack pressure in terms of overall cell gravimetric energy density, a minimal SSB system of 20 kWh with stack pressures of < ≈1.5 MPa is required to produce comparable cell-to-module efficiencies to LIBs (Figure 2.7c-f).

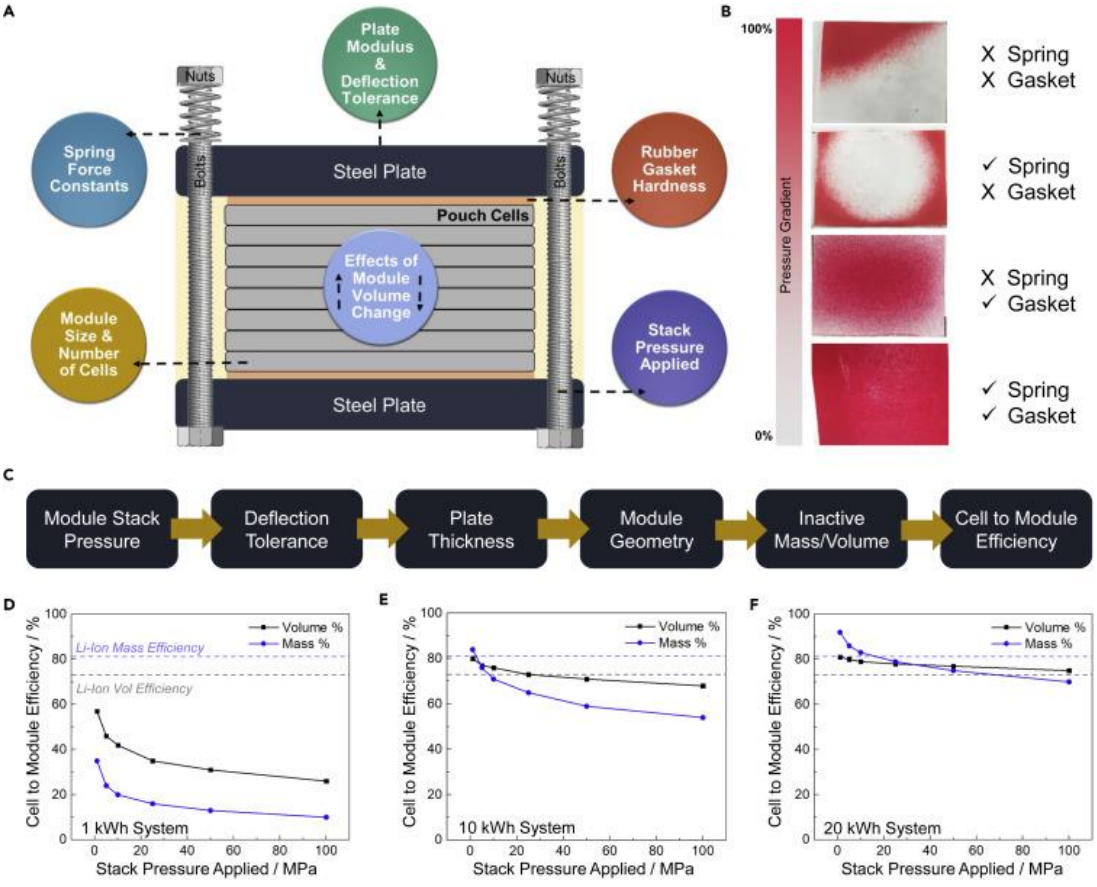

Figure 2.7 a. Schematic of the SSB module under stack pressure with **b.** the pressure gradient as a function of using springs and gaskets. **c-f.** Model of the cell-to-module conversion efficiencies for different stack pressures for a **d.** 1 kWh system, **e.** a 10 kWh

system and **f.** a 20 kWh system. The LIB mass efficiency (dashed blue line) and volume efficiency (dashed grey line) are displayed for comparison. Reprinted with permission from ref.[96]

Additionally, the SSB stress response during cycling is an important consideration towards overall cell performance. The internal stress within the SSB increases the cell overpotentials due to lithiation-induced stress. The partial molar volume of lithium in Li and Si NEs is very large compared to PE materials. Han et al.[97] found that for a composite Si NE, reducing the particle size lowered the observed stress. Work by Doux et al.[78] highlighted that the fabrication pressure of SEs is more critical for cycle life than stack pressure. Both fabrication pressure and stack pressure affect the ionic conductivity of the SE and impedance of the SE|electrode interface and therefore should be carefully controlled when engineering SSBs. The internal stress is important to measure and quantify using experimental methods to validate echem-mech models. Validated physical models can provide crucial insights into the deformation of electrode and SE structures as well as any phase transformation processes in the NE or PE.

Chapter 3

Thin Film Silicon Solid State Batteries via Modelling and Experimental Characterisation

This chapter is adapted from the work published in "Vadhva, P.; Boyce, A.; Hales, A.; Pang, M.-C.; Patel, A.; Shearing, P. R.; Offer, G. J.; Rettie, A. Towards Optimised Cell Design of Thin Film Silicon-Based Solid-State Batteries via Modelling and Experimental Characterisation. *J Electrochem Soc* **2022**. https://doi.org/10.1149/1945-7111/AC9552."

Contribution Statement: The model equations and implementation into COMSOL Software was carried out equally by A. Boyce and P. Vadhva. Pulse testing and equivalent circuit modelling was conducted by P. Vadhva using code written by R. Tomlin and RC parameters extracted by A. Hales. All other experimental testing and analysis was carried out by P. Vadhva with assistance from A. Patel and initial project guidance from M. Pang. Funding acquisition and project supervision by P. Shearing, G. Offer and A. Rettie.

3.1 Introduction

As many fundamental aspects of Si-based SSBs are poorly understood, such as the solid-solid coupling between Si and the SE during the large volumetric expansion during Si lithiation,[28,98–100] a validated electrochemical model can be highly useful. Through the coupling of the electrochemical and mechanical transport mechanisms, the model can provide an insight on the stress-strain response within the cell and sensitivity on electrochemical parameters. By improving our understanding of the stress-strain relationship at the *a*-Si|SE interface, the mechanical properties of the SE, cell dimensions and electrode thicknesses may be tailored to limit Si expansion. This can help to increase cell lifetime, and enable high power micro-batteries with potential implications for large-format SSBs.

There are limited studies of Si-based SSBs that are paired with conventional PE materials.[14,24–28] Furthermore, while models of Si-based LIBs are well described in the literature,[34,101–104] those of SSBs with Si NEs are lacking, especially those validated against experimental data for cycling and pulsing conditions. To address these issues, in this work, a 2D echem-mech model was built and validated using a suite of experimental electrochemical tests under dynamic load conditions, on a thin-film amorphous silicon (*a*-Si)|LiPON|$LiCoO_2$ SSB.

First, Section 3.2 describes the model formulation whilst Section 3.3 discusses the material parameters and simulation details. The experimental methods are described in Section 3.4. Section 3.5 presents the electrochemical behavior during initial cell formation, steady state conditions and pulsed conditions using GITT and hybrid pulse power characterisation (HPPC). In several cases, these results were used to parameterise the model. Subsequently, model agreement with charge/discharge curves acquired at 1C rate was investigated followed by further validation against the HPPC response. Finally, this work presents the effects of varying relative electrode thickness (up to a factor of 4) on the mechanical stresses and strains experienced in the SSB model.

3.2 Model Formulation

A schematic of the SSB is illustrated in Figure 3.1: the CCs, SE separator, *a*-Si negative and LCO positive electrodes, where t_{cc}, t_{sep}, t_{ne}, t_{pe} are their respective thicknesses, is defined. Also, note the orthogonal coordinate system, where the *x*, *y*, and *z* coordinates are the thickness, length and width of the thin film SSB respectively. The ensuing echem-mech framework assumed a 2D geometry in cell thickness and length (*x* and *y*, given the film-like nature of the SSB) with Li transport and mechanical properties occurring in 1D along *x*-*y,* with a plane strain mechanical treatment (Figure 3.1). For computational efficiency, a small sub volume of the overall cell thickness *x*, was modelled, which was assumed to be representative of the cell.

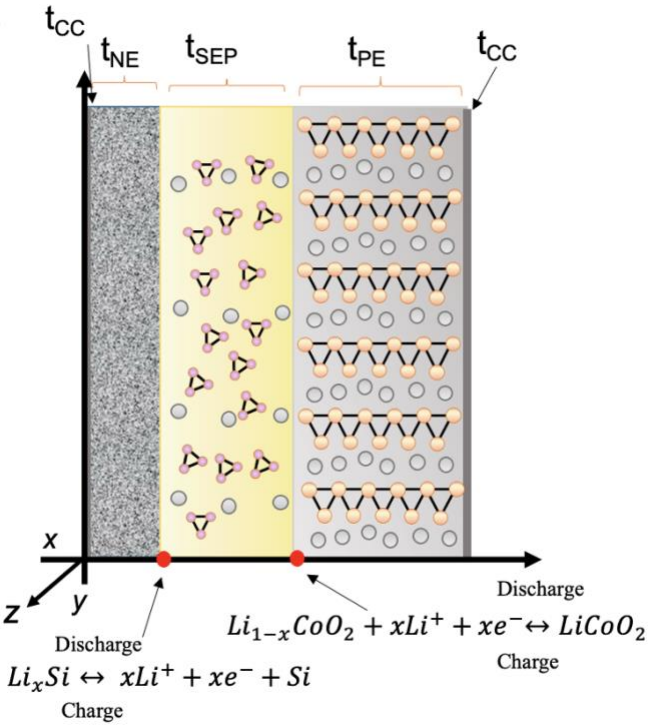

Figure 3.1 The 2D cross-sectional schematic of the thin film SSB used in the COMSOL model. Note that the atomic arrangements are purely for illustrative purposes and that atomistic simulations were not performed in this study.

3.2.1 Solid electrolyte

The SE is described by concentrated solution theory[105] and with Li^+ ions assumed to be the only mobile species present. This is a reasonable assumption as the transference number has been experimentally measured to be close to unity for LiPON.[9,14] The Nernst-Plank equation is used to model ion conduction in the bulk SE region,

$$\boldsymbol{J_b} = -D_b \nabla c_{b0} + \frac{z_i F}{RT} D_b c_{b0} \nabla \varphi_b \tag{3.1}$$

where $\boldsymbol{J_b}$ is the flux across the bulk electrolyte, z_i is the species charge, F is Faraday's constant (96,485 C mol^{-1}), D_b is the diffusion coefficient, c_{b0} is the initial concentration of the bulk SE and φ_b is the electric potential across the medium. Given that the electrolyte is a solid body, convection terms were neglected. Current through the SE was modelled using Ohm's law (3.2a), in addition, the system must obey charge conservation (3.2b):

$$\boldsymbol{i}_b = -K_b \nabla \varphi_b \tag{3.2a}$$

$$\nabla \cdot \boldsymbol{i_b} = 0 \tag{3.2b}$$

where $\boldsymbol{i_b}$ is the current in the bulk SE (bold symbols represent vector quantities) and K_b is the ionic conductivity of the SE.

The stress in the SE obeys mechanical equilibrium such that body forces are neglected,

$$\nabla \cdot \boldsymbol{\sigma_b} = 0 \tag{3.3}$$

where $\boldsymbol{\sigma_b}$ is the Cauchy stress tensor. The SE is assumed to obey Hooke's Law: $\boldsymbol{\sigma_b} = C_b \times \varepsilon_b$, where C_b is the stiffness matrix, and in this instance, the model is considered to be isotropic with Young's modulus, E_b and Poisson's ratio, ν_b. A

small strain formulation is considered, where the total strain $\boldsymbol{\varepsilon}_{\mathrm{b}}$ is obtained by solving for the displacement field, $\boldsymbol{u}$ in the SE,

$$\boldsymbol{\varepsilon}_{\mathbf{b}} = \frac{1}{2}((\nabla \boldsymbol{u})^T + \nabla \boldsymbol{u}) \tag{3.4}$$

3.2.2 Positive electrode

Like the SE, the LCO positive electrode is assumed to observe mechanical equilibrium (Equation 3.3), while a similar small strain formulation and isotropic Hooke's law are employed, with stress $\boldsymbol{\sigma}_{\mathrm{p}}$, a total strain $\boldsymbol{\varepsilon}_{\mathrm{p}}$, stiffness matrix $\boldsymbol{C}_{\mathrm{p}}$, Young's modulus E_{p} and Poisson's ratio, ν_{p}. Here, there is diffusion induced strain $\boldsymbol{\varepsilon}_p^{ch}$, and consequently the total strain $\boldsymbol{\varepsilon}_{\mathrm{p,}}$ must be decomposed into an elastic component $\boldsymbol{\varepsilon}_{\mathrm{p}}^{\mathrm{e}}$, and a diffusion-related component: $\boldsymbol{\varepsilon}_{\mathrm{p}} = \boldsymbol{\varepsilon}_{\mathrm{p}}^{\mathrm{e}} + \boldsymbol{\varepsilon}_{\mathrm{p}}^{\mathrm{ch}}$, where $\boldsymbol{\varepsilon}_{\mathrm{p}}^{\mathrm{ch}}$ is given as,

$$\varepsilon_{\mathrm{p}}^{\mathrm{ch}} = \frac{1}{3}\Omega_{\mathrm{p}}(c_{\mathrm{p}} - c_{\mathrm{p0}})\mathbf{I} \tag{3.5}$$

where c_{p} is the Li concentration, c_{p0} is the initial Li concentration, Ω_{p} is the partial molar volume and $\mathbf{I}$ is the identity tensor. Solid-state diffusion in the PE is modelled using Fick's first law with an additional contribution due to diffusion-induced swelling (hydrostatic) stresses ($\boldsymbol{\sigma}_{\mathrm{p,H}}$),

$$\boldsymbol{J}_{\mathbf{p}} = -D_{\mathrm{p}}\nabla c_{\mathrm{p}} + \frac{\Omega_{\mathrm{p}} c_{\mathrm{p}}}{RT}\nabla \boldsymbol{\sigma}_{\mathrm{p,H}} \tag{3.6}$$

where $\boldsymbol{\sigma}_{\mathrm{p,H}} = \mathrm{tr}[\boldsymbol{\sigma}]/3$, D_{p} is the diffusion coefficient, and $\boldsymbol{J}_{\mathbf{p}}$ is the flux, where the subscript p detonates these parameters to relate to the PE region. Fick's second law describes the transient transport of Li in the electrode,

$$\frac{\partial c_{\mathrm{p}}}{\partial t} = \nabla \cdot \boldsymbol{J}_{\mathbf{p}} \tag{3.7}$$

Current flow was modelled using Ohm's law,

$$\boldsymbol{i}_{\mathrm{p}} = -K_{\mathrm{p}} \nabla \varphi_{\mathrm{p}} \qquad (3.8)$$

where $\boldsymbol{i}_{\mathrm{p}}$ and K_{p} are the current and electronic conductivity across the PE respectively. Finally, charge conservation was observed:

$$\nabla \cdot \boldsymbol{i}_{\mathrm{p}} = 0 \qquad (3.9)$$

3.2.3 Negative electrode

It is known that thin film electrodes at a given capacity do not display a difference in stress (across the thickness of the electrode) unless the electrode materials experience plastic deformation.[106] If only elastic deformation of the electrodes occurs, then hysteresis would be not observed as the loading and unloading during cycling would occur along the same stress path. It is important to highlight that other stress contributions could affect the hysteresis loop, such as the Li concentration gradients at the electrode interfaces. However, as LCO is not expected to plastically deform due to its higher Young's modulus and hardness than *a*-Si (even when fully lithiated)[107] it is reasonable to assume that voltage hysteresis (as observed experimentally in Section 3.5.2) is primarily due to plastic deformation of *a*-Si occurring during discharge.

Upon lithiation Si can exhibit nominal strains up to 300%, thus it is appropriate to adopt a viscoplastic-type yield model.[102,106] The following approach was adapted from Di Leo et al. [34] who experimentally validated their electro-mechanical model against half-cell curvature data using mechanical measurements of an *a*-Si electrode and a LE.,[16,17] To the best of our knowledge, analogous experiments have not been reported for *a*-Si with a SE. The method is summarised as follows: finite deformation kinematics is considered with large elastic-plastic strains and multiplicative decomposition of the deformation gradient, $\boldsymbol{F}=\boldsymbol{F}^{\mathrm{e}}\boldsymbol{F}^{\mathrm{p}}\boldsymbol{F}^{\mathrm{ch}}$, where the superscripts represent the elastic, volume-preserving plastic, and lithiation-induced deformation gradients. The lithiation-induced deformation gradient is given as $\boldsymbol{F}^{\mathbf{ch}} = \left(1 + \Omega(c_n - c_{n0})\right)^{1/3}$. The plastic deformation evolves as,

$$\dot{\boldsymbol{F}}^{\mathrm{p}} = \dot{\varepsilon}^{\mathrm{p}}_{\mathrm{eq}} \left(\frac{3\boldsymbol{\sigma}}{2\sigma_{\mathrm{eq}}} \right) \boldsymbol{F}^{\mathrm{p}} \tag{3.10}$$

where $\dot{\varepsilon}^{\mathrm{p}}_{\mathrm{eq}} > 0$ is the equivalent plastic strain rate and $\sigma_{\mathrm{eq}} = \sqrt{3/2}|\boldsymbol{\sigma}|$ is the equivalent stress. During plastic flow, the equivalent strain rate is taken to be,

$$\dot{\boldsymbol{\varepsilon}}^{\dot{p}}_{\mathrm{eq}} = \begin{cases} 0 & if\ \sigma_{\mathrm{eq}} \leq \sigma_{\mathrm{Y}}(\bar{c}) \\ \dot{\varepsilon_0} \left(\dfrac{\sigma_{\mathrm{eq}} - \sigma_{\mathrm{Y}}(\bar{c})}{\sigma_*} \right)^{nr} & if\ \sigma_{eq} > \sigma_Y(\bar{c}) \end{cases} \tag{3.11}$$

where σ_* is a stress-based constant, $\dot{\varepsilon_0}$ is a reference plastic strain-rate and *nr* is a strain-rate related fitting parameter. The concentration-dependent yield stress, $\boldsymbol{\sigma}_{\mathrm{Y}}(\bar{c})$ is given as,

$$\sigma_{\mathrm{Y}}(\bar{c}_{\mathrm{n}}) = \sigma_{\mathrm{sat}} + (\sigma_0 - \sigma_{\mathrm{sat}}) e^{-\frac{\bar{c}_n}{\bar{c}_*}} . \tag{3.12}$$

where σ_0, σ_{sat}, c_* are positive-valued stress-related fitting parameters.[34] As with the PE, diffusion of Li within the NE is captured using Fick's Law and an additional swelling term, analogous to Equation 3.6,

$$\boldsymbol{J}_{\mathbf{n}} = -D_n \nabla c_n + \frac{\Omega_{\mathrm{n}} c_{\mathrm{n}}}{RT} \nabla \sigma_{\mathrm{n,H}} . \tag{3.13}$$

As in the studies of Sethuraman et al.[106] and Di Leo et al.[34] quadratic, higher-order stress-related terms are neglected by assuming their negligible influence on the overall response. As before, Fick's second law provides a description of transient diffusion,

$$\frac{\partial c_{\mathrm{n}}}{\partial t} = \nabla \cdot \boldsymbol{J}_{\mathbf{n}} . \tag{3.14}$$

As before, Ohm's law describes current flow,

$$\boldsymbol{i}_{\mathrm{n}} = -K_{\mathrm{n}} \nabla \varphi_{\mathrm{n}} \tag{3.15}$$

with $\boldsymbol{i}_{\mathrm{n}}$ and K_{n} being the current and electronic conductivity, across the negative respectively, and charge conservation is observed,

$$\nabla \cdot \boldsymbol{i}_{\mathrm{n}} = 0 \tag{3.16}$$

3.2.4 Charge transfer kinetics

It is necessary to impose boundary conditions at the interfaces of the SE and electrode in order to accurately solve model equations. By doing so the charge transfer reactions and the additional stress overpotential required for lithiation to proceed are captured. The charge transfer rate is commonly expressed using a Butler-Volmer type equation,

$$i_{\mathrm{BV}} = i_0 \left(\exp\left(\frac{\alpha_n F \eta_{\mathrm{n}}}{RT} \right) - \exp\left(-\frac{\alpha_p F \eta_{\mathrm{p}}}{RT} \right) \right). \tag{3.17}$$

where α_n and α_p are the negative and positive charge transfer coefficients respectively. The local exchange current density, i_0 is dependent on both Li and bulk electrolyte concentrations,

$$i_{0\_i} = F(k_i)^{\alpha_i}(1 - \bar{c}_i)^{\alpha_i}(\bar{c}_i)^{1-\alpha_i} \left(\frac{c_{b0}}{c_{b0,ref}} \right)^{\alpha_i} \tag{3.18}$$

where the subscript i is n or p depending on the interface, $c_{b0,ref}$ is a initial reference SE concentration, $\bar{c}_i = \frac{c}{c_{\max}}$ where c is the Li concentration and $c_{\max}$ is the maximum Li concentration in the NE or PE and the rate constant (k_i) expressed as k_p and k_n for the PE and NE respectively. The total overpotential η_{i}, is expressed as,

$$\eta_{\mathrm{i}} = \varphi_{\mathrm{i}} - \varphi_{\mathrm{b}} - U_{\mathrm{i}} - \frac{\Omega_{\mathrm{i}} \sigma_{\mathrm{H,i}}}{F} \tag{3.19}$$

where U_i is the open circuit voltage, and additional overpotentials due to diffusion-induced hydrostatic stress $\sigma_{H,i}$ and the initial partial molar volume Ω_i, are incorporated via the final term on the right-hand side of Equation 3.19.[108]

3.2.5 Boundary and initial conditions

Consider the coordinate system (x, y, z) in Figure 3.1. At the positive CC, a current density is applied: $\boldsymbol{i}_{cc} \cdot \boldsymbol{n}_{cc,p} = i_{in}$ at $x = (t_{cc,n} + t_{ne} + t_{sep} + t_{pe} + t_{cc,p})$, where $\boldsymbol{n}_{cc,p}$ is the unit normal vector pointing outwards from the positive CC surface in the positive z-direction. The applied current density i_{in} at 1C discharge, is calculated based on the sub volume of the cell. Since the maximum accepted quantity of Li for the given electrode material, $c_{p,max}$: the current density is given as $i_{in} = c_{p,max}FV_p/t_0A$, where the area is in the dimensions of the cell in the z, y coordinates, $A = zy$, V_p is the volume with $V_p = zyx$ and $t_0 = 3600$ s. At the negative CC, a potential of $\varphi_p = 0$ V is applied at $x = 0$.

The thin film SSB is prescribed to be fixed in all directions to the positive CC surface, i.e. $\boldsymbol{u}_{cc} \cdot \boldsymbol{n}_{cc,p} = 0$ at $x = (t_{cc,n} + t_{ne} + t_{sep} + t_{pe} + t_{cc,p})$, whilst the negative CC surface remains unconstrained. Given that a small sub volume of the electrode is modelled in the y-direction, it is appropriate to apply symmetry boundary conditions for species fluxes, displacements and potentials.

At the interface between the separator and the electrodes, the electronic current flow is specified to be zero: $\boldsymbol{i}_i \cdot \boldsymbol{n}_{sep,i} = 0$, where $\boldsymbol{n}_{sep}$ is the unit normal vector to the interface between the electrode and the separator, pointing in the direction away from the electrodes. This ensures that only the ionic current is permitted across this interface. At the electrolyte-electrode interface a flux of Li into the electrode is observed, or Li^+ ions into the electrolyte as a result of the charge transfer reaction. The fluxes are as follows: $\boldsymbol{J}_b \cdot \boldsymbol{n}_{sep} = -i_{BV}/F$ and $\boldsymbol{J}_i \cdot \boldsymbol{n}_i = -i_{BV}/F$, where $\boldsymbol{n}_i$ is the normal vector pointing from the electrolyte to the electrodes. A current density is also prescribed at this interface: $\boldsymbol{i}_b \cdot \boldsymbol{n}_{sep} = -i_{BV}$ and $\boldsymbol{i}_i \cdot \boldsymbol{n}_i = -i_{BV}$. An initial Li concentration in the electrodes, c_{i0}, is prescribed, whilst the initial concentration

in the electrolyte is given by c_{b0}. The electrode and all associated constituent domains are assumed to be in an initially unstressed state.

To summarise, the strain type simulated in the SE and PE domain is linear elastic whereas for the NE (*a*-Si) an elastic-viscoplastic behavior is modelled. The three types of strains occurring within the NE are elastic, volume-preserving plastic, and lithiation-induced deformation gradients. The PE and SE are not expected to plastically deform due to their higher Young's modulus and hardness even at full lithiation.

3.3 Numerical methods

3.3.1 Material parameters

The mechanical and electrochemical parameters used in the model were either previously reported values from the literature or experimentally determined in this study (Table 3.1). LCO and LiPON were assumed to be isotropic linear-elastic solids, whereas *a*-Si was treated as an isotropic elastic-viscoplastic solid with a Li concentration-dependent Young's modulus and yield strength as defined in Equation 3.12. The elastic properties of *a*-Si vary with state of lithiation (SoL) during cell cycling. The Young's modulus and Poisson's ratio vary between the elastic limits of pure Li and *a*-Si depending on SoL. This produces a non-linear trend which is captured in the model (a detailed explanation of these parameters can be found in the study by Leo et al.[34]). The CCs were assumed to be electronically conductive, linear elastic solids with Young's moduli of ≈100 GPa. Finally, the universal gas constant, R was taken as 8.314 J mol^{-1} K^{-1}, and all simulations and experiments were carried out at a temperature, T of 298 K.

Table 3.1 *Model parameters*

		Parameter	Units	Value	Source
Electrochemical	SE Diffusion coefficient	D_b	m^2 s^{-1}	1.7×10^{-16}	Ref [109]

	Initial SE concentration	c_{b0}	mol m^{-3}	1000	--
	Max PE concentration	$c_{p,max}$	mol m^{-3}	5.19×10^{4}	Ref [23]
	Max NE concentration	$c_{n,max}$	mol m^{-3}	1.55×10^{5}	Calculated
	Initial NE concentration	c_{n0}	mol m^{-3}	$0.05\times c_{Si,max}$	--
	Initial PE concentration	c_{p0}	mol m^{-3}	$0.95\times c_{LCO,max}$	--
	Charge transfer coefficient	α_n, α_p	1	0.5	--
	SE Ionic conductivity	K_b	S cm^{-1}	2.3×10^{-6}	EIS
	NE Electronic conductivity	K_n	S cm^{-1}	0.33	Ref [110]
	PE Electronic conductivity	K_p	S cm^{-1}	1×10^{-5}	Averaged from ref [107]
Elastic	PE Young's modulus	E_p	GPa	191	Ref [107]
	PE Young's modulus	E_n	GPa	$f(c_n/c_{n,max})$	Ref [34]
	SE Young's modulus	E_b	GPa	77	Ref [111]
	PE Poisson's	υ_p	1	0.24	Ref [107]

	ratio				
	SE Poisson's ratio	υ_b	1	0.25	Ref [111]
	NE Poisson's ratio	υ_n	1	$f(c_n/c_{n,max})$	Ref [34]
	NE Partial molar volume	Ω_n	$m^3\ mol^{-1}$	8.8×10^{-6}	Ref [112]
	PE Partial molar volume	Ω_p	$m^3\ mol^{-1}$	-1×10^{-7}	Ref [25]
Plastic (Si)	Strain fitting parameter	σ_0	GPa	0.9	Ref [103]
	Strain fitting parameter	σ_{sat}	GPa	0.4	Ref [103]
	Plastic strain rate	$\dot{\varepsilon}$	s^{-1}	2.3×10^{-3}	Ref [103]
	Strain fitting parameter	c_*	1	0.04	Ref [103]
	Stress exponent	nr	1	2.94	Ref [103]
Rate kinetics	NE/PE Rate coefficient	k_n, k_p	$mol\ m^{-2}\ s^{-1}$	1.3×10^{-5}	Obtained from 1C cycling data
	PE OCV	U_p	V	$f(c_p/c_{p,max})$	Ref [23]

Electrochemical properties often vary as a function of composition. The diffusion coefficient was experimentally estimated as a function of SoC for *a*-Si and LCO using GITT. Diffusion through the SE was given by D_b, reported by Raijmakers et

al.[109] The initial concentration of Li^+ ions, c_{b0} was parametrised in the study to give the best fit to the experimental 1C data. The maximum concentration $c_{Si,max}$ of Li in Li_ySi was estimated using the equation: $c_{Si,max} = y\rho_{Si}$. Here y represents the Li stoichiometry in Li_ySi and ρ_{Si} is the theoretical maximum molar density of the hosting material. By analysing the quantity of Li extracted from LCO during charging, the amount of Li alloyed with the *a*-Si electrode was calculated. The upper voltage limit was 4 V and by extrapolation to the open circuit voltage (OCV) of LCO, the amount of Li extracted from LCO, y was quantified. It should be noted that the value of y must be normalised by the LCO thickness.

3.3.2 Simulation and validation details

The 2D echem-mech model was created using the finite element modelling software package, COMSOL Multiphysics (v5.6, Sweden). The 2D geometry in this study is used to model the mechanical properties in the *x*-*y* plane. The mesh consisted of approximately 4,000 quadratic elements with 94,000 degrees of freedom, while the solutions were found to be mesh independent. The Parallel Direct Sparse Solver (PARDISO) was used to solve the discretised transport, electrode kinetics and deformation kinematics equations. A segregated approach was used, which involved solving the coupled field variables in a sequential staggered manner. Time stepping was handled using 2nd order backward Euler differentiation, whilst time step sensitivity analysis was performed.

3.4 Experimental Design

3.4.1 Experimental set-up

A commercial thin-film SSB was supplied by a UK battery manufacturer. The cell had a capacity of 250 µAh, comprising of an *a*-Si NE, a LiPON SE and a crystalline LCO PE sputtered on top of a substrate using vacuum processing methods. A test rig was set up at Imperial College London for thin film SSB cycling to extract parameters for model validation (Figure 3.2a). The rig consists of housing

the SSB inside a thermal chamber (Binder) which controls the temperature. A thermocouple was attached to the cell as is standard practice holding it in place using Kapton tape. The temperature of the cell was monitored by the thermocouple readings recorded using a data logger (PicoLog TC-08) and the cell was cycled using a potentiostat (Biologic EC-lab), the cables of which were pulled through a circular hole (located at the back) and was covered with thermal foam that was held with aluminum tape for thermal insulation. The SSB cell was mounted on a printed circuit board with embedded electrical connections and an illustration of the expanded cell components can be seen in Figure 3.2b.

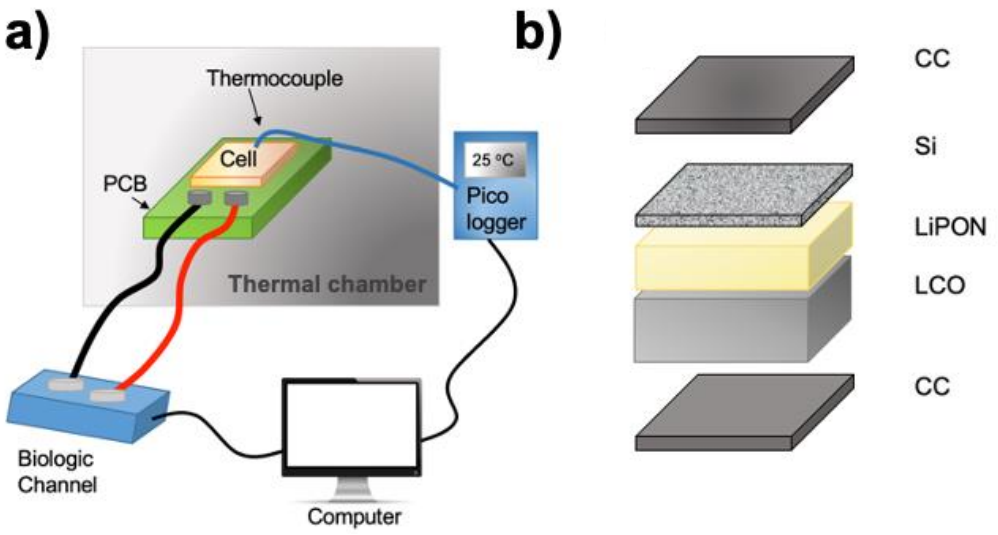

Figure 3.2 a) Schematic of test rig set up and **b)** illustration of expanded cell components.

3.4.2 Cell Formation and Steady State Electrochemical Tests

The cell was formed using five charge/discharge cycles at C/5 and differential capacity ($\frac{dSoC}{dV}$) analysis (DCA) performed to reveal electrode processes. Differential capacity analysis is a widely used tool to characterise the state of health of a battery by identifying various peaks in the DCA curves that correspond to phase changes of the active materials during charge and discharge. Differential capacity is the differential of the capacity (or interchangeably the state of charge, which is the capacity divided by the full cell capacity) and the voltage. The PE and

NE contribute to the full cell DCA in an additive manner. Therefore, comparing the DCA peaks of the full cell can be compared to the half-cell, where any differences in peak positions, height and area can point to different degradation mechanisms. If the height of the peaks decreases and shift towards higher or lower voltages depending on charging and discharging respectively, it indicates a loss of lithium inventory likely due to a decomposition layer forming on either electrode. The shift in voltage of the electrodes relative to one another indicates electrode slippage which subtly changes the shape of the voltage versus capacity curve. The electrode slippage is another indicator of side reactions at either electrode causing the capacity alignment of the electrodes to shift.[113] If, however, there is a decrease of peak height at approximately constant voltage, this is likely due to loss of active material for example transition metal dissolution or lattice collapse of the PE.[114,115] The total peak area of charge should equal discharge for the case there is no full cell capacity loss. A reduction in discharge peak relative to charge peak and vice versa, indicates loss of lithium due to side reactions.

In the thin film SSB case, the ($\frac{dSoC}{dV}$) analysis of the full cell contains information from both electrodes, therefore comparison with half-cell data from literature was used to assign the peak contributions from the *a*-Si and LCO as it was not possible to make half-cells (specialist vacuum deposition equipment for SSB synthesis was not available, nor was the company willing to disclose the vacuum processing conditions).[107,116] Si DCA peaks can vary largely depending on whether it is amorphous or crystalline and the vacuum processing parameters. The ($\frac{dSoC}{dV}$) data (Figure 3.7) was compared during the first formation cycle (C/5)and after subsequent cycling at 1C and only tentative peak assignment of the PE and NE contributions could be conducted. Of interest was the formation cycle where first cycle losses as a result of side reactions could be detected by investigating differences in peak area on charge versus discharge.

OCV as a function of SoC was determined for the formed full cell after relaxation for 24 hours at 10% capacity increments. A pseudo-OCV was measured using a small cycling current of C/30. EIS measurements were taken at each 10% SoC

interval after 24 hours relaxation during charge and discharge. During EIS, a 5 mV voltage perturbation and a frequency range of 1 mHz to 1 MHz were used. Nyquist plots (-Im(Z) vs. Re(Z)) were fitted with an equivalent circuit model (ECM) using ZView software (Scribner Associates).

When conducting linear EIS, two conditions must be obeyed: i) the form of the input and output functions must be the same, and ii) must be linear to ensure that higher harmonic terms are avoided, as these represent irreversible electrochemical changes to the system.[117] In order to ensure these conditions were obeyed, a Kramers-Kronig (K-K) relation was applied to test the linearity, stability and causality of the EIS data. From the impedance spectra, the ionic conductivity, (K_{b}) of LiPON was calculated as an input for the echem-mech model using:

$$K_{\mathrm{b}} = \frac{\mathrm{t_{sep}}}{A_{\mathrm{sep}} R_{\mathrm{b}}} \tag{3.20}$$

where, A_{sep} is the surface area of the SE, and R_{b} is the bulk resistance of the SE taken from the ECM of the EIS data.

To separate polarisation contributions from the various cell components and identify all time processes in the system, a Fourier transform of the EIS data was performed for DRT analysis by,[23,118]

$$Z(w) = R_{\mathrm{ohmic}} + Z_{pol}(w) = R_{\mathrm{ohmic}} + \sum_{i=1}^{N} \frac{R_{\mathrm{pol,k}}}{1 + j\omega\tau_k} \tag{3.21}$$

where R_{ohmic} is the Ohmic resistance of the SSB and is independent of frequency, while $Z_{pol}(w)$ accounts for the polarisation resistance, $R_{pol,k}$ and is a function of frequency. This deconvolution is possible since the different cell processes have characteristic frequencies, and therefore time constants, associated with specific processes (Table 3.2). MATLAB code by Wan et al.[118] was used to perform DRT

analysis. The K-K residual plots of EIS data were ±1% (Figure A.1 and Figure A.2 in the Appendix).

Table 3.2 *Characteristic time scales in the SSB*

Approximate Time Constant (s)	Cell Process Assignment	Source
2×10^{-6}	LiPON ionic migration	Ref [119]
5×10^{-5}	Li_ySi|LiPON interface	This study
3×10^{-4}	Li_ySi|*a*-Si interface	This study
3×10^{-3}	LiPON|LCO charge transfer	Ref [119]

3.4.3 Pulsed electrochemical tests

The EIS "tail" (impedance at ~45° at low frequencies >~1 Hz on the Nyquist plot) is an indication of diffusion processes. However, the thin film SSB EIS data at low frequencies was not stable over different SoC ranges (10-90%), hence an alternative method was employed to extract the diffusion coefficient. The GITT method was used to analyse the total Li^+ ion diffusion of the full cell at different SoCs. GITT method is not routinely used for thin film SSBs, and a study by Pang et al.[23] conducted on a thin film Li-based SSB, was therefore used as a guide for GITT

testing. As the focus of this work is to evaluate the dynamic SSB behaviour under pulse conditions, it is fitting that the diffusion coefficient is estimated using the GITT pulse method and across a range of SoC values for charge and discharge. This is because diffusion coefficients extracted using the EIS technique are taken at OCV (equilibrium conditions), where no current is passed through the cell which contrasts with GITT where a small current pulse is applied. Hence, a difference in diffusion values can occur between these measurements and implies that the diffusion behaviour within the NE and PE has a complex dependency on the cell usage and operation.

Figure 3.3 shows the schematic of a typical GITT pulse procedure, where ΔV_t is the voltage response due to the applied current pulse (calculated after subtracting the initial *IR* drop due to internal cell resistance) and the subsequent voltage relaxation, ΔV_s.

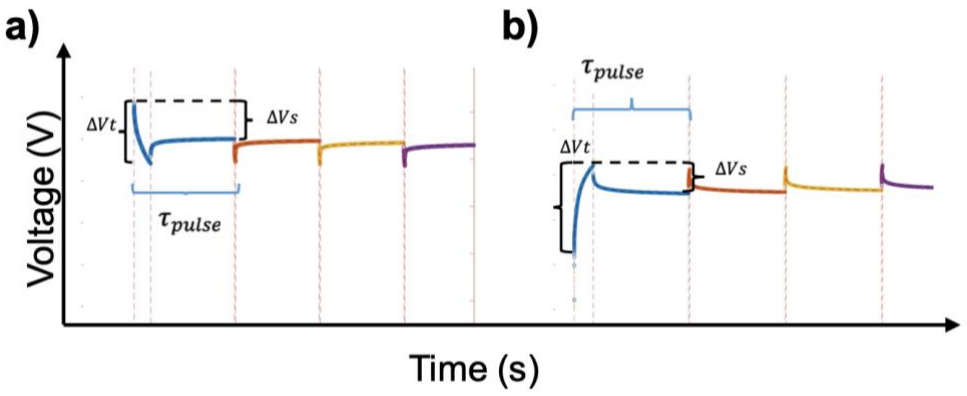

Figure 3.3 GITT pulses and extraction of diffusion coefficient using $\Delta \boldsymbol{V_t}$ and $\Delta \boldsymbol{V_s}$ from the pulse profile, **a)** for GITT discharge pulses and **b)** charge pulses.

This method was used to estimate the cell diffusion coefficient, D_{cell} using the equation:

$$D_{\text{cell}} = \frac{4}{\pi \tau_{pulse}} {t_{\text{elec}}}^2 \left(\frac{\Delta V_{\text{s}}}{\Delta V_{\text{t}}}\right)^2 \qquad (3.22)$$

where τ_{pulse} is the time period of the GITT pulse and t_{elec} is the electrode thickness. This equation is valid for $\tau_{\text{pulse}} << \frac{t_{\text{elec}}{}^2}{D_{\text{cell}}} 120$ where the ratio of these values was on the order of ~ 10^5 s. In these experiments, 20 s (<< ~ 10^5 s) was used for the pulse duration, followed by a relaxation to OCV. The GITT pulses were carried out at 10% SoC intervals and the diffusion coefficients were calculated at these points.

In this configuration, the different electrode contributions are convoluted. To estimate the individual electrode contributions, the PE and NE contributions were scaled by their respective charge transfer resistances, which were determined using DRT analysis (Equation 3.21). These estimates of the diffusion coefficients in each electrode were used as parameters in the model. The diffusion coefficient for the extracted PE (LCO) was found to lie within the same order of magnitude compared to that of Pang et al.[23] which was also extracted using the GITT method.

3.4.4 Load testing

HPPC testing was performed to probe the dynamic cell behaviour over usable voltage ranges. The test is used to determine the cell power capability, incorporated over a range of SoCs during charge and discharge. Various short current pulses are applied to the cell, thereby a relatively short charge/discharge load is subjected to the battery and is followed by a regenerative pulse (discharge/charge) to recover the capacity lost during the load pulse. An ECM can be fit to the pulse to deconvolute the resistances that occur within the cell at different SoCs and under which mode of operation these resistance increase/decrease (e.g., on charge versus discharge). By assigning time domains to the resistive processes, information about the cell's resistance contributions can be deduced. The HPPC method is rarely reported for SSBs, however studies have been carried out on LIBs to characterise the resistances as HPPC is able to mimic the drive profile of an EV. From these tests, the response of the LIB can be analysed under these 'real world' cycling profiles. These types of pulse tests are important as we look to commercialise SSBs and should be applied to these systems.

The full HPPC protocol is illustrated in Figure 3.4 and yielded three discharge and charge datasets. Prior to the first HPPC discharge, the cell is charged to full capacity: constant current up to 4V and constant voltage until current drops below 1C. This state (considered 100% SoC) is used as the datum for coulomb counting through all subsequent HPPC tests.

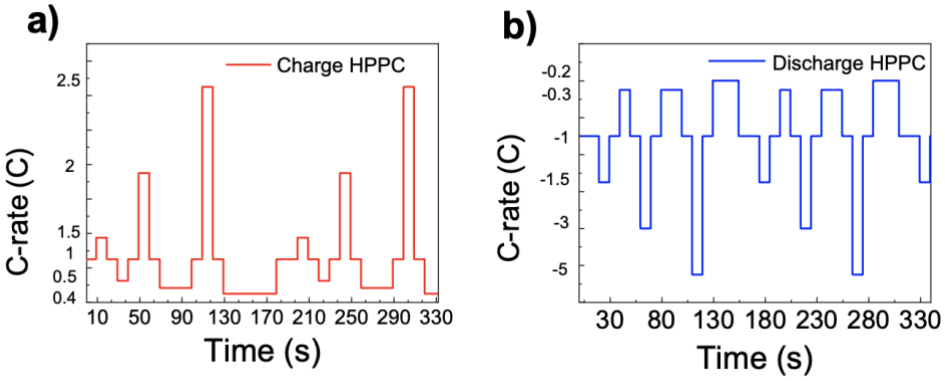

Figure 3.4 Example current pulse profiles for **a)** charge HPPC and **b)** discharge HPPC.

The loaded HPPC procedure, in discharge and charge, consists of six pulses of varying magnitude, separated by a 10 s, 1C load period. The six pulses may be described in two sets: three "high" C-rate pulses, for example 1.5C, 3C and 5C, which have a 10 s duration, and three "low" C-rate pulses to ensure the time averaged (dis)charge rate is 1C. To this end, the low C-rate pulses vary in magnitude and duration, depending on the nature of the "high" C-rate pulse magnitudes. In charge, the cell may not be charged at greater than 2.5C, imposing an upper limit on the possible pulses that may be employed. The magnitudes and order of the pulses were varied from one discharge to the next, and from one charge to the next, in order to create variability in the extracted parameter datasets. The steps of the procedure are repeated until the cell's voltage limit is reached (2.9 V in discharge or 4 V in charge), which is the end criteria for the single HPPC test. Figure 3.4 a and b show example loaded HPPC procedures for charge and discharge respectively.

The HPPC results were used to parameterise the Thevenin ECM (Figure 3.5) to extract the RC parameters. The first order Thevenin ECM consists of a resistor

in series with two parallel resistor/capacitor (RC) pairs. Separate sets of parameters were developed for discharge and charge.

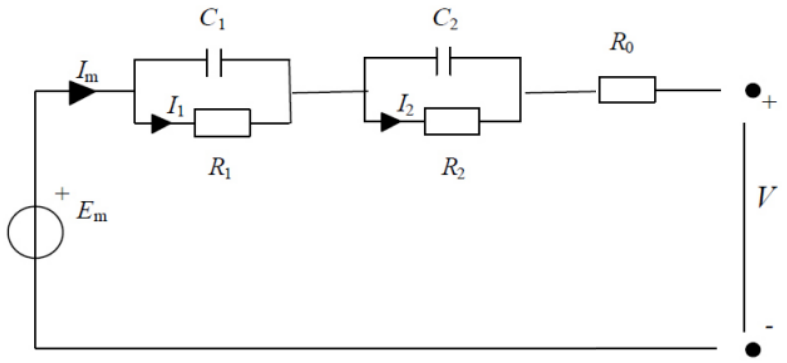

Figure 3.5 Thevenin equivalent circuit model containing two RC pairs.

Parameter extraction was conducted using a script developed in-house, which uses the MATLAB curve-fitting toolbox to fit the ECMs response (i.e. simulated terminal voltage) to the experimental voltage data through a least-squares optimisation method. The methods for extraction follow well established processes, as set out by Ahmed et al.[121] and Jackey et al.[122,123] ECM parameters vary considerably with cell SoC and therefore 5% SoC windows (i.e., 100-95%, 95-90%, etc.) were used to extract unique parameters which describe the cell's behaviour for specific SoC ranges.

The simulated terminal voltage (V_t) at any timestep was described by Equation 3.23,

$$V_t = U - R_0 I - \sum_{i=1}^{n} U_i \, U_{RC,} \tag{3.23}$$

where the cell OCV, U is a function a given SoC, R_0 is the series (Ohmic) resistance due to the bulk SE impedance R_{bulk}, U_i is the voltage drop across the ith RC pair, n is the total number of RC pairs (n = 2 for the purposes of the present study where, R_{elec} is the lumped charge transfer resistance of the electrodes and R_{diff} is the diffusion resistance) and I is the magnitude of current flow.

The modelled versus experimental HPPC fit can be seen in Figure 3.6 a and b for charge and discharge respectively. The rms error is <15 mV, with the largest error at the start of charge/discharge due to OCV estimation error.

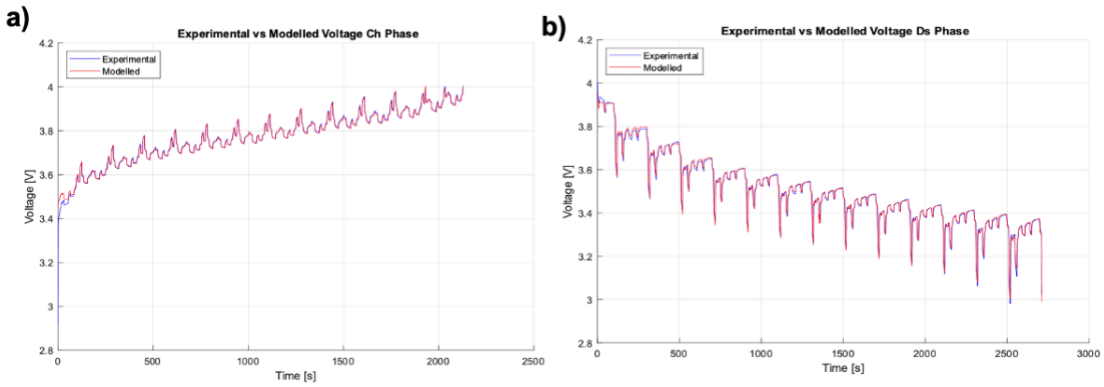

Figure 3.6 Experimental vs. modelled (using the ECM in Figure 3.5) voltage profile for the **a)** charge and **b)** discharge HPPC profile.

3.5 Results and Discussion

3.5.1 Formation cycles

The voltage profiles of the 5 initial charge cycles at C/5 showed a sharp "knee-point" at ≈3.65 V (Figure 3.7a). Using differential capacity analysis (Figure 3.7b), this feature was attributed to a characteristic LCO phase transformation observed previously[107] and a broad peak due to *a*-Si lithiation to Li_2Si could also be assigned,[116] consistent with *a*-Si not being fully lithiated to $Li_{15}Si_4$ over the voltage range used here.

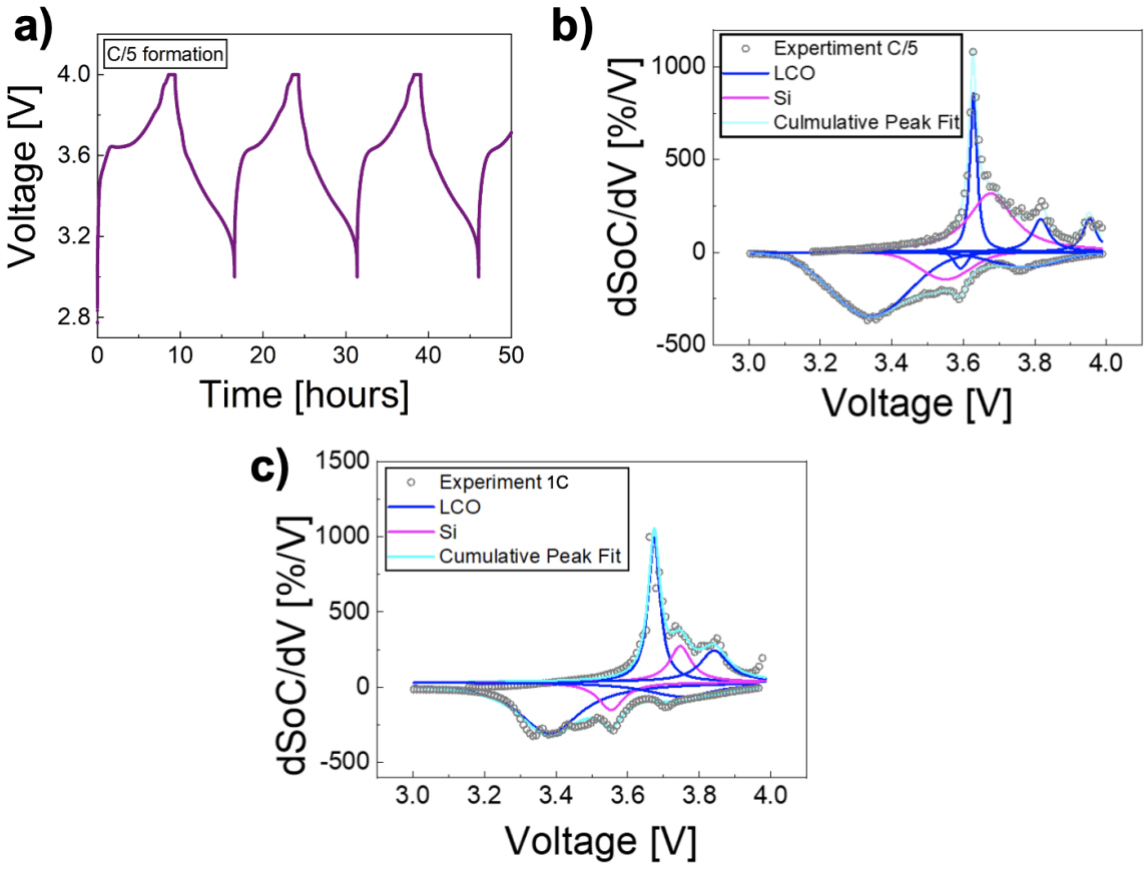

Figure 3.7 **a)** Voltage profiles of C/5 formation cycles. Differential capacity analyses of **b)** formation cycle at C/5 and **c)** after formation cycles at 1C.

A decrease in the peak area is observed and attributed to the *a*-Si electrode on discharge, likely due to side reactions consuming Li during the alloying reaction with *a*-Si on formation, as has been observed in a previous full cell study.[124] Conversely, the differential capacity analysis for 1C cycling post-cell formation (Figure 3.7c) showed the peak areas attributed to LCO and *a*-Si to be near equal between charge and discharge – indicative of stable cycling.

3.5.2 Electrochemical testing

Experimental tests consisting of OCV and low current (C/30) cycling measurements post-formation were used to determine the SoC-OCV relationship

and cell capacity respectively. During the OCV testing, a voltage hysteresis was observed between charge and discharge (Figure 3.8a), which is commonly seen for *a*-Si-based half-cells.[125] An increased voltage hysteresis was observed during low current (C/30) cycling (Figure 3.8b) compared with OCV and was attributed to the hydrostatic stress caused by diffusion induced strains (Equation 3.6) as a result of lithiation and delithiation of the *a*-Si electrode. This was consistent with the expected viscoplastic behavior.

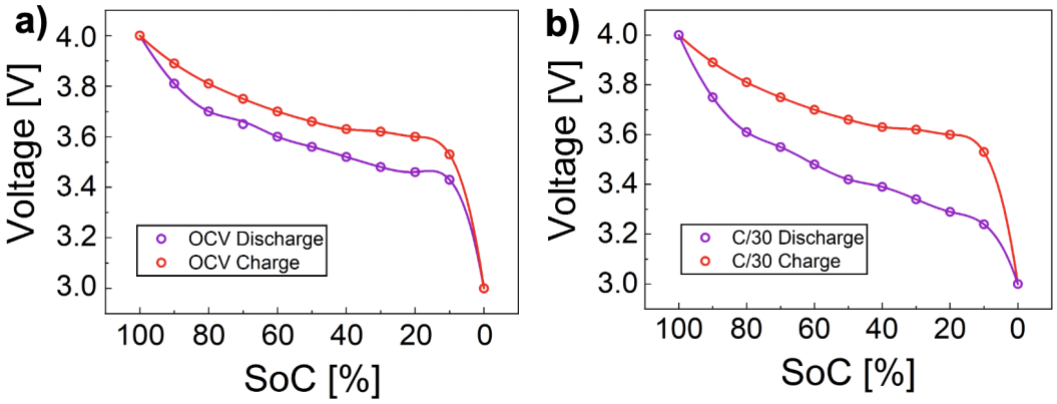

Figure 3.8 a) OCV curve on charge and discharge, with 24 hours relaxation between SoC points, **b)** C/30 cycling. Voltage hysteresis between charge and discharge was observed in both cases.

3.5.3 Electrochemical impedance spectroscopy and distribution of relaxation times analysis

EIS showed two semi-circles in the high and mid-to-low frequency regions on a Nyquist plot. There was very little variation in the Nyquist spectra during charge and discharge (Figure 3.9) thus minimal information could be determined about the internal cell impedances from EIS alone.

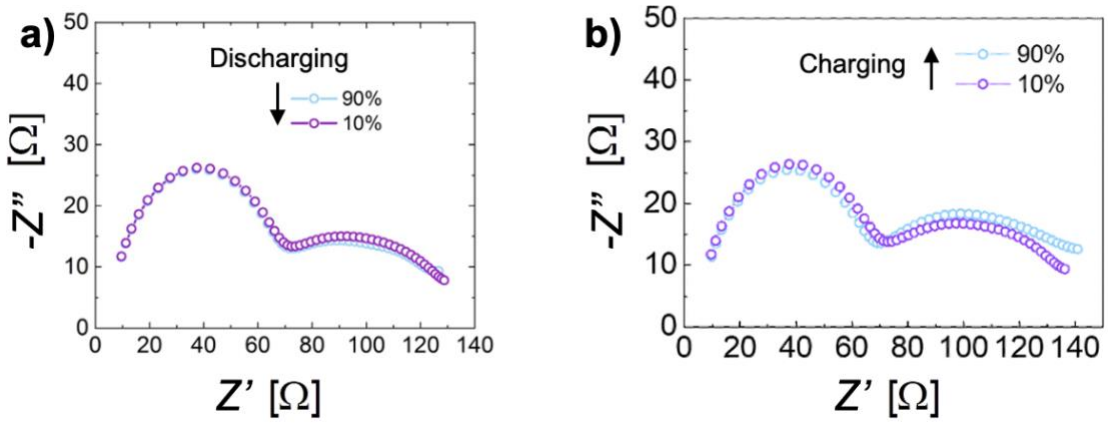

Figure 3.9 EIS **a)** discharge and **b)** charge for 10% and 90% SoC.

A representative plot at 50% SoC is shown in Figure **3.10**. As the latter semi-circle was substantially depressed, the possibility that this feature was made up of multiple polarisation processes using DRT analysis was investigated.

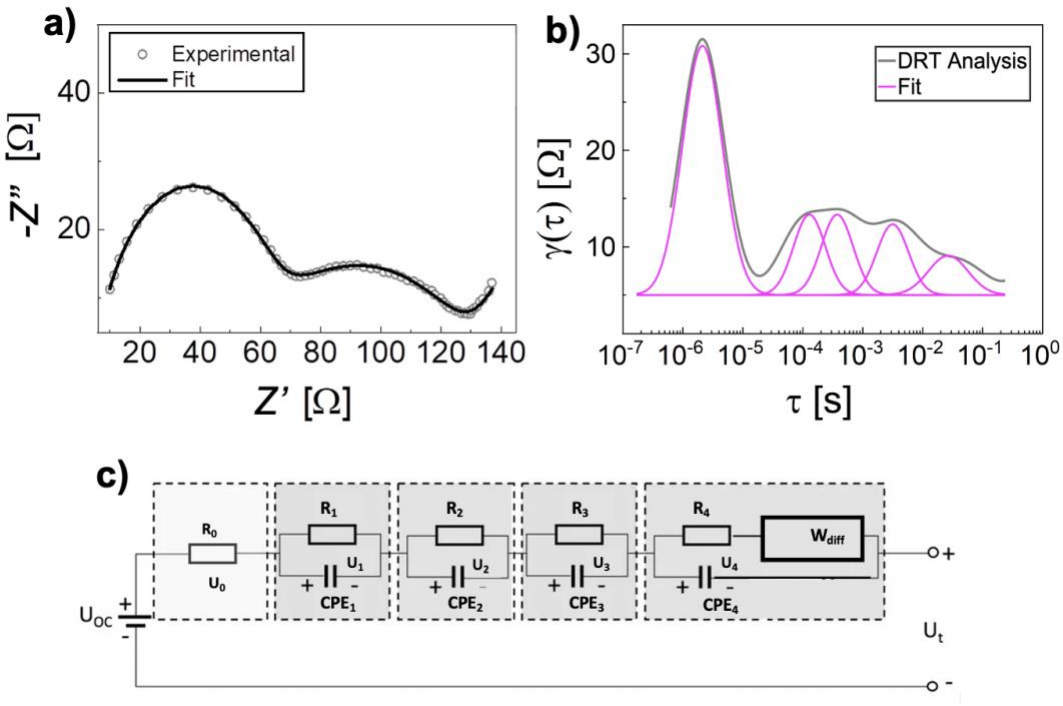

Figure 3.10 For the discharge case at 50% SoC, **a)** representative EIS, **b)** deconvoluted DRT spectra showing five polarisation processes (x and y axes are not made equal for clarity) and **c)** the ECM used for the EIS fitting in **a).**

From the DRT spectrum (Figure **3.10**b), several distinct polarisation processes were identified. The peak observed at ≈10^{-6} s was attributed to ion migration in the LiPON SE and was largely invariant during operation as expected. At the other end of the spectrum, the peak at ≈0.1 s was assigned to relatively slow diffusion processes and exhibited a complex dependance with SoC. As low frequency EIS measurements can be unreliable, time-domain experiments were used to deconvolute and quantify individual electrode contributions to the diffusion polarisation in these cells (Section 3.5.5).

Intermediate polarisation processes in the range 10^{-5} to 10^{-2} s were attributed to charge transfer contributions at the various cell interfaces. Based on previous reports, a single LiPON|LCO time constant was expected to occur at ≈10^{-3} s (Table 3.2), [23,119] thus, the peaks at ≈10^{-5} and ≈10^{-4} s were attributable to the *a*-Si electrode. The exact meaning of these processes is not known, but it is speculated that they may result from the Li_ySi alloy at the SE| *a*-Si interface and the additional interface between lithiated Li_ySi and unlithiated *a*-Si in the electrode bulk. This picture is consistent with partial *a*-Si lithiation during operation and the differential capacity analysis which hinted at irreversible Li loss after the first formation cycle (Section 3.5.1).

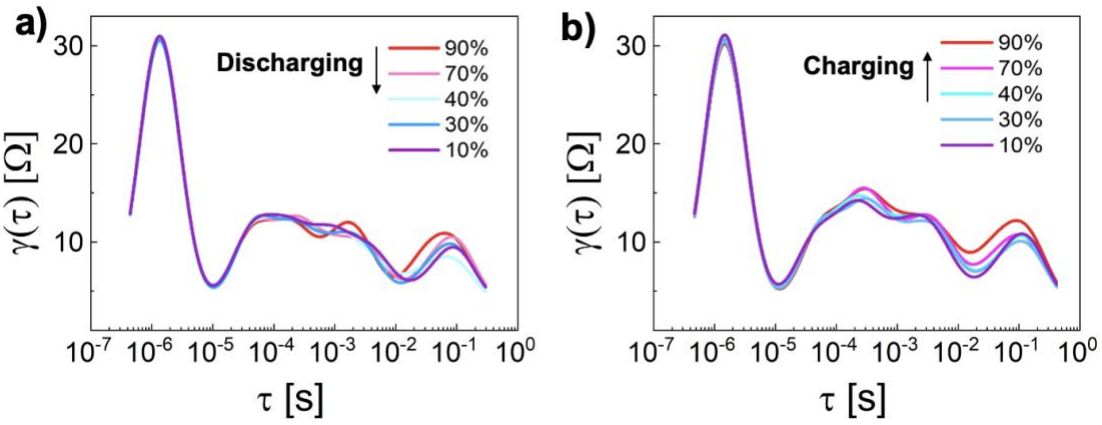

Figure 3.11. DRT spectra during **a)** discharge and **b)** charge for various SoC values.

During charge and discharge, the SE|LCO polarisation was approximately constant, as was the *a*-Si electrode process centred around ≈10^{-5} s (Figure **3.11**). In contrast, the *a*-Si contribution at ≈10^{-4} s was invariant on delithiation but increased during lithiation. The observed increase in charge transfer resistance may be due to the swelling of *a*-Si as it lithiates to Li_ySi. Therefore, the following preliminary assignments are made: the faster interfacial process (≈10^{-5} s) represents the SE|Li_ySi interface, while slower charge transfer (≈10^{-4} s) occurs between Li_ySi and bulk *a*-Si.

The five polarisation processes revealed by DRT analysis were incorporated into an ECM that fit the EIS data well as shown in Figure **3.10**c. The ionic conductivity of LiPON was calculated using the value of R_1 obtained from the ECM fit and inputted into Equation 3.20, which was in good agreement with literature values.[23] DRT analysis also allowed quantification of the electrode resistances during charge and discharge, which were used to estimate Li diffusion coefficients for individual electrodes from full-cell GITT data in the following section.

3.5.4 Galvanostatic intermittent titration technique

From experiments using GITT the total cell diffusion was extracted. The Li diffusion coefficients, D_{GITT} in the *a*-Si and LCO electrodes were estimated for charge and discharge as explained in Section 4.3. The D_{GITT} value in *a*-Si was determined to be ≈2 orders of magnitude smaller than the D_{GITT} value in LCO (Figure 3.12).

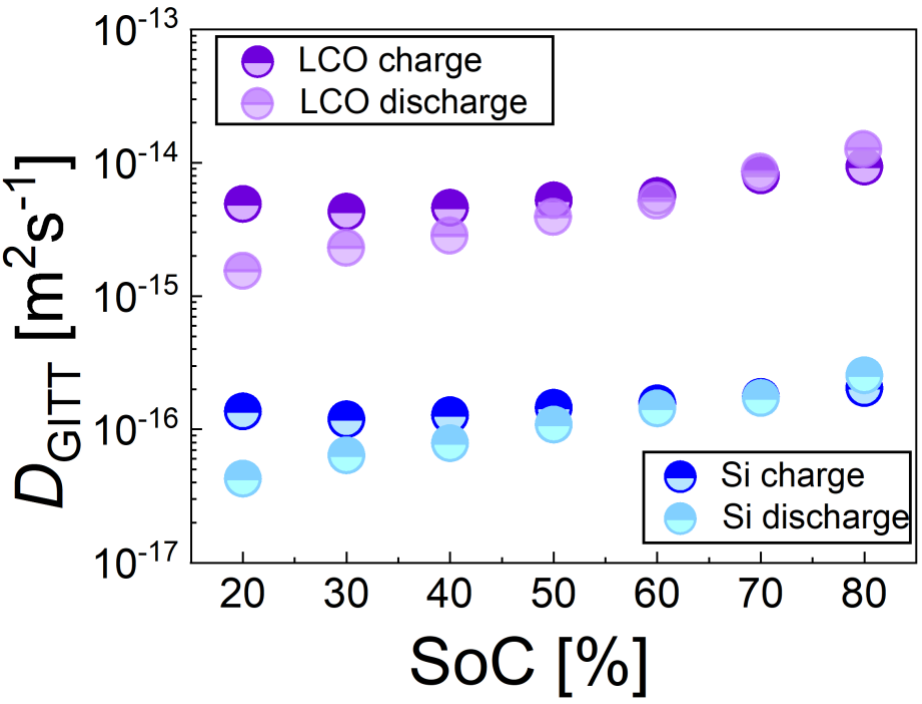

Figure 3.12 Solid-state diffusion coefficient values estimated for LCO and *a*-Si during charge and discharge using the relative polarisation contributions from DRT analyses.

For the charge case at low SoC, D_{GITT} was fairly constant but gradually increased from mid to high SoC. A similar trend was found for diffusion on discharge, though a reduction in D_{GITT} was more pronounced in the low SoC region at the end of discharge. This behaviour could be due to hindered extraction of Li^+ ions from *a*-Li_ySi with low Li content. Similarly, the reduced D_{GITT} value in LCO at low SoC on discharge relative to charge can be explained by the intercalation of Li^+ ions into LCO being impeded by a high Li concentration at the LCO|SE interface.

3.5.5 Hybrid pulse power characterisation

HPPC was conducted, and the resultant voltage profile was fit to two parallel *RC* units in series. The following *R* values were extracted as a function of SoC: R_{bulk}, R_{elec} and $R_{diff.}$. Figure 3.13 shows their behaviour during charge and discharge. The charge profile was diffusion-limited especially at high SoC and the resistance associated with the SE, R_{bulk}, remained approximately constant over the SoC range

whereas the charge transfer resistance, R_{elec} had a complex dependence on SoC. However, during discharge there was high diffusion resistance at the SoC extremes but was overall limited by the slow electrode kinetics (higher R_{elec}) at low SoCs with R_{bulk} remaining approximately constant over the SoC range. This observation is in contrast with the EIS results at steady state which showed the charge transfer resistances to be near equal at different SoC points (Figure **3.10**). If the increase in interfacial resistance R_{elec} was due to irreversible side reactions or a stable decomposition layer, then this should have been apparent in the EIS data (which were measured after HPPC pulsing). Rather, these results suggest that the increase in diffusion impedance, R_{diff} during pulsing was a transient cell response that was due to diffusion limitation in the electrodes (increase in R_{diff}) and mechanical stress due to the build-up of concentration gradients at the SE|electrode interface (increase in R_{elec}).

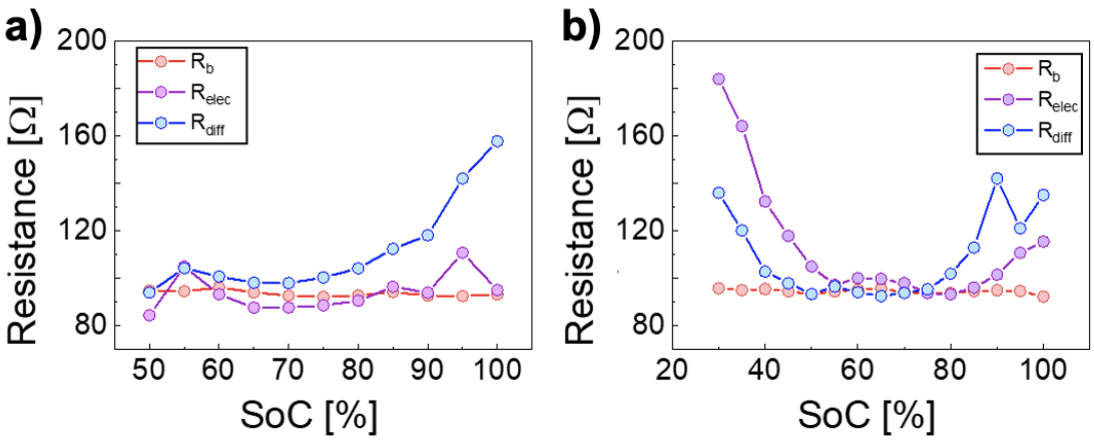

Figure 3.13 Resistance values extracted from hybrid pulse power characterisation profiles during **a)** charge and **b)** discharge.

While diffusion limitations at low SoC during discharge were in agreement with the GITT results, those observed during charging at high SoC were not. Thus, the dynamic cell behaviour is highly complex, especially in the case of charging when *a*-Si strain is increasing. It is possible that the time constants of charge transfer and diffusion processes overlap and therefore R_{elec} and R_{diff} cannot be solely attributed

to one or the other, rather one may dominate in certain time domains. Two additional HPPC measurements for charge and discharge were conducted and used for model parameterisation and validation against the experimental data as shown in Figure 3.14.

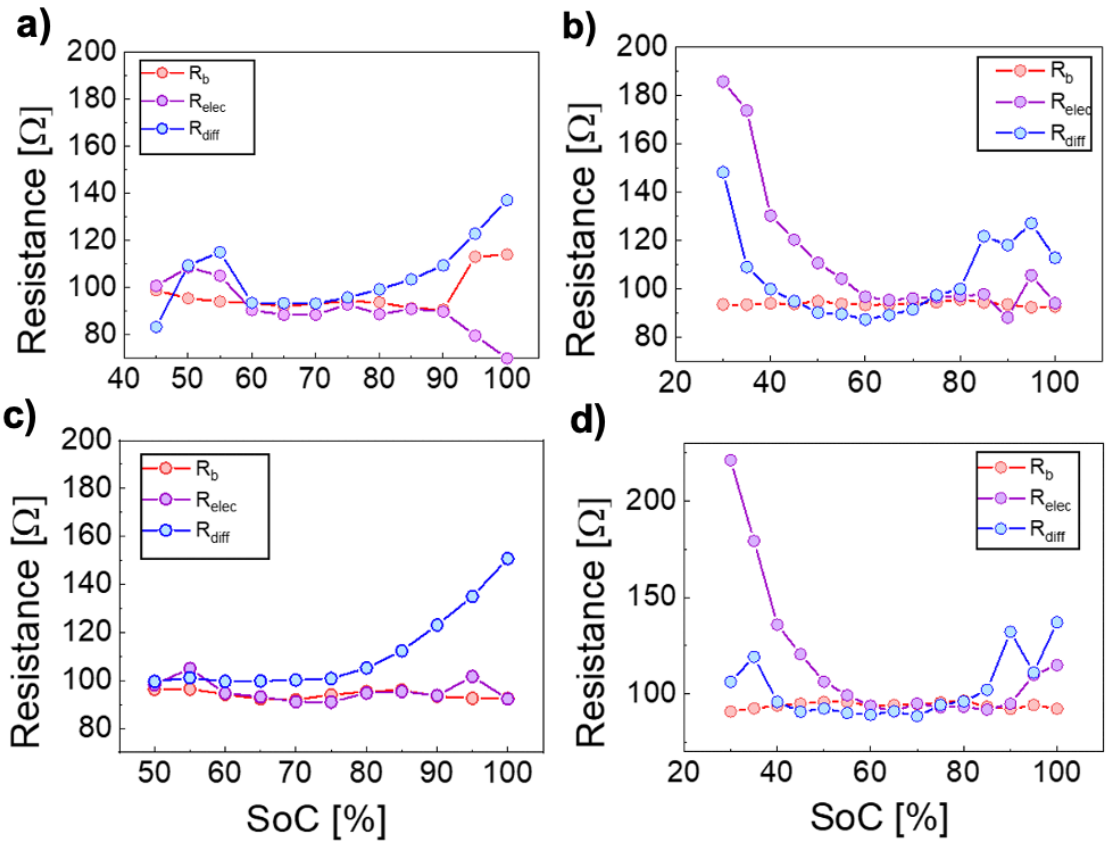

Figure 3.14 HPPC using profile 2, **a)** charge and **b)** discharge. HPPC using pulse profile 3, **c)** charge and **d)** discharge.

These followed similar trends, which was expected for pulses at similar C-rates. An acceptable root mean square (rms) error of <15 mV (predicted by the Thevenin model, see Figure 3.5) was obtained.

3.5.6 Model validation

The echem-mech model was validated using experimental charge and discharge curves, both taken at a 1C rate. Figure 3.15 shows a comparison between these experimental data and two simulation cases using different values of the Li^+ ion diffusion coefficient, *D* for the electrode materials, as elaborated below.

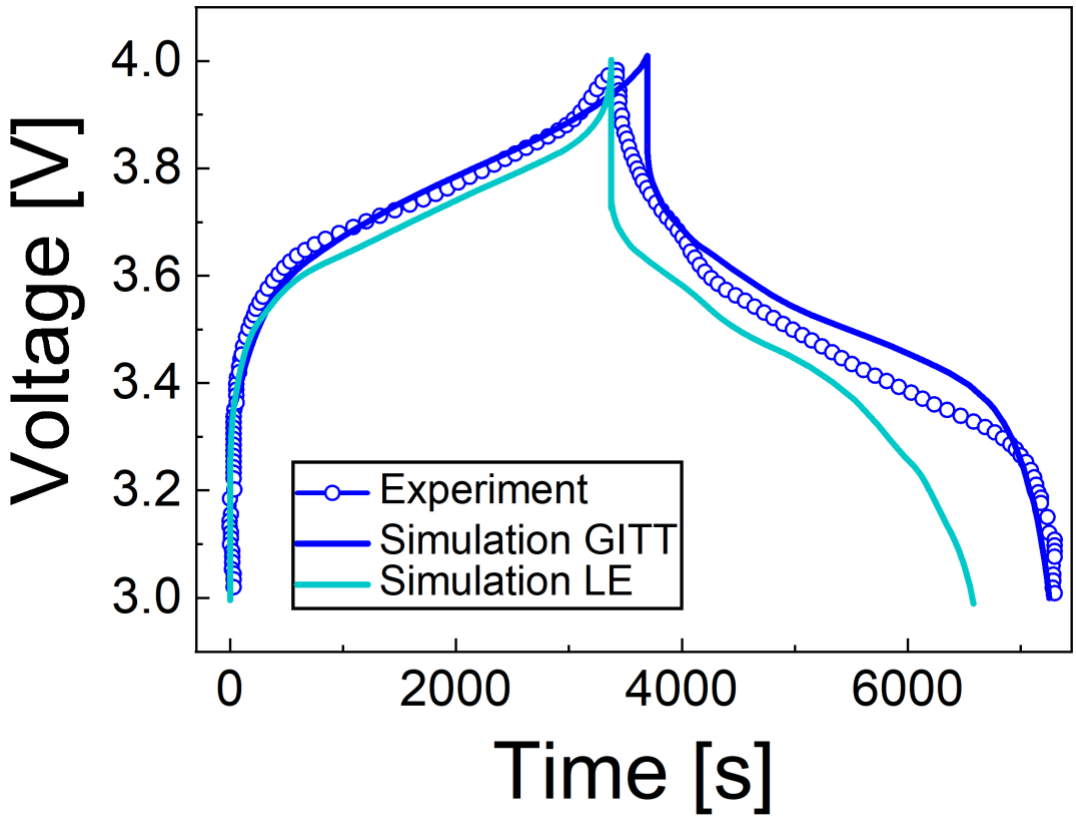

Figure 3.15 1C charge/discharge data compared with simulations using experimentally determined diffusion coefficients using GITT versus values from half-cells with a LE.

In the first case (Figure 3.15, light blue trace), the *D* values for LCO and *a*-Si used in the model were based on half-cell experiments using LE reference data (supplied by a commercial SSB manufacturer). Although good agreement between experiment and simulation was observed on charge, significant deviations (>200

mV) were apparent on discharge and the discharge capacity was severely underpredicted. In the second case (Figure 3.15, dark blue trace), D_{GITT} values for LCO and *a*-Si were estimated using full-cell GITT data (Section 3.5.5), modified by the total electrode charge transfer resistances (quantified by DRT analysis in Section 3.5.4). The inclusion of these parameters markedly improved the agreement with experiment on discharge, accurately predicting cell capacity and highlighting the importance of accurate diffusion coefficient values when modelling these systems.

The remaining discrepancies between model and experiment during cycling were primarily attributed to uncertainties in the OCV values of *a*-Si and LCO, which were extracted from half-cell data using a LE. When a LE is used, the electrodes can expand freely with minimal constraint. In contrast, the SSB considered in the present study uses a SE that may influence electrode response, e.g., volumetric expansion may be limited by the high Young's modulus of the SE. Given that there will be a change in the stress and strain fields, the OCV is likely to be affected. Representative solid-state half-cell data are therefore highly desirable for future SSB modelling studies.

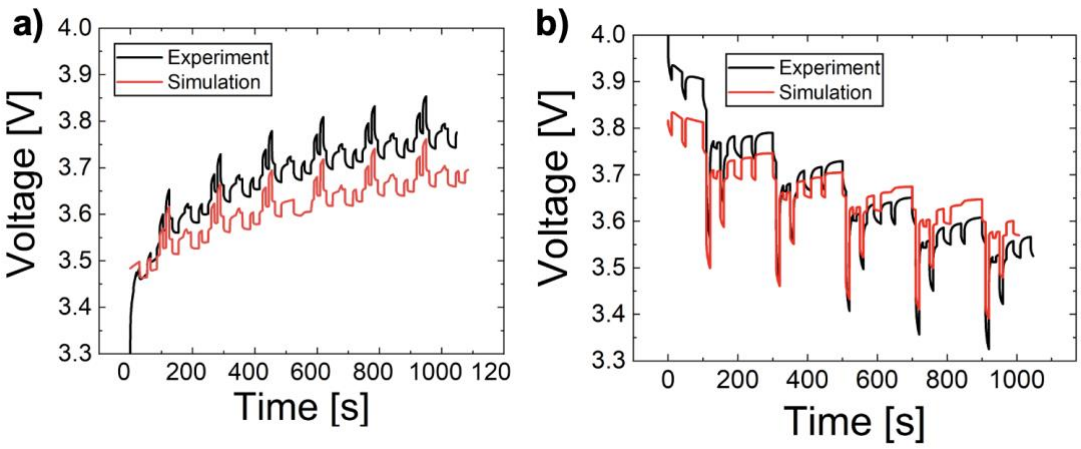

Figure 3.16 Experimental and simulated HPPC profiles for **a)** charge and **b)** discharge.

The model was further validated against charge and discharge during HPPC (Figure 3.16). The HPPC simulations followed the profile and general trend of the

experimental data well, deviating by a maximum value of ≈100 mV. These offsets can be explained by considering the simulated 1C charge data in Figure 3.16, which did not perfectly capture the "knee point" at high SoC. It is speculated that this difference has also translated into the HPPC charge profile as a voltage offset. During discharge, the initial pulse was captured as a sharper drop in voltage than observed experimentally, again consistent with the 1C discharge data (Figure 3.15). It can be concluded that the model reproduced the pulse behaviour of the cell with further improvement being possible with more accurate experimental parameters extracted from representative half-cell OCV and GITT data.

3.5.7 Electrode thickness effects

Increasing electrode thickness is desirable to maximise cell capacity but may compromise power capability. In order to aid SSB design, the effects of electrode thickness on stresses and strains in *a*-Si -based, thin-film SSBs was studied. Maps of maximum principal nominal strains and stresses (which both occurred at the SE|Li_ySi interface during 1C cycling) as a function of relative electrode thickness were created using the developed model.

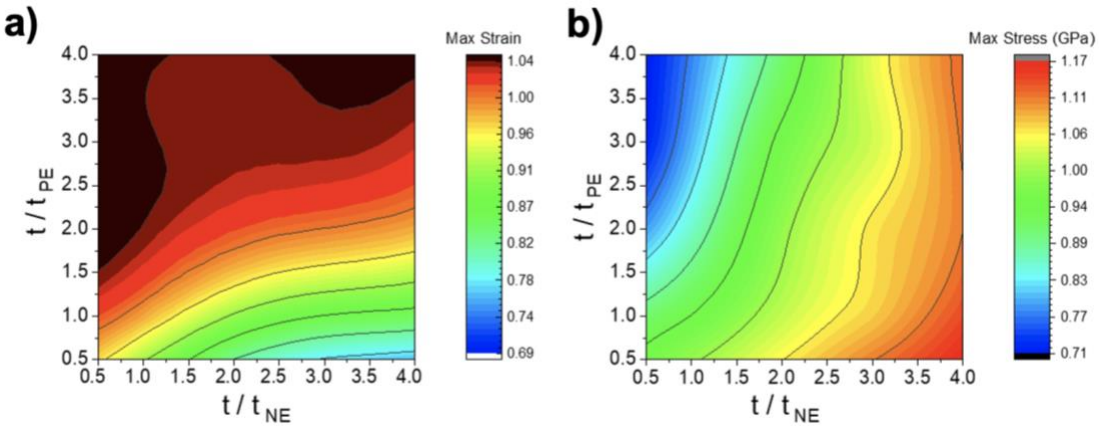

Figure 3.17 Illustrates maps of SSB **a)** strain and **b)** stress as a function of varying PE and NE thicknesses against the nominal thickness *t, t/*t_{NE} and *t/*t_{PE} respectively.

Figure 3.17 illustrates the tradeoff that exists in terms of limiting the maximum stress and volumetric expansion. As the electrode thickness ratio (nominally a negative to positive electrode thickness ratio of 1:1) was increased to 4:1, the model predicted a maximum strain of -13% and a maximum stress of +30%. By targeting a thicker *a*-Si electrode, which can incorporate more Li, the strain is reduced provided the LCO electrode remains relatively thin, i.e. the degree of *a*-Si lithiation remains relatively low. However, this direction may not be practical from an application perspective, as the cell capacity is limited by the LCO and scales linearly as a function of LCO thickness. For thicker LCO layers, the increase in the total Li available results in a greater degree of lithiation in the *a*-Si, and hence greater strain. Tailoring the relative electrode thicknesses compared to the nominal 1:1 up to a factor of 1:4 (negative to positive electrode thickness ratio), resulted in increased stress from 0.71 GPa up to 1.17 GPa, corresponding to a volumetric expansion from 69% to 104%. The model showed that stress and strain variations are heterogenous in the cell, with the SE|Li_ySi interface experiencing the greatest stress. Thus, a thin *a*-Si electrode coupled with a thick LCO electrode would be desirable to minimise overall stress. Although this results in a highly lithiated and highly strained *a*-Si electrode, a lower concentration gradient was produced resulting in more a homogenous stress distribution while maximising cell capacity. From Figure 3.13, it can be deduced to optimise for both stress and strain, a NE to PE ratio of ~1-1.5 (NE) to ~0.5-1 (PE) is desirable.

3.6 Conclusion

This study has presented experimental characterisation of a commercial thin-film SSB which was used to parameterise and validate a 2D echem-mech model. First, differential capacity analysis during first cycle formation was suggestive of a thin Li_ySi layer forming at the *a*-Si|LiPON interface. The voltage hysteresis observed during OCV and C/30 cycling was attributed to due to diffusion induced stress, highlighting the role of mechanical properties in this system even at low C-rates. DRT analysis was used to guide the interpretation of EIS, which displayed 5

different time processes occurring within the SSB. Two polarisation processes were assigned to the *a*-Si electrode, possibly due to a Li_ySi alloy layer at the *a*-Si|SE interface and an additional interface between this layer and unlithiated *a*-Si in the electrode bulk. This picture is consistent with partial *a*-Si lithiation during operation and irreversible Li loss after the first formation cycle. The diffusion coefficients of *a*-Si and LCO were estimated using the GITT and the pulsed behaviour of the SSB probed using HPPC. HPPC revealed the complex behaviour of the diffusion and electrode resistances as a function of SoC which was not observed during steady-state EIS measurements.

Several experimental parameters extracted from these tests were inputted into the model for validation. It was found that the use of solid-state diffusion coefficient values from half cells using a LE resulted in unsatisfactory agreement with charge/discharge data, while those determined using the GITT on the full cell SSB reproduced the cell capacity during 1C cycling and response during HPPC. The simulation could be further improved by obtaining more accurate experimental parameters for the diffusion coefficient and OCV values. Additionally, electro-mechanical studies of solid-state half-cells (*a*-Si|LiPON|Li metal), e.g. using curvature measurements as have been performed on *a*-Si half cells with LEs[16, 17] would be beneficial for future modelling efforts.

Finally, the model was used to investigate the stress-strain behaviour when electrode thicknesses were varied. A trade-off between limiting the maximum stress and limiting cell expansion was shown. The recommendation from this study is to initially satisfy the required cell capacity by the LCO thickness, followed by using the thinnest *a*-Si layer possible to accommodate Li. This would minimise the stress at the SE|Li_ySi interface and hence the possibility of fracture and delamination. Whilst this would result in increased interfacial strain, this may be mitigated by engineering the Li_ySi|SE interface or applying external pressure. In the next chapter, this thesis will focus on the relationship between applied pressure and C-rate on the stress-strain response of the SSB. In addition, the mechanical properties of suitable SE candidates that enables a reduction in strain at the Li_ySi|SE interface will be probed.

It is noted that the model used an unconstrained *a*-Si electrode for simplicity. In practice this will not be the case, as the top CC and casing will constrain expansion to some extent. As the maximum stress is experienced at the SE|Li_ySi interface, it is critical that the SE mechanical properties are tailored to reduce the *a*-Si stress and be sufficiently mechanically strong to withstand the stresses occurring during cycling, otherwise fracture propagation may occur under high tensile stress and cause cell failure.

Chapter 4

Effects of Pressure and C-rate on the Stress-Strain Response of the Solid State Battery Model

This chapter is adapted from the work published in "Vadhva P, Boyce A, Patel A, Shearing P, Offer G, Rettie A. Silicon-based Solid-State Batteries: Electrochemistry and Mechanics to Guide Design and Operation. ChemRxiv. Cambridge: Cambridge Open Engage; 2023."

Contribution Statement: Model simulations and data analysis was conducted by P. Vadhva with advice and direction from A. Boyce, G. Offer and A. Patel. Funding acquisition by A. Rettie and P. Shearing.

4.1 Introduction

Chapter 3 demonstrated an experimentally validated echem-mech model of a Si thin film SSB. However, the electrochemical and mechanical interplay was not explored, nor was the dependency of externally applied pressure or C-rate. The sensitivity of SE materials and mechanical parameters on rate performance as a function of applied pressure is poorly understood nor is the severity of the complex stress field generated during (de)alloying at the Si|SE interface. Further, the influence of applied pressure and C-rate on the SSB voltage profile, build-up of concentration gradients within the SSB domains and stress-strain response is not fully understood.

This work delves deeper into this to understand the influence of these parameters in order to guide cell material design.[33] The thin film SSB model consists of *a*-Si NE, LiPON SE and LCO PE. First, the effect of SE mechanical properties and kinetics on first cycle efficiency are explored. Next, maximum principal stress and strains are observed at the SE|NE boundary which is used to generate a map of stress and strain as a function of C-rate and applied pressure. Finally, the effect of different SE material selection on the cell stress-strain response is discussed and used as a guide to lay out the desired SE mechanical properties for optimal cell performance.

4.2 Model Formulation

A schematic of the thin film SSB is depicted in Figure 4.1a, highlighting the reaction and solid-state transport equations in each domain. The schematic illustrates the CCs, *a*-Si (NE), the SE separator and LCO (PE) with only the SE being altered during the material design study. The thickness of the CCs, *a*-Si, SE and LCO are represented as t_{cc}, $t_{sep,}$ t_{ne}, and t_{pe} respectively, while Figure 4.1b shows the applied pressure to the top of the cell and fully clamped conditions at the bottom of the cell, i.e., at the CC adjacent to the PE. An orthogonal coordinate system (Figure 4.1a) is used to define the thickness x, length y and width z of the SSB. Li transport occurs in 1D, while deformation is assumed to be a plain strain.

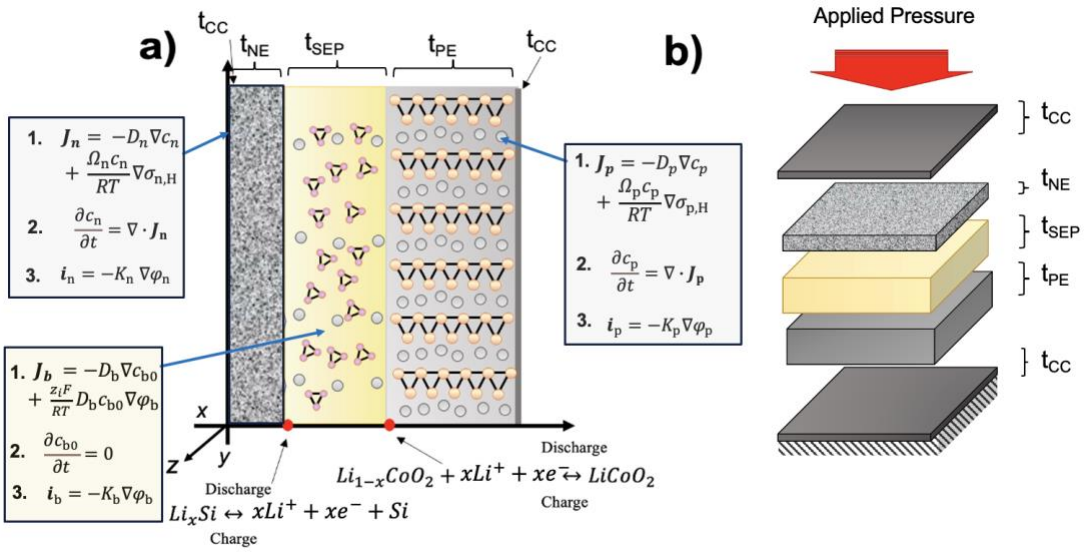

Figure 4.1 a) 2D thin film SSB schematic, with the relevant electrochemical equations highlighted in each domain. **b)** 3D SSB schematic displaying externally applied pressure to the top of the NE CC with the entire cell fixed at the bottom.

4.2.1 Material parameters and boundary conditions

For the baseline case, the cell configuration was *a*-Si NE, LiPON SE and LCO PE. In this work, the SE material was varied, and the mechanical and electrochemical parameters used are recorded in Table 4.1. Here, the ionic conductivity, elastic modulus and yield strength are denoted as K, E, σ_Y respectively, with the subscript relating to the type of SE material. The chosen sulfide and oxide SE materials were LPSCl and $Li_{6.4}La_3Zr_{1.4}Ta_{0.6}O_{12}$ (LLZTO) respectively. Both are commonly used SEs with relatively high ionic conductivities, and their mechanical properties and internal yield behaviour have been characterized by Papakyriakou et al.[126] where LPSCl and LLZTO were found to exhibit viscoplastic creep behaviour with a creep rate coefficient, B (sec^{-1}) and stress exponent, n_{SE} (Table 4.1). A Chaboche-type equation (see Equation 3.11) to model the viscoplasticity is used herein however, the experimental post-yield

stress-strain response of these SE materials has not yet been reported to the best of our knowledge.

Table 4.1 *Solid electrolyte material parameters*

		Parameter	Units	Value	Source
Electrochemical	Ionic conductivity LiPON	$K_{\_LiPON}$	S cm^{-1}	2.3×10^{-6}	Ref [119]
	Ionic conductivity LPSCl	$K_{\_LPSCl}$	S cm^{-1}	2.9×10^{-3}	Ref [126]
	Ionic conductivity LLZTO	$K_{\_LLZTO}$	S cm^{-1}	5.9×10^{-4}	Ref [126]
Elastic	Young's modulus LiPON	$E_{\_LiPON}$	GPa	77	Ref [111]
	Young's modulus LPSCl	$E_{\_LPSCl}$	GPa	29	Ref [126]
	Young's modulus LLZTO	$E_{\_LLZTO}$	GPa	125	Ref [126]
Plastic	Yield's strength LiPON	σ_{Y_LiPON}	GPa	1.33	Ref [111]
	Yield's strength LPSCl	σ_{Y_LPSCl}	GPa	0.67	Ref [126]

Yield's strength LLZTO	σ_{Y_LLZTO}	GPa	3	Ref [126]
Stress exponent LPSCl	$n_{\_LPSCl}$	1	20	Ref [126]
Stress exponent LLZTO	$n_{\_LLZTO}$	1	45	Ref [126]
Creep rate coefficient LPSCl	$B_{\_LPSCl}$	s^{-1}	6×10^{-4}	Ref [126]
Creep rate coefficient LLZTO	$B_{\_LLZTO}$	s^{-1}	1×10^{-4}	Ref [126]

Treatment of the LiPON SE was extended from an isotropic linear-elastic solid to include plastic deformation. In the absence of mechanical studies on its post-yield behaviour, LiPON was modelled as a perfectly plastic solid. LPSCl and LLZTO were also modelled as elastic-perfectly plastic solids. LCO was assumed to be an isotropic linear-elastic solid, whereas *a*-Si was treated as an isotropic elastic-viscoplastic solid with its Young's modulus, yield strength and Poisson's ratio varying with the state of lithiation (further details can be found in Vadhva et al.[33] and Leo et al.[34]). The CCs were assumed to be electronically conductive, linear elastic solids with Young's moduli of ≈100 GPa. Finally, the universal gas constant, R was taken as 8.314 J mol^{-1} K^{-1}, and all simulations were conducted at a temperature, T of 298 K.

Various boundary conditions were considered to probe the influence of pressure and constraint on electrode behaviour and are outlined as follows:

1. An applied pressure at the CC adjacent to the NE electrode in the range of 0-500 MPa. A fully clamped constraint (zero displacements in x, y, and z) at the CC adjacent to the PE was applied.
2. In a separate study, fully clamped conditions were applied at both CCs to assess the maximum level of constraint.

4.2.2 Simulation details

The echem-mech model was created using the finite element modelling software package, COMSOL Multiphysics (v6.0 Sweden). The 2D mesh consisted of approximately 4,000 quadratic elements with 94,000 degrees of freedom, while the solutions were found to be mesh independent. The Parallel Direct Sparse Solver (PARDISO) was used to solve the discretised transport, electrochemistry, and solid mechanics equations, using the numerical procedure previously outlined.[33]

4.3 Results and Discussion

4.3.1 First cycle efficiency

Under a C/5 C-rate plots for charge-discharge of cycles 1 and 2 of the baseline cell were simulated (Figure 4.2a). Subsequent simulation cycles followed the trend of cycle 2. Two different cases were modelled: 1) Si as an elastic solid (elastic behaviour only, red lines) and 2) Si as a viscoplastic solid (plastic behaviour included into the model, blue lines). There was a pronounced difference in the charge capacities between cycle 1 and 2 for the Si plasticity case and a much smaller difference for the Si elastic case. This points to Si plastic deformation occurring during the first cycle that caused changes in electrode response from the start of charge to the end of discharge, resulting in reduced cell capacity. This observation is in agreement with experimental findings by Han et al.[127] who suggested that the difference in first and second cycle capacity may be due to Si-Si bond breaking and plastic deformation during the first lithiation. It is important to note that the cell capacity increased with the inclusion of Si plasticity given that the plastic

deformation of Si reduces the build-up of stress. The reduction in lithiation-induced stress overpotential reduces the overall cell overpotential, allowing further lithiation before the upper voltage limit is reached.

Incrementing the rate to 1C (Figure 4.2b) while modelling Si as an elastic material resulted in greater first cycle capacity reduction when compared to C/5 cycling, albeit with a lower capacity reduction than when Si plasticity was considered. To understand the cause of this phenomenon, the diffusion of Li in Si, as taken from experimentally extracted diffusion coefficient in literature ($D_{exp} \approx 10^{-16}$ m^2 s^{-1}),[33] was increased by ≈4 orders of magnitude to a hypothetical diffusion coefficient ($D_{hyp} = 10^{-12}$ m^2 s^{-1}). As a result, the difference between first and second cycle capacity was significantly reduced for both the Si elastic and viscoplastic cases (Figure 4.2c) showing the Li-ion diffusion in Si is a limiting factor and that cycling rate greatly influences the electrochemical response. It must also be noted, by extension, that electrode thickness will influence the extent of reduction in first cycle capacity given the transport limitations that are typically associated with thicker electrodes.[128]

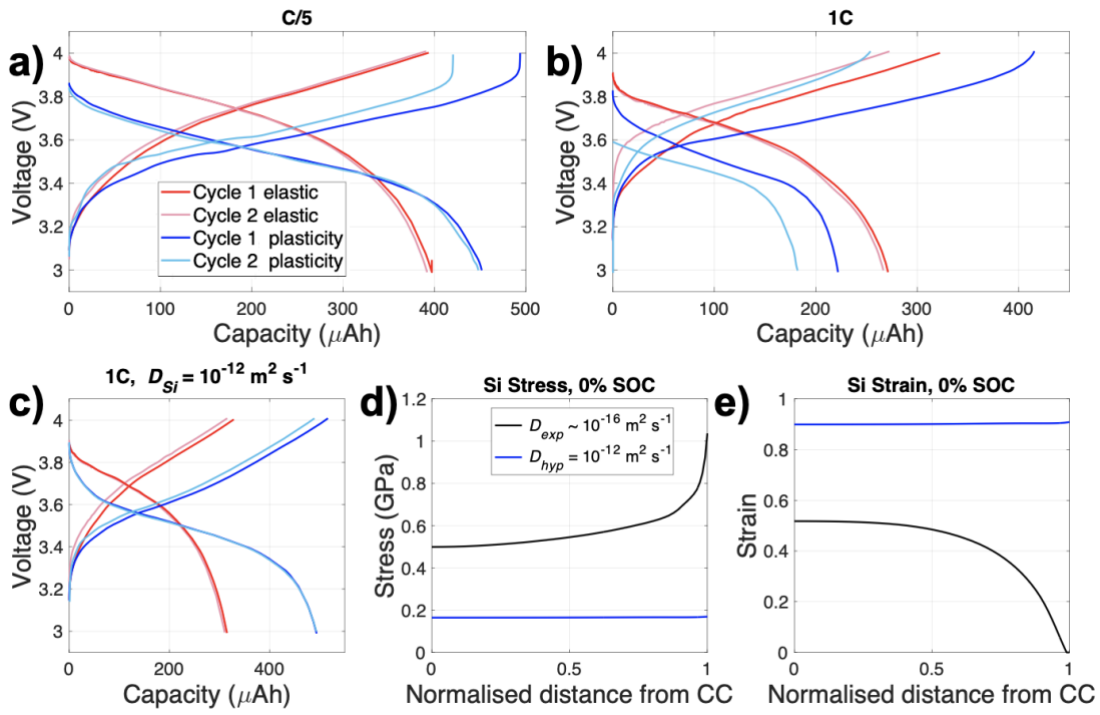

Figure 4.2 **a)** C/5 voltage profile considering Si elastic only behaviour (red) and with the inclusion of Si plasticity (blue). The darker shade indicates the first cycle, whereas the lighter shade represents the second cycle. **b)** Voltage profile at 1C and **c)** with a higher Li diffusion coefficient in Si ($D_{hyp} = 10^{-12}$ m^2 s^{-1}). **d)** Si nominal stress and **e.** nominal strain at 0% SOC, using $D_{exp} \approx 10^{-16}$ m^2 s^{-1} (black) and $D_{hyp} = 10^{-12}$ m^2 s^{-1} (blue). The legend in **a)** applies to Figures **a)** to **c)** whilst the legend in **d)** applies to Figures **d)** and **e).**

Herein it is denoted that 100% and 0% state of charge (SOC) is the end of charge and end of discharge of the first cycle respectively. It should be noted that the stress and strain outlined in this study are always the nominal principal stress and strain. Considering the Si stress and strain at 0% SOC, a much lower tensile stress (Figure 4.2d) was exhibited for the higher diffusion coefficient of 10^{-12} m^2 s^{-1} compared to the experimentally extracted diffusion coefficient (D_{exp}) which is of the order $\approx 10^{-16}$ m^2 s^{-1} depending on the SOC. The observed Si strain was lower than the theoretical maximum strain of 3 (300% volumetric expansion) under the cell voltage cycling limits given that full Si lithiation did not occur. As the extent Si is lithiated is governed by the Li inventory from LCO, the thickness of the LCO

dictated the maximum possible lithiation of Si. When normalising the Si concentration gradient, it was the maximum amount of Si lithiation that was achieved during cycling that was used. Experimental evidence of partial Si lithiation was observed previously using differential capacity analysis for these cells.[33]

The Si strain was considerably greater when the higher diffusion coefficient was implemented (Figure 4.2e), due to increased Si lithiation, which resulted in greater strains but also increased cell capacity. In addition, the Si strain was more homogenous through the electrode than with the slower experimental diffusion coefficient (Figure 4.2e), which can be directly linked to the Li concentration gradients throughout the electrode due to diffusion-related transport limitations. Further, for the Si plasticity case with a faster diffusion coefficient (Figure 4.2c), a much higher first cycle discharge capacity at 1C (≈450 μAh) was displayed than with the experimentally extracted diffusion coefficient (≈225 μAh in Figure 4.2b). The capacity difference between cycles was not as pronounced for the Si elastic case. Therefore, the Li diffusion rate in Si, thickness and the mechanical properties of Si greatly influence the achievable cell capacity and stress-strain response.

4.3.2 Applied pressure

To understand the influence of applied pressure on the electrochemical performance of the baseline SSB, a pressure of 500 MPa was applied. Two C-rates (1C and 5C) were simulated under the applied pressure to observe the evolution of stress and strain in the Si NE. The higher C-rates were chosen to observe how the larger concentration gradients in the Si affected the local stress-strain response. Additionally, the Si stress at 0% SOC under an applied pressure of 500 MPa was compared to the zero-pressure condition for both C-rates. There was minimal change in the stress and strain of LCO during cycling (strain ≈2% in LCO[112]), and so the stress and strain generated in the NE and SE during cycling was focused upon.

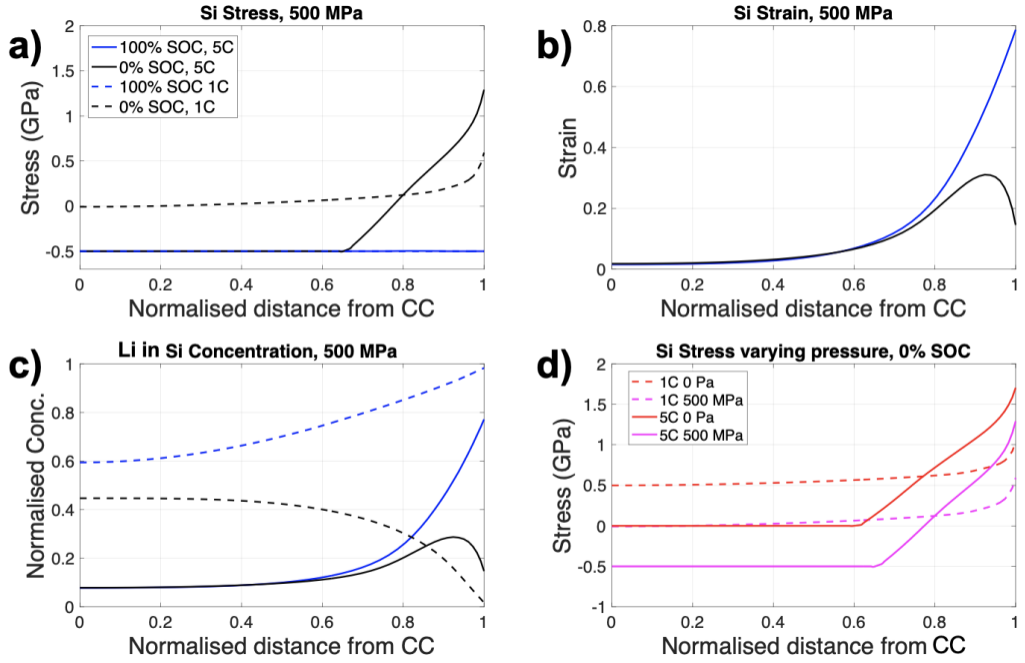

Figure 4.3 Results simulated under 500 MPa applied pressure at 5C (solid line) and 1C (dashed line) at 100% SOC (blue) and 0% SOC (black) showing **a)** nominal stress in Si, **b)** nominal strain in Si, **c)** normalised Si concentration with respect to the maximum acceptable concentration and **d)** nominal stress in Si at 0% SOC with varying pressure of 0 MPa (red) and 500 MPa (purple) at 1C (dashed) and 5C (solid line). The legend displayed in **a)** applies to Figures **a)-c)** with the grey text on top of the figures indicating the cell configuration (e.g., the CC and NE interface (CC|NE) at 0 normalised distance from the CC).

Figure 4.3a shows that at 0% SOC (end of discharge) a larger tensile stress was observed for 5C (black solid line), which occurred near the Si|SE interface, moving to compressive stress further into the Si electrode, towards the CC. This is due to the concentration gradient that is present during discharge and is related to the sluggish solid-state transport of Li^+ ions in Si. This means that towards the Si|SE interface, more Li is removed (reducing the stress) but further into the electrode some Li remains, which produces a lithiation-induced compressive stress. The Si stress for the 1C case at 0% SOC (dashed black line) was more homogenous throughout the electrode with lower tensile stress at the Si|SE interface and a

gradual decrease in stress to zero (no compressive stress observed). At 100% SOC, the Si stress at both C-rates was the same.

The Si strain profile (Figure 4.3b) is analogous to the state-of-lithiation in Si, (Figure 4.3c, normalised with respect to its maximum concentration) because the strain occurs due to the lithiation of Si. At the end of discharge for the 5C case, a local peak in Li concentration and strain occurred at ≈0.9 normalised distance from the CC which was due to slow diffusion upon discharging and the fact that not all the Li was removed. This leads to localised strains at that distance into the electrode. The concentration and strains are highest at 100% SOC due to maximum lithiation and are higher for 1C (dashed blue line) than 5C (solid blue line) due to the slower C-rate allowing greater lithiation. The concentration and strain profiles during 1C cycling were more homogenous throughout the Si than in the 5C case.

Figure 4.3d compares the electrode response with and without applied pressure. The Si stress at 0% SOC highlights the non-linear stress response: for 1C at zero applied pressure (dashed red line), Si exhibits tensile stress towards the CC as a result of delithiation, with a gradual increase in stress due to lower Li content towards the Si|SE interface. At 500 MPa (dashed purple line) however, there is compressive stress due to the pressure that is applied. This external pressure counteracts the tensile stress within the Si electrode due to delithiation and results in an almost stress-free state at the CC, with increasing tensile stress further into the electrode. For the 5C case with no applied pressure (solid red line), there are low concentrations of Li at the CC, causing low, or close to zero stress at this location, with increasing tensile stress through the remainder of the electrode, similar to the 1C case. For the cell simulated at 5C with 500 MPa pressure (solid pink line), the CC region experiences commensurate compressive stress, with tensile stresses developing toward the interface due to high levels of lithiation close to the SE.

To help visualise the compressive applied pressure stress and lithiation-induced stress which is compressive during charge and tensile during discharge, the schematic is presented (Figure 4.4a and b). The build-up of Li concentration gradients within the Si toward end of charge (Figure 4.4a) and end of discharge

(Figure 4.4b) is displayed and used to understand the non-linear stress and strain response displayed in Figure 4.3.

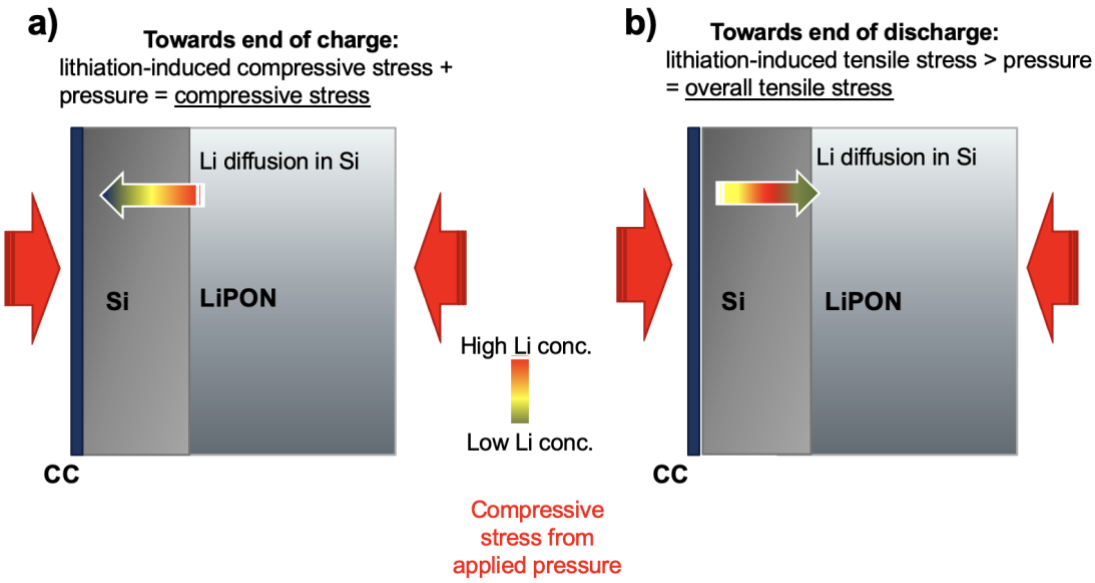

Figure 4.4 Schematic of compressive applied pressure and lithiation-induced stress towards **a)** the end of charge and **b)** the end of discharge. The Li concentration gradient is represented by the arrow's colour gradient with the solid red arrows representing the compressive stress from the applied pressure. The LCO and bottom CC are omitted for clarity, with the dashed black lines representing that the bottom of the cell is fixed.

Under the applied pressure case of 500 MPa, the yield strength of LiPON (1.33 GPa in Table 4.1) was not reached. To explore the effect of LiPON plastic deformation, the cell was simulated as fully constrained to guarantee yielding and cycled at a 1C rate. In this study, the influence of LiPON material response was considered; a comparison was drawn between an elastic material and of an elastic-perfectly plastic response. The Si stress reduced when LiPON plasticity (solid lines) was considered (Figure 4.5a) at 100% and 0% SOC whilst the stress in LiPON increased as a result of plastic deformation for the fully constrained case (Figure 4.5b). The concentration and Si strain remain very similar for both cases (Figures 4.5c and d).

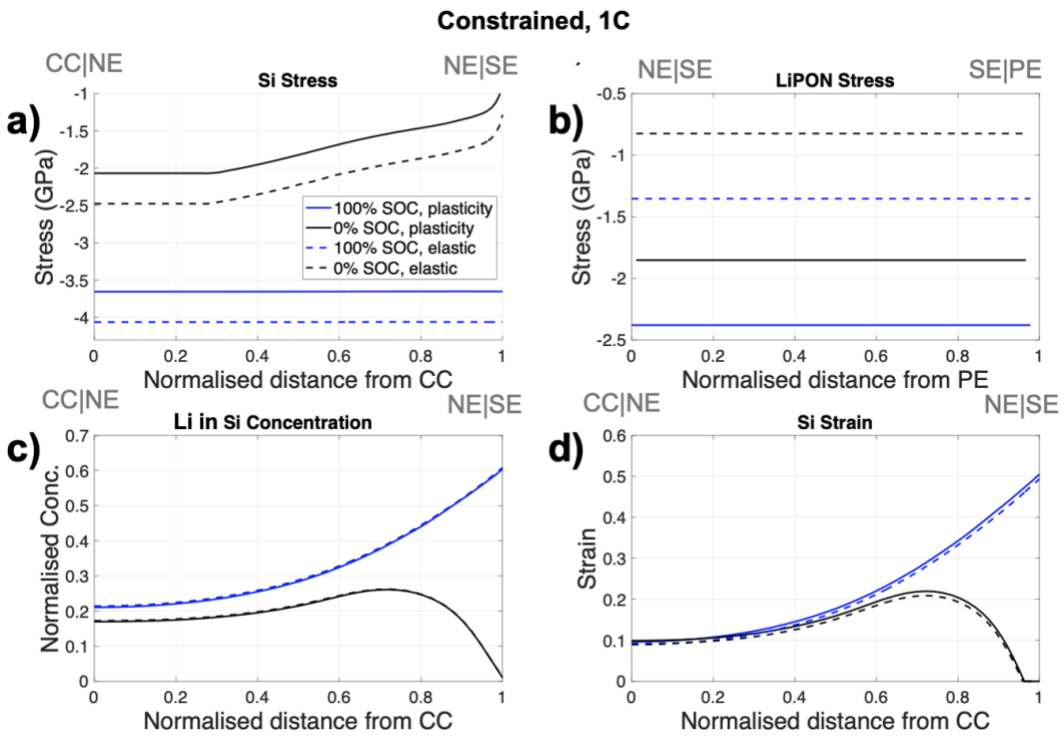

Figure 4.5 Constrained case simulated for LiPON plasticity (solid line) and elastic behaviour only (dashed line) at 100% SOC (blue) and 0% SOC (black) showing **a)** Si stress, **b)** LiPON stress **c)** Si concentration and **d)** Si strain. The legend displayed in **a)** applies to all figures with the grey text on top of the figures indicating the cell configuration.

To understand the effect of applied pressure and C-rate on the cell capacity, a map was generated where five C-rates under five pressure values were simulated, with intermediate values determined by linear interpolation. Figure 4.6 shows a map of the maximum principal strains that occurred at the Si|LiPON interface. As the C-rate increased, the stress overpotential became larger, reaching the maximum cell voltage quicker, thereby reducing the overall capacity. Note that the average capacity discussed in this section and in Figures 4.6 and 4.7 is an average of the cell's charge and discharge capacities. As the C-rate increases, the lower degree of lithiation also reduces the maximum principal strain (black contours in Figure 4.6). For a given C-rate, there is little change in capacity as the applied pressure is increased, highlighting the cell strain response is more sensitive to the C-rate than the applied pressure in the range of 0 – 500 MPa. This is in line with previous

findings (Figure 4.3b) which showed the driver of localised strains within the Si is the higher C-rate (5C versus 1C).

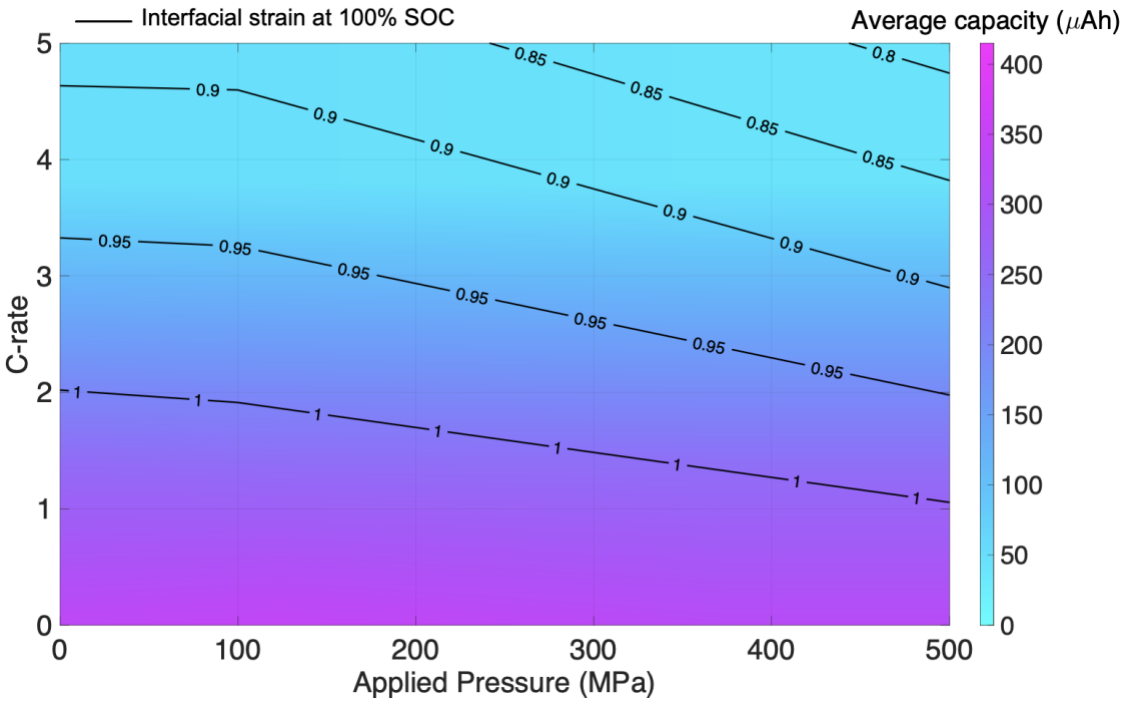

Figure 4.6 Contour map of maximum principal strain at 100% SOC (solid black lines) at the Si|LiPON interface as a function of C-rate versus applied pressure, with corresponding-coloured contours of average cell capacity.

The stress at 100% SOC (black contours in Figure 4.7a) is significant in that as the applied pressure increased the compressive stress also increased, but the stress was independent of C-rate. Again, the average cell capacity is largely dependent on C-rate and minimally affected by applied pressure. At higher C-rates the cell capacity was reduced due to slow Li ion diffusion in Si, which produced non-linear concentration gradients within the electrode and reduced the degree of lithiation. The stress experienced at the interface remains compressive for all non-zero applied pressures. By contrast, the stress at 0% SOC (Figure 4.7b) depends both on C-rate and applied pressure. The stress and strain experienced at the interface are due to the tensile lithiation-induced stress during discharge. As the C-rate was increased, the tensile stress also increased and the build-up of stress under these conditions could be of concern for void formation as well as possible Si and/or SE fracture. It

is interesting to note at a given C-rate, as the applied pressure increases, the stress is reduced due to the applied pressure which exerts a compressive force (clearly visualised in Figure 4.4b) resulting in an overall reduced tensile stress. The capacity is influenced by the C-rate, reducing at higher C-rates, with little dependence on applied pressure.

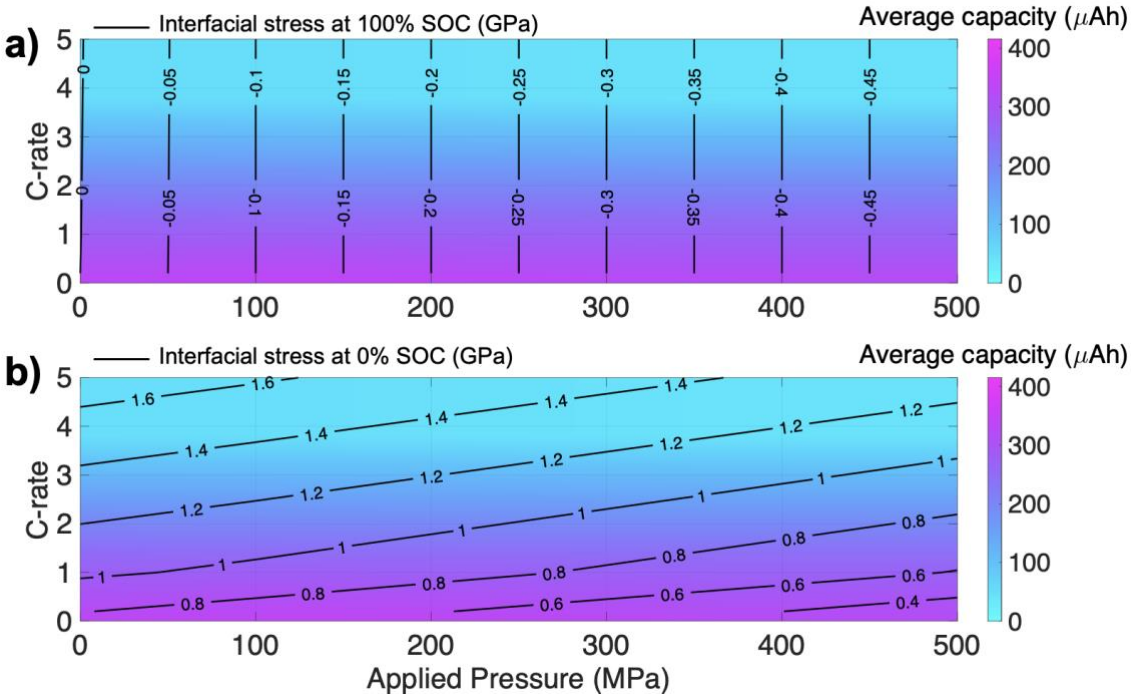

Figure 4.7 Contour map of maximum principal stress in GPa (solid black lines) at the Si|LiPON interface as a function of C-rate versus applied pressure with corresponding-coloured contours of average cell capacity at **a)** 100% SOC and **b)** 0% SOC.

4.3.3 Materials selection

To explore the mechanical properties of the SE and its influence on the resulting stress and strain, the SSB was extended from the baseline case (LiPON SE) to include other SEs. Two commonly used SEs were chosen, both of which display different electrochemical and mechanical properties (outlined in Table 4.1). In all cases, the SSB was fully constrained to probe the effect of SE plastic deformation.

The Si stress at 1C, 0% SOC was non-linear for all SEs (Figure 4.8a) however, compared to LiPON the Si stress increased for the LLZTO case but reduced for the LPSCl case. At 5C, the spread in Si stress reduced for the three different materials (Figure 4.8b) highlighting the importance of kinetics on the Si stress response. The stress at 5C was observed to change from compressive (at the CC) to tensile at the Si|SE boundary. In contrast, at 1C the stress remained compressive through the Si, though it reduced in value towards the Si|SE interface. The reason behind the tensile behaviour at 5C can be understood by analysing the different concentration gradients within the Si NE for the LPSCl case at 1C (Figure 4.8c) versus 5C (Figure 4.8d). The Li concentration in Si at 5C is highly non-linear exhibiting a turning point in the concentration gradient due to the slow diffusion of Li in Si, at a normalised distance from the CC (≈0.9) and a subsequent drop in concentration. This rapid reduction in concentration likely reduced the stress at the interface and since the top of the cell is constrained, a mix of compressive stress and tensile stress exists within the Si. By comparison, the concentration gradient in the Si at 1C (Figure 4.8c) show a gradual decay in concentration. Only the Si concentration gradient for the LPSCl case is modelled here for clarity as the profiles follow a similar trend for the other two SEs.

The Si strain at 100% SOC (Figure 4.8e) was highest for the LPSCl case, which was expected as it exhibited the lowest stress and therefore highest Si lithiation. Although LPSCl exhibited the highest strains (Figure 4.9c) which could be undesirable from an engineering standpoint, it also had the highest amount of lithiation, which will result in the greatest cell capacity. The spread in strains was larger for 1C versus 5C for the different SE materials (Figures 4.8e and 4.8f) and the stress-strain profiles were more homogenous throughout the Si electrode for 1C.

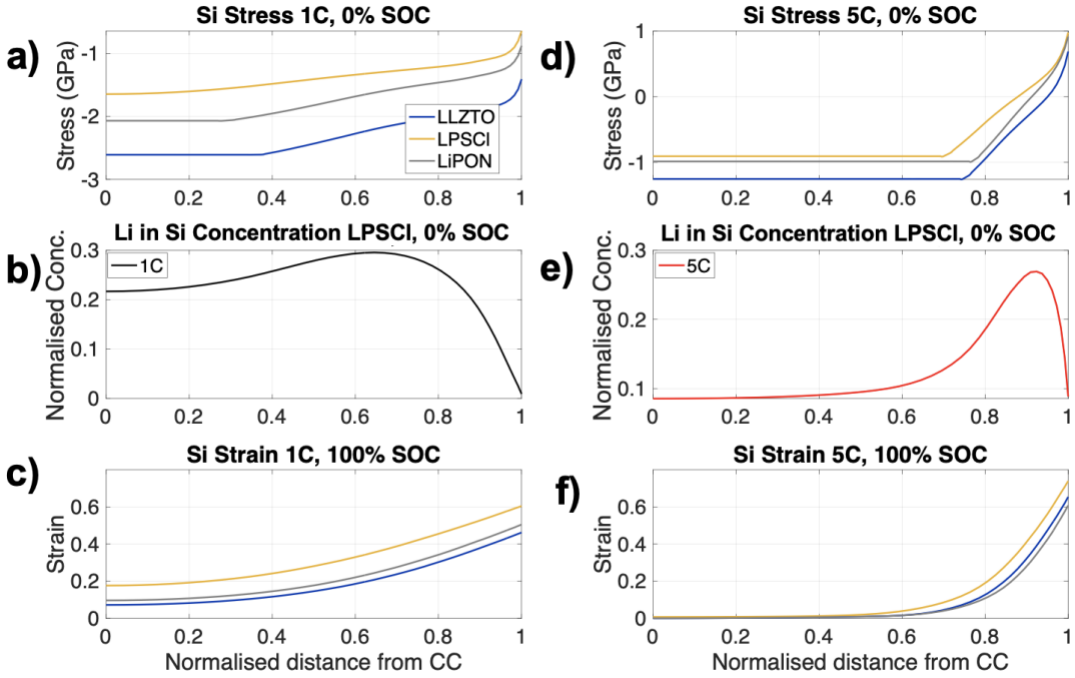

Figure 4.8 Si stress at 0% SOC at **a)** 1C and **b)** 5C for the three different SEs: LPSCl (yellow), LiPON (grey) and LLZTO (blue). The Si concentration for the LPSCl case at 0% SOC at **c)** 1C (black) and **d)** 5C (red). The Si strain at 100% SOC is displayed for **e)** 1C and **f)** 5C. Legend in **a)** applies to Figures **a), c), d)** and **f)** whilst **b)** and **e)** have their own legends.

At 100% SOC, the Si stress and SE stress and strains at different C-rates (C/5, 1C and 5C) were constant throughout the domains, therefore a scatter plot was chosen to best represent the results (Figure 4.9). The Si stress (Figure 4.9a) was greatest for the LLZTO case but the stress (Figure 4.9b) and strain (Figure 4.9c) within LLZTO were significantly lower compared to LiPON and LPSCl. LLZTO did not yield under any C-rate and as a result displayed lower stress and strain. LPSCl has the lowest yield strength which resulted in the early onset of plastic deformation, the Si stress was reduced. This resulted in increased lithiation which means it experienced the highest SE stress and strain for all C-rates. This could be concerning for low yield strength materials such as LPSCl which deformed by as much as 15% even at the low C-rate condition of C/5. As previously observed, as

the C-rate increased the spread in stress-strain values between the three materials decreased.

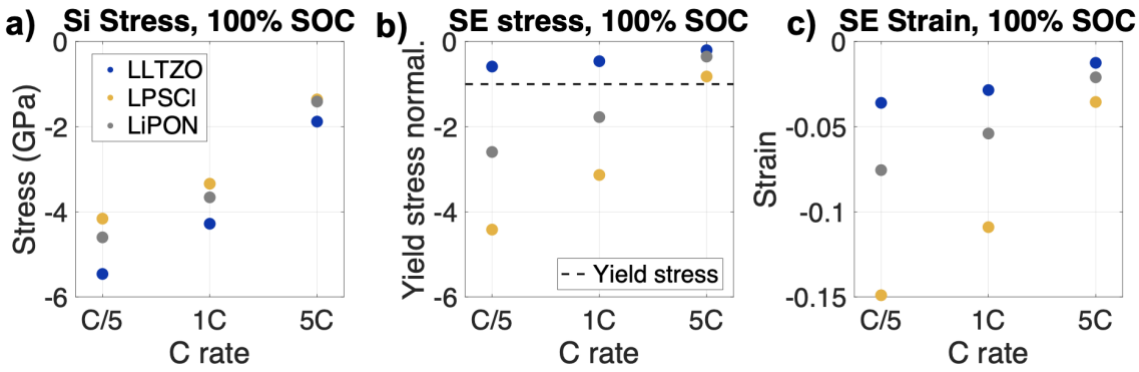

Figure 4.9 a) Si stress at 100% SOC for the three different SEs: LPSCl (yellow), LiPON (grey) and LLZTO (blue) at C/5, 1C and 5C. **b)** The SE stress normalised by its yield stress (dashed line) and **c)** SE strain at 100% SOC. The legend in **a)** applies to all figures.

4.3.4 Solid electrolyte design for optimal cell performance

This section considers the SE mechanical properties for optimal cell performance under the fully constrained case at 1C, 100% SOC. Following the discussion on the importance of the SE mechanical properties on the stress-strain response, six cases of hypothetical SEs were simulated with Young's moduli and yield strength values taken alternatively from LiPON, LLZTO and LPSCl (Figure 4.10). Such materials could be realised via composites or SE material discovery. For comparison, LiPON, LLZTO and LPSCl are displayed alongside the different SE cases, with the LiPON SE (grey dashed line) and Si (red dashed line) stress values displayed for reference.

In Case 1, the Young's modulus of LiPON was chosen and paired with a lower yield strength equal to LPSCl. This resulted in a reduction in Si stress compared with LiPON, due to the earlier onset of the SE yielding and subsequently increased the SE stress. Case 2 simulates the Young's modulus of LLZTO with a moderate yield strength equal to that of LiPON. Compared to pure LiPON, a minimal increase in the SE and Si stress occurred. In Case 3, the SE stress increased significantly

(≈1.1 GPa) due to the lower yield strength, whilst Si stress reduced minimally (≈0.1 GPa). Case 4 simulated the Young's modulus of LiPON with relatively higher yield strength equal to that of LLZTO. The SE stress reduced significantly (≈-1 GPa) as the material yield onset was delayed which increased the Si stress (≈0.35 GPa). For Cases 5 and 6, LPSCl Young's modulus was chosen with a yield strength equal to LLZTO and LiPON respectively. There was little change between the two cases, though Case 6 has a slightly lower yield strength, which increased the SE stress and reduced the Si stress minimally. Compared to the LPSCl SE, Cases 5 and 6 show an increased Si stress (≈0.2 GPa) but with a greater reduction in SE stress (≈0.6 GPa) due to the higher yield strength.

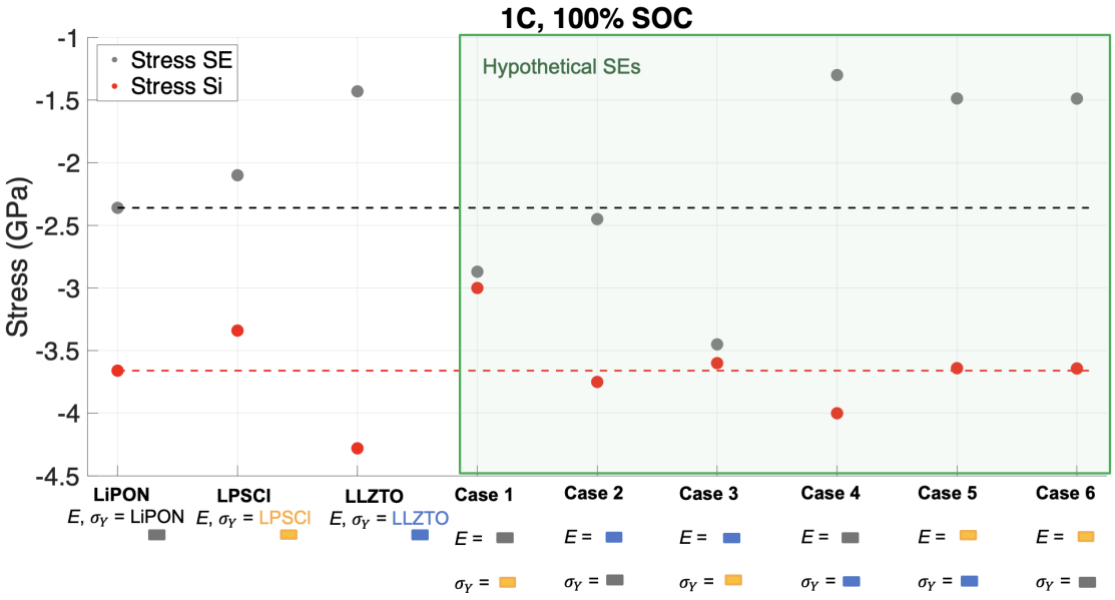

Figure 4.10 Si (grey dots) and SE (red dots) stress response at 1C, 100% SOC. LiPON, LPSCl and LLZTO SEs are contrasted against six simulated hypothetical SEs with Young's modulus and yield strength values taken alternatively from LiPON, LPSCl and LLZTO which are represented by coloured rectangle symbols (grey for LiPON, yellow for LPSCl and blue for LLZTO). The dashed line across the y-axis highlights the LiPON SE and Si stress values from the baseline study.

Overall, a trend was observed whereby choosing a relatively moderate Young's modulus, similar to that of LiPON, helps to reduce the Si stress and pairing with a low yield strength allows for the early onset of SE yielding which further reduces Si stress (Case 1) but results in an increase of SE stress. Selecting a relatively low Young's modulus material such as LPSCl with a high or moderate yield strength (Case 5 or 6) reduces the SE stress similar to Case 4. However, in comparison to Case 4, the Si stress is reduced further by ≈0.4 GPa. If reducing the stress in the Si NE is of primary concern, then a SE with a moderate Young's modulus and low yield strength (Case 1) should be chosen. If, however, a reduction in SE is of greater importance, then as Cases 5 or 6 show, a low Young's modulus and a high or moderate yield strength should be adopted. Selecting a high Young's modulus similar to LLZTO did not provide much benefit against the baseline LiPON case in either Si or SE stress. If a high Young's modulus material is to be used then its advantage is in its superior yield strength which reduces the SE stress, although a greater reduction in both SE and Si stress can be achieved with a moderate Young's modulus similar to that of LiPON tailored with the high yield strength of LLZTO. Therefore, a high Young's modulus alone is not advantageous in reducing the Si and SE stress – the yield strength also plays an important role.

4.4 Conclusion

A previously validated echem-mech model of a thin film SSB with a Si NE[33] (Chapter 3) was used to understand the effect of mechanical and electrochemical properties on the first and second charge-discharge cycles. Then, the effect of applied pressure and C-rate on the average cell capacity and stress-strain response was probed. Finally, the mechanical properties of the SE were tailored for minimal interfacial stress and strain. Key insights include:

(1) Modelling Si plasticity and the diffusion of Li^+ ions in Si greatly influences the achievable first cycle capacity. Focus should be drawn to

the mechanical and electrochemical parameters of Si when optimising SSB cycle life.

(2) The interfacial stress at 100% SOC was found to be C-rate independent and increased as a function of applied pressure. Thus, to reduce the interfacial stress and strains at 100% SOC and increase cell capacity, low to moderate C-rates (1-1.5C) and applied pressure are desirable (< 200 MPa).

(3) The stress experienced at the end of discharge was tensile which is of concern as it could lead to void formation during discharge. To reduce the interfacial stress at the end of discharge and increase cell capacity, low C-rates (<1C) and moderately applied pressure (100-200 MPa) are desirable, as the applied pressure reduces the overall tensile stress.

(4) The capacity was strongly influenced by the C-rate and minimally affected by applied pressure. As the C-rate increased the average capacity reduced greatly (factor of ≈5 from 1C to 5C, with no applied pressure). This emphasises that the slow Li ion diffusion in Si is a key driver of the localised concentration gradients and limits the achievable cell capacity. Strategies to mitigate this aspect include use of a thinner Si electrode with added porosity[14] or nano-structuring of Si to increase its surface area.[129]

(5) Finally, to optimise the SE material mechanical properties to reduce the stress experienced in Si and SE (at 1C, 100% SOC), several hypothetical SEs cases were simulated, and the following material design choices were proposed:

    a. If reducing maximum Si stress is of primary concern, then a moderate Young's modulus similar to LiPON (≈77 GPa) with a low yield strength comparable to sulfide materials such as LPSCl (≈0.67 GPa) should be selected.

    b. However, if a reduction in SE stress is of greater importance, then a low Young's modulus similar to LPSCl (≈29 GPa) with a moderate to high yield strength (1.3-3 GPa) should be adopted.

(6) Post-yield mechanical properties of different SEs should be experimentally reported as these will greatly influence the stress-strain response of the cell. A perfectly plastic post-yield behaviour for the SEs was assumed in this study due to a lack of experimental values in the literature.

In summary, there has been a relative lack of emphasis on high-capacity Si NEs for SSBs and the results in this work showcase a variety of factors such as C-rate, applied pressure and Si and SE mechanical properties that can affect the cell capacity and stress and strain evolution. The SE Young's modulus, yield strength and fracture properties likely play a role in the SSB cycle life and future work will look at probing these aspects. Other factors such as reducing the Li ion diffusion path in Si, will need to be considered. This work set out to try to understand the mechanical cell response and the influence of SE material properties. By tailoring the SE material, it has provided an insight on the importance of SE material selection, design and characterisation of the elastic-plastic behaviour which are relevant for large format SSB systems. Echem-mech interactions need to be carefully controlled and considered to enable high performance next-generation SSBs.

Chapter 5

Scalable Solution-Processed Non-Crystalline Solid Electrolytes

This chapter is adapted from the work published in "Vadhva, P.; Gill, T. E.; Cruddos, J. H.; Said, S.; Siniscalchi, M.; Narayanan, S.; Pasta, M.; Miller, T. S.; Rettie, A. J. E. Engineering Solution-Processed Non-Crystalline Solid Electrolytes for Li Metal Batteries. *Chemistry of Materials* **2023**. https://doi.org/10.1021/ACS.CHEMMATER.2C03071."

Contribution Statement: Experimental characterisation and analysis was carried out by P. Vadhva with help from S. Said on AFM testing and S. Narayanan on in-situ XPS. In addition, Li deposition training and testing was carried out by M. Siniscalchi, in conjunction with P. Vadhva. Assistance in film synthesis and electrochemical testing on the phase space of LAPO, was supported by T. Gill and J. Cruddos. Funding acquisition and project supervision by A. Rettie, M. Pasta and T. Miller.

5.1 Introduction

Moving beyond LiPON, to other NC materials that can be engineered using scalable methods is vital when considering manufacturing of SEs to reduce cost and increase throughput. New NC SEs produced by scalable methods would be of great interest for advanced batteries such as thin film SSBs or "anode-free" cells with the films deposited onto the NE CC.[130] Solution-based processing involving direct deposition of precursor solutions followed by a moderate temperature annealing step can function as a low energy alternative to the conventional high temperature routes used for ceramic SEs.[131,132] From the work carried out in Chapters 3 and 4, it is understood that the SE mechanical properties greatly influence the cell performance. A moderate Young's modulus ≈77 GPa (similar to that of LiPON) should be targeted for such a NC material. The ductile nature of a NC material is beneficial in terms of reducing the stress within a SSB as seen in this study. From an electrochemical standpoint, a similar ionic conductivity of LiPON in a thin film format is desirable to allow for fast reactions at the interface and through the SE. If a sub-micron thickness NC material can be engineered, Li^+ ions travel a shorter distance compared to bulk crystalline SE materials (10s-100s of microns thick) and a slightly lower ionic conductivity (10^{-7}-10^{-6} S cm^{-1}) compared to these bulk crystalline SEs can be justified. This chapter will discuss such a scalable NC material that exhibits the highest ionic conductivity of a lithium aluminophosphate material (>10^{-7} S cm^{-1}) with a Young's modulus (54(4) GPa) similar to that of LiPON.

Here, NC LAPO phases are reported with desirable SE properties synthesised from solution. First, this phase space is rationally explored and thin film materials with σ_{ion} >10^{-7} S cm^{-1} found. Then, the effects of annealing temperature on the σ_{ion}, film structure, surface roughness, chemical composition and local structure are studied. The optimised SE is shown to exhibit a small barrier to Li^+-ion transport, low σ_e, and mechanical properties comparable to LiPON. Finally, the electrochemical stability against Li-metal is probed and the chemical composition of the resultant interphase determined.

5.2 Experimental Methods

5.2.1 Film fabrication

Li-Al-P-O thin films were synthesised by spin coating from aqueous precursor solutions, followed by an annealing step in air as described previously.[133] In a typical spin coating synthesis, 50 mmol of $Al(NO_3)_3 \bullet 9H_2O$ (Sigma Aldrich) was added to 50 mL of de-ionised (DI) water and stirred for 1 hr until completely dissolved. To this solution, 63 mmol of H_3PO_4 (85% concentrated in water) was added and stirred overnight at 80 °C. After cooling to room temperature, 137.5 mmol of $LiNO_3$ (Fisher Scientific) was added. Finally, the solution was diluted with DI water to achieve a final concentration of 0.4 M with respect to Al. This final concentration was used for all precursor solutions with the moles of $LiNO_3$ or H_3PO_4 being varied to achieve a range of Li:Al:P ratios during compositional exploration.

Si substrates (p-type, boron-doped, single-side polished, resistivity <0.1 cm, PI-KEM), were used as electrically conductive back contacts with low roughness. These were cut into 2×2 cm^2 squares using a diamond scribe and sonicated separately in acetone and then IPA for 5 min, rinsing with DI water in between. Subsequently, the substrates were dried using a N_2 gun before being O_2 plasma-treated (Henniker HPT-100) at 100 W for 5 min to produce a hydrophilic surface.

The precursor solution was sonicated at 40 °C for 1 h and cooled to room temperature before being twice filtered using a 0.2 μm Teflon filter attached to a syringe. The solution was flooded onto the substrate, spin coated at 3000 rpm for 30 s (after a ramp rate of 6000 rpm s^{-1}) and immediately transferred to a pre-heated hot plate at 275 °C for 1 min. The process was repeated for multi-layer films, by allowing the film to cool to room temperature before spin coating the next layer. After the designated number of layers were deposited, a final anneal at the desired temperature was carried out for 1 h. For the films annealed above 275 °C, a box furnace was used with a 5 °C min^{-1} ramp rate. For the films annealed at 230 °C, the pre-heated hot plate was set at 230 °C so that the films were not exposed to a temperature above this value.

5.2.2 Physical characterisation

Film thickness was determined using a LEO Gemini 1525 field emission scanning electron microscope (SEM). SEM uses an electron microscope which focusses an electron beam, onto a substrate causing it to scatter electrons (primary electrons) and produce secondary electrons which are detected and used to construct a magnified 3-D image of the sample. The electrons interact with the atoms in the sample thereby containing information about the surface topography. The electron beam in a typical SEM is generated through a thermionic emission gun or PE ray tube where resistance heating in the filaments cause emission of electrons by thermionic emission when the filament has a high enough current passed through it.[134] If a minimum emission voltage of 200 kV is required, and the electrons are accelerated towards the NE thereby gaining 200 keV of energy. The electrons are then collimated by condenser lenses into thin beam and the *x,y* scanning coils are used to raster the beam (in the *x* and *y* directions) with the objective lens to converge the beam to focus it on the sample. The X-ray detector emits X-rays which is useful for Energy Dispersive Spectroscopy (EDX analysis). EDX is commonly used in conjunction with SEM, to detect characteristic X-ray energies to qualitatively study the elemental composition of the sample.

SEM detects electrons from two types of sources: secondary and back-scattered electrons. Secondary electrons are primary electrons (from the beam) that have interacted with the surface of the sample through inelastic collisions. The incident electron excites an electron in the sample, losing some of its energy. The excited electron now moves to the surface of the sample where it may excite the surface, if it has sufficient energy to do so and becomes the secondary electron. When the primary electron beam excites an inner shell of an atom to a higher energy state, an outer shell electron becomes attracted to the inner shell (due to the positive hole left by the excited electron). There is a shift of energy as this electron moves from a higher energy level to a lower one, meaning that the excess energy is released in the form of an X-ray. In addition to these X-rays, photons and auger electrons are

also emitted due to the electron interaction with the sample. Backscattered electrons are primary electrons that have undergone elastic collision with the sample, being scattered from their original path, and have been reflected back with no loss of energy (Figure 5.1).[135]

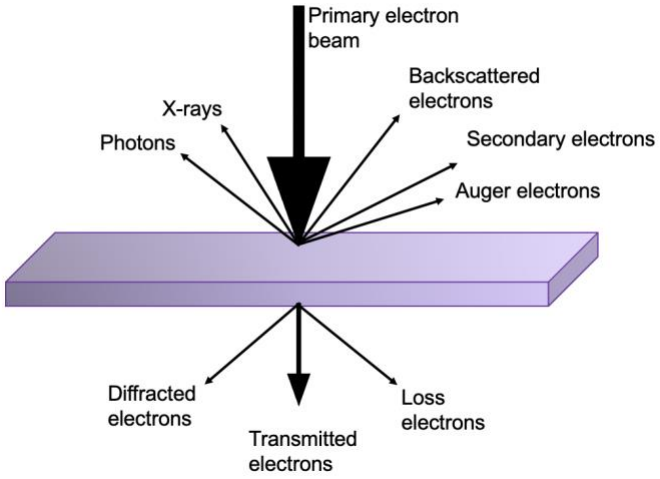

Figure 5.1 Possible processes when a sample is illuminated with electrons.

A vacuum is used to house the sample instruments and sample preparation is key, whereby samples with low electronic conductivity should be sputtered with a conductive metal to minimise charging. Very light elements (H, He or Li) are hard to detect using EDX due to the poor resolution and low signal from these small atoms which are not able to scatter enough electrons to produce a detectable signal. Therefore, for compositional analysis on LAPO films which contain Li, XPS was conducted. For LAPO films SEM cross-sectional imaging, the brittle-fracture method was used, and a thin Au layer was sputtered to minimise charging. Multi-layer films were used for ease of imaging.

The film morphology and mechanical properties were characterised using atomic force microscopy (AFM, Bruker Dimension Icon with ScanAsyst). AFM microscopy is a surface sensing technique which uses a sharp nanoscale tip on a silicon probe. As the tip contacts the sample surface, the cantilever to which it is attached to bends. The bending of the cantilever is indicative of the tip and sample

interaction force and is detected using a laser diode and a split photodetector. The tip is used to generate an image of the sample through raster scanning across the surface. Two main operating modes are commonly used: contact and tapping mode. When the probe is in contact mode, the tip presses into the surface which causes an electronic feedback loop monitoring the tip and sample interaction force. However, when the probe is in tapping mode, it limits the amount of contact between the surface of the sample and the tip to prevent both the surface and tip from damage. For this reason, tapping mode is commonly adopted. The cantilever, which forms as a spring, vibrates near its resonance frequency, moving the tip sinusoidally up and down. The sinusoidal motion of the tip is altered as a it moves towards the sample. Again, a feedback loop is used, similar to the contact mode, to keep the amplitude of the tapping motion constant. In both modes, the topography of the sample is traced.

AFM was conducted across a 10×10 μm^2 LAPO film area, with the average roughness calculated from three different areas across 1×1 μm^2 using the PeakForce Quantitative Nanoscale Mechanical mode which uses utilises the tapping mode to probe the nanomechanical properties of the film. For mechanical property measurements, the probe was calibrated by the relative method, using highly oriented pyrolytic graphite (HOPG) with a nominal elastic modulus of 18 GPa for reference. At each point in the scan, alongside the morphology, the probe performed nanoindentation measurements and recorded the load and displacement of the specialised tips and cantilevers to produce a load–displacement curve. The DMT (Derjagin, Muller, Toropov) model[136] was used to fit the force displacement curve as this model is commonly applied to tips with a small curvature radius and high stiffness. The reduced Young's modulus, E_r can be obtained via:

$$F - F_{adh} = \frac{4}{3} E_r \sqrt{R(d - d_0)^3} \qquad (5.1)$$

where $F - F_{adh}$ is the force on the cantilever relative to the adhesion force, $(d - d_0)$ is the sample deformation and R is the radius of the tip end. From the reduced modulus the sample's elastic modulus can be obtained, where E_i and v_i are the moduli and Poisson's ratio of the indenter and sample (E_s, v_s) respectively.

$$E_r = \frac{1 - v_i^2}{E_i} + \frac{1 - v_s^2}{E_s} \tag{5.2}$$

The E_i and v_i of the diamond indenter was taken to be 1070 GPa and 0.07 respectively. The Poisson's ratio of the sample, v_s was assumed as 0.3 which is common for these SE materials (Table 1.1). All of the results obtained by the AFM were analysed by Nanoscope Analysis software.

5.2.3 Chemical characterisation

The film composition was determined using X-ray photoelectron spectroscopy (ThermoFisher, K-alpha XPS system, Al source) with binding energies referenced against the adventitious carbon 1s peak at 284.4 eV. XPS is a surface sensitive technique with an average depth analysis of ≈5 to 10 nm.[137] Information about the chemical and electronic state at the surface of a material, elemental composition and empirical formula can be analysed. The energies of the photoelectrons which have been excited by the incident high energy electrons are studied. From the intensity of the photoelectron peak and binding energy, the identity of the material can be determined. XPS necessitates operation in a high vacuum ($<10^{-8}$ Torr)[138] to reduce the number of inelastic collisions and contamination with atmospheric gas atoms.

Electrons are fired at an NE, usually Al or Mg,[138] which then passes through a monochromator to make sure all the photons have the same wavelength and therefore energy. For Al X-rays this gives a K-alpha of 1486.7 eV.[138] If the energy of the incident X-rays on the sample has an energy exceeding the binding energy,

an electron from a valence band will be emitted. The binding energy of the emitted electron can be calculated using the photoelectric equation:

$$E_{binding} = E_{photon} - (E_{kinetic} + \varphi). \quad (5.3)$$

Since the kinetic energy of the incident photon is known, E_{photon} and the kinetic energy, $E_{kinetic}$ of the emitted electron is measured by the photoelectron detector and the work function, φ, is specific to the surface material, then the binding energy, $E_{binding}$ can be calculated.

The probability of detection, $P(d)$ at a distance d into the sample decreases as d increases. The inelastic mean free path of the electrons λ, is the distance the electron can travel through a solid and interacting with matter, before losing energy.[138]

$$P(d) = exp\left(-\frac{d}{\lambda}\right) \quad (5.4)$$

The probability of detection decreases exponentially as the distance into the film increases. A typical XPS spectra will have peaks at the different binding energies from the emitted photoelectrons. The intensity of the XPS peaks (height), will be proportional to the number of photoelectrons emitted at that binding energy, corresponding to the electron configuration within the atoms; 1s, 2s, 2p etc. To calculate the composition of the material, the raw XPS signal is fitted (Shirley background used) and the extracted area is divided by the relative sensitivity factor (RSF), and then normalised by each element identified by the analyser in order to calculate atomic percentage of each element in the compound.

Any changes in the XPS spectra or slight shifts in energy of the binding energy of the compound can indicate slight oxidation or reduction of that particular element. For example, an oxidised element will shift to higher binding energies as changes in valence electron density alters the shielding effect of the inner electrons. It should be noted that hydrogen and helium are not detected using XPS due to the small photoelectron cross section of helium, and hydrogen which are lacking in

core electrons. Quantitive accuracy of XPS depends on factors such as the signal-to-noise ratio, peak convolution, RSFs accuracy and correction of the electron energy due to the electron inelastic mean free path.[139]

For the LAPO samples. a survey scan and regions around elements of interest were conducted. The following RSFs from CasaXPS were used to quantify film surface stoichiometries, Li 1s (0.057), Al 2p (0.537), O 1s (2.93) and P 2p (1.192). For lighter elements such as Li, a minimum of 30 scans were acquired. In situ XPS coupled with Li deposition was conducted in an in-house set-up, using a Phi XPS VersaProbe III with an Al Kα X-ray source generating focused, monochromatic Al Kα X-rays at 1486.6 eV under ultrahigh vacuum conditions (the main chamber maintained at pressures between 10^{-7} and 10^{-6} Pa). Here, Li metal ($3\times3mm^2$, 750 nm thick, Sigma Aldrich) was attached to a sample holder within the XPS chamber, similar to the setup described by Wenzel et al. previously.[140] The LAPO sample and Li metal were transferred to the XPS chamber using a vacuum transfer vessel directly from a glovebox to minimise air exposure. Li sputtering was conducted using an Ar^+ ion gun, at an acceleration voltage of 4 kV and beam current of 2.8 μA with data were collected at intervals of 5 mins. CasaXPS software was used to analyse the XPS data and quantify the chemical composition using Shirley background fitting. The spectra obtained prior to lithium deposition were charge corrected to adventitious C at 284.8 eV through acquired C 1s spectra. After lithium deposition the Li_2O peak at 528.5 eV in the O 1s spectra was used for charge-correction.

Grazing incidence X-ray diffraction (GI-XRD) was performed on a Bruker D8 Discover diffractometer with a microfocus Cu source and Vantec 500 2D detector. X-ray diffraction is a non-destructive technique used to infer the crystalline characteristics of a material. Bragg's law has been used to explain the X-ray interference pattern as a result of X-rays being scattered by the lattice plane of a crystal. Using Bragg's equation[141] the average spacing between the lattice planes inside the crystal can be calculated. Constructive interference occurs at *d*, i.e. the X-rays interfering from crystal planes with spacing *d*,

$$n\lambda = 2d \sin(\theta) \qquad (5.5)$$

where, λ is the wavelength of the X-rays, n is an integer and θ is the incident X-ray angle which is equal to half the angle the X-rays are scattered through. The unit-cell of a crystalline material has atomic planes with different spacing depending on the structure of the crystal. These produce a characteristic pattern for a given crystalline material. Therefore, the degree of crystallinity in a material can be inferred from XRD as well as identifying the amount of different crystalline phases by comparing the data to reference databases and if there is any amorphous material present. Amorphous components may appear as a broad, ill-defined background signal, unlike the sharp peaks observed for a crystalline structure.

In the X-ray source, X-ray beams are emitted by the target, through thermionic emission, which are accelerated in an electric field towards a metal anode target. In laboratory sources, Cu and Mo are commonly used. The accelerated electrons fired at the metal cause an electron in an inner shell to be emitted which then cause an electron from a higher valence band to drop to a lower band, with the emission of an X-ray photon with an energy equivalent to the difference between energy bands.

The X-ray beam is collimated and focused on the sample. The X-ray detector moves around the sample and the intensity of the scattered X-rays (counts per second) are measured as function of angle 2θ. It is typical to use filters to block the K-beta extra peaks, so that only K-alpha will be observed on the spectra. The K-alpha line is defined as the two orbitals involved in the electron transition from a higher to lower valence band which are adjacent to one another. If the two orbitals are separated by a shell, then this transition is known as K-beta line.[142]

GI-XRD is a modification of the XRD method that uses small incident angle X-ray beams to limit X-ray penetration into the bulk material thereby optimising the signal intensity from the surface of the sample. This technique is therefore well suited to thin films and was used to study the LAPO films. The films were spin coated onto fused silica substrates to minimise scattering from the substrate. The fused silica substrates were cleaned using the same procedure as the Si wafers and

were purchased pre-cut to 2×2 cm^2, with a thickness of 1 mm from Multi-lab. The scans were performed in a theta-theta geometry with 4 frames at 120 s per frame and the sample was rotated in the beam during collection.

5.2.4 Electronic and electrochemical characterisation

Through-plane measurements were performed throughout. Circular Au top contact pads (1.2 mm diameter, ≈80 nm thickness) were deposited by sputtering through a shadow mask. For the bottom contact, Al foil was attached to the back of the Si substrate using conductive epoxy (Agar Scientific). An in-house cell holder was designed to take conductivity measurements, where an Au-plated screw with a rounded tip gently contacted the Au pads. In all cases 4-layer films were used as thinner films could be damaged by the screw contact pressure. The Au screw and Al back contact were connected to a potentiostat (Reference 600+, Gamry) for electrochemical measurements, with no applied pressure other than that of the Au screw lightly contacting the film. This error on the amount of screw pressure applied to the film, will be a combination of the variation in 1) the measurement procedure and 2) the film properties. If it is assumed that the errors due to the measurement procedure (i.e., contacting the top contact pad with the screw) will be constant over many films of different compositions (reasonable because number of measurements is large), then an upper bound can be estimated from the lowest relative error (evident in Figures 5.4 and 5.5): ≈16%. Therefore, the role of contacting the contact pad and any associated pressure is not significant in this case, which is reasonable as the sputtered top contact pads define the area of the cell (1.13 mm^2) and are significantly larger than the rounded screw tip (0.20 mm^2 maximum), so the majority of the cell is under no applied pressure.

EIS was conducted using a 5 mV perturbation voltage over a frequency range of 50 Hz to 1 MHz conducted at room temperature. The EIS data were fit using an equivalent circuit model (ECM) consisting of elementary components in a Randles type circuit.[143,144] A resistor (R) and constant phase element (CPE) in parallel were used to model different relaxation processes, where R_0 accounts for the impedance due to the ohmic resistance from electrical contacts, R_1 is assigned to the bulk SE

impedance (R_b) of LAPO and CPE_w accounted for the electrode polarization due to the non-symmetric blocking electrodes.[117]

The ionic conductivity, σ_{ion} was calculated using Equation 5.6:

$$\sigma_{ion} = \frac{l}{RA} \tag{5.6}$$

where, l is the thickness of the film, R is the bulk SE resistance and A is the geometric area. These values were averaged from 3 different films, with each film being sampled 6 times across the sample.

Temperature-dependent EIS measurements were conducted inside a thermal chamber in air on 3 separate samples to obtain an average. Data collection was performed during heating and a wait time of 2 h was used at each temperature point to reach thermal equilibrium. The temperature dependence of the σ_{ion} was fit to an Arrhenius relationship:[145,146]

$$\sigma_{ion}\mathrm{T} = \sigma_0 \, e^{-E_a/kT} \tag{5.7}$$

where, σ_0 is a pre-exponential factor dependent on temperature T, E_a is the activation energy and k is the Boltzmann constant.

For the DC polarisation experiments, a voltage bias of 1 V was applied for 1 h and the current-voltage curve fit to an exponential decay function. A longer duration constant-voltage experiment was run over 12 h, which confirmed that 1 h was sufficient to reach steady state.

Finally, the electrochemical stability of LAPO with Li metal was probed by thermally evaporating Li (MBraun, EVAP) to form circular contacts (1 mm diameter, 1 μm thickness) onto a LAPO film on a Si substrate, resulting in a Li|LAPO|Si configuration, which had been dried under vacuum in a Buchi oven at 60 °C overnight. The idea that the drying process did not significantly affect the films was investigated: a room temperature $\boldsymbol{\sigma_{ion}}$value of 1.5(7)×10^{-7} S cm^{-1} was measured for dried $Li_{2.8}AlP_{1.25}O_x$ films vs. 1.8(5)×10^{-7} S cm^{-1} with no drying step.

Cu was used as the current collector and the cell was sealed under Ar in a pouch cell bag (Figure A.3 in the Appendix shows an image of the LAPO film on a Si wafer inserted inside the pouch cell before sealing). The cell was clamped between two plates to ensure good electrical connection. EIS was conducted at room temperature over 13 h with a Biologic MTZ-35 potentiostat, between 1 Hz and 3.7 MHz. To separate polarisation contributions from the various cell components and identify all time processes in the system, a Fourier transform of the EIS data was performed for DRT analysis by,[23,147]

$$Z(w) = R_{\text{ohmic}} + Z_{pol}(w) = R_{\text{ohmic}} + \sum_{i=1}^{N} \frac{R_{\text{pol,k}}}{1 + j\omega\tau_k} \qquad (5.8)$$

where, R_{ohmic} is the Ohmic resistance of the SSB and is independent of frequency, while $Z_{pol}(w)$ accounts for the polarisation resistance, $R_{pol,k}$ and is a function of frequency. This deconvolution is possible since the different cell processes have characteristic frequencies, and therefore time constants, associated with specific processes. A MATLAB code by Wan et al.[147] was used to perform DRT analysis. The Li deposition and cell assembly were carried out in an Ar-filled glovebox (MBraun, <1 ppm H_2O and O_2).

5.3 Results and Discussion

5.3.1 Compositional engineering

LAPO films were synthesised by spin coating and produced visually homogenous films by eye. The amount of the lithium nitrate salt in the precursor solution was varied to target different LAPO compositions. The experimental apparatus for the precursor solution synthesis and the synthesised LAPO film (after spin coating and annealing) is shown in Figure 5.2.

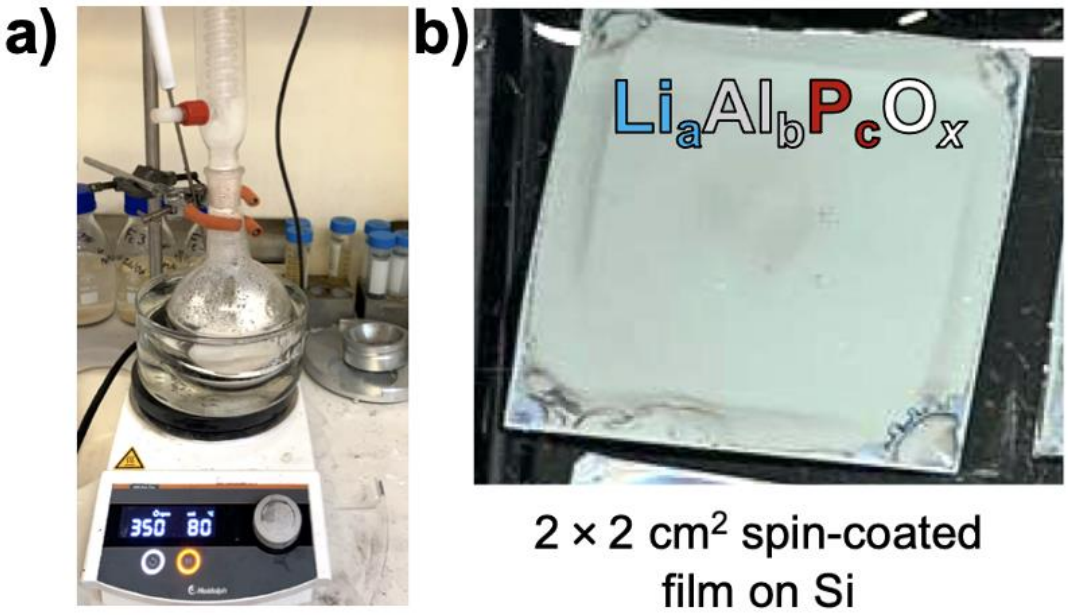

Figure 5.2 a) Experimental apparatus for the precursor solution synthesis which is used for spin coating and subsequently annealed on a silicon substrate (for electrical measurements) at temperatures > 230 ºC depending on the targeted annealing temperature of the sample. **b)** Visual representation of a sample annealed at 275 ºC is shown.

Previous work[133] determined a room temperature σ_{ion} (value of 2.6×10^{-8} S cm^{-1} for the single composition $Li_{2.5}Al_1P_{1.5}O_{5.5}$ (based on the bulk glass $0.5Li_2O$-$0.2Al_2O_3$- $0.3P_2O_5$)[148] annealed at 275 °C. Because elemental composition can strongly affect the conduction properties of SEs,[148,149] the Li and P ratios relative to Al in $Li_aAl_1P_cO_x$ was systematically adjusted whilst keeping the annealing temperature constant at 275 °C. Note that *a* values were determined by XPS, while *c* represents the nominal amount of phosphorous in the precursor solutions.

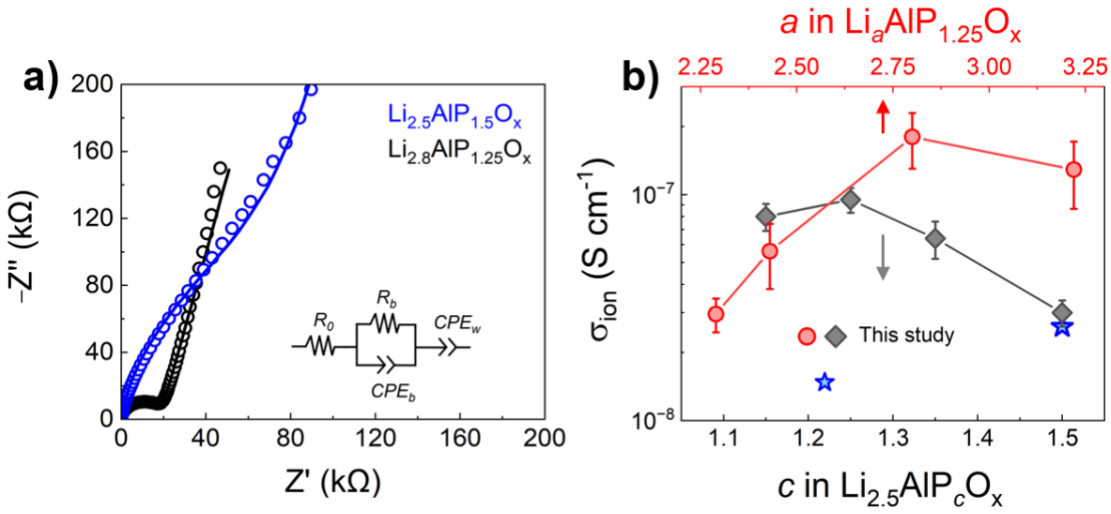

Figure 5.3 a) EIS Nyquist plots for two LAPO compositions with the equivalent circuit model used to fit the data (inset). **b)** σ_{ion} for various LAPO compositions determined from the fitted EIS data and the blue star representing the conductivity of the single composition $Li_{2.5}Al_1P_{1.5}O_{5.5}$ in literature.[133]

First, the P content in $Li_{2.5}Al_1P_cO_x$ was varied in the range $1.1 < c < 1.5$. EIS of all samples could be adequately fit with the ECM (Figure 5.3a inset) which is common for non-crystalline materials.[119] Good agreement with the previous work of Clayton et al. at $c = 1.5$ was observed. As the P content was decreased from 1.5 to 1.25, an increase in σ_{ion} from $3.0(4)\times10^{-8}$ S cm^{-1} to $0.95(12)\times10^{-7}$ S cm^{-1} was observed. Values of c below 1.15 resulted in films with poor coverage. Fixing the optimal value of $c = 1.25$, the Li content (a value) was subsequently varied. By increasing a from 2.25 to 2.8, the σ_{ion} increased by almost an order of magnitude (from $3.0(5)\times10^{-8}$ S cm^{-1} to $1.8(5)\times10^{-7}$ S cm^{-1}) highlighting the sensitivity of σ_{ion} to both Li and P content. Finally, the effect of P content in the Li-rich $Li_{2.8}Al_1P_cO_x$ was investigated, which confirmed the same optimal composition (Figure 5.4). Therefore, the initial exploration $Li_{2.8}Al_1P_{1.25}O_x$ of the Li-Al-P-O phase space yielded a maximum σ_{ion} of $1.8(5)\times10^{-7}$ S cm^{-1} for the composition To the best of our knowledge, this is the highest ionic conductivity reported for a lithium aluminophosphate glass at room temperature (Table 5.1).[133,148–150]

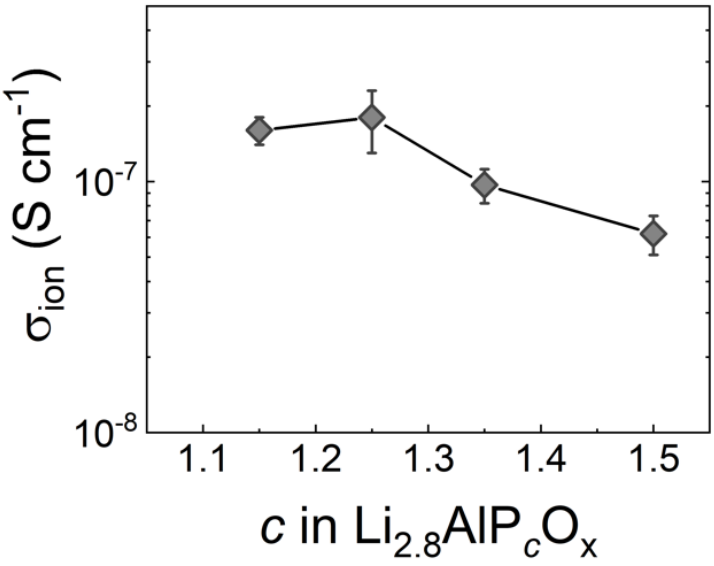

Figure 5.4 Ionic conductivity for $Li_{2.8}AlP_cO_x$ films determined from the fitted EIS data using the ECM displayed in Figure 5.4.

Table 5.1 *Comparison of ionic conductivity conducted at temperature T(K) of Li-Al-P-O bulk glasses and solution processed thin films.*[133,148–150]

Composition	Processing type	*T* (K)	σ_{ion} (S cm^{-1})	Reference
$Li_{2.8}AlP_{1.25}O_x$	Solution	295	1.8(5) x10^{-7}	This study
$Li_{2.5}AlP_{1.5}O_x$	Solution	295	2.6×10^{-8}	Clayton et al., 2017
$Li_{2.5}AlP_{1.5}O_{6.5}$	Melt	303	2.8×10^{-8}	Reddy et al., 2012
$Li_{2.33}AlP_5O_{15.67}$	Melt	403	2.1×10^{-7}	Sharma et al., 2009
$Li_{10}AlP_9O_{29}$	Melt	295 (extrapolated)	1.3×10^{-8}	Moreau et al., 2009

5.3.2 Effect of annealing temperature

From Figure 5.3, the LAPO film composition with the highest $\boldsymbol{\sigma_{ion}}$ ($Li_{2.8}Al_1P_{1.25}O_x$) was chosen and the conductivity as a function of annealing temperature, T_{anneal} studied. An inverse relationship between $\boldsymbol{\sigma_{ion}}$ and T_{anneal} was discovered, with $\boldsymbol{\sigma_{ion}}$ decreasing by a factor of ≈4 from 230 to 400 °C (Figure 5.5). This observation is in contrast to the work of Clayton et al.[133] who found negligible ionic

conductivity (≈10^{-10} S cm^{-1}) after annealing $Li_{2.5}Al_1P_{1.5}O_x$ films at 400 °C, suggesting a complex relationship between composition, annealing temperature and film structure in this system.

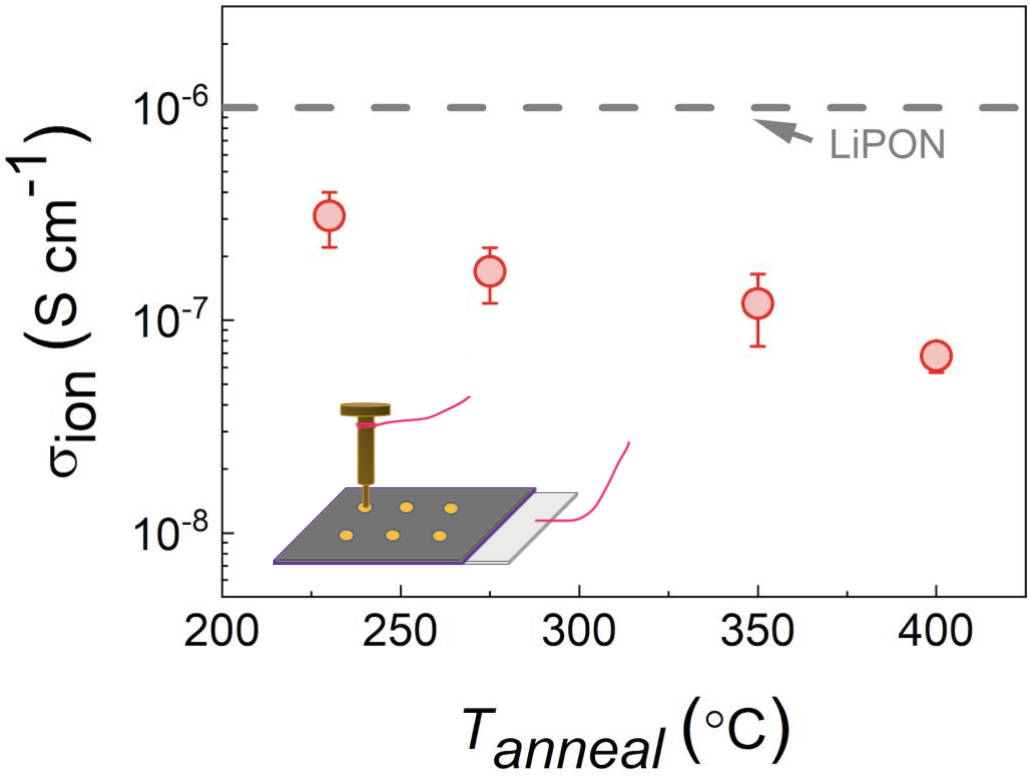

Figure 5.5 The σ_{ion} variation for $Li_{2.8}AlP_{1.25}O_x$ films as a function of annealing temperature, conducted at room temperature with the inset displaying the Au contacts on top of the film and Si substrate, with Al contact on the bottom. A gold screw contacts the top of the Au contact, and the Al bottom is bonded to a wire (pink line) with epoxy paste. Both wires are connected to a potentiostat to run EIS. LiPON conductivity is shown for comparison (dashed grey line).

The most conductive films had σ_{ion} values within an order of magnitude of state-of-the-art LiPON SEs (σ_{ion} ≈2×10^{-6} S cm^{-1}).[151] It is noted that the LiPON SEs used in SSBs are typically several microns in thickness, so comparable bulk resistance values would be expected for the thinner LAPO films (i.e., 100s of nms) used here. Annealing at temperatures less than 230 °C resulted in appearing visually spotty and inhomogeneous coverage of the Si substrate. Crystallisation may occur at

higher annealing temperatures and affect ionic properties. Laboratory GI-XRD showed no signal above the background of the fused silica substrates, indicating the films were non-crystalline at all annealing conditions investigated here (Figure 5.6).

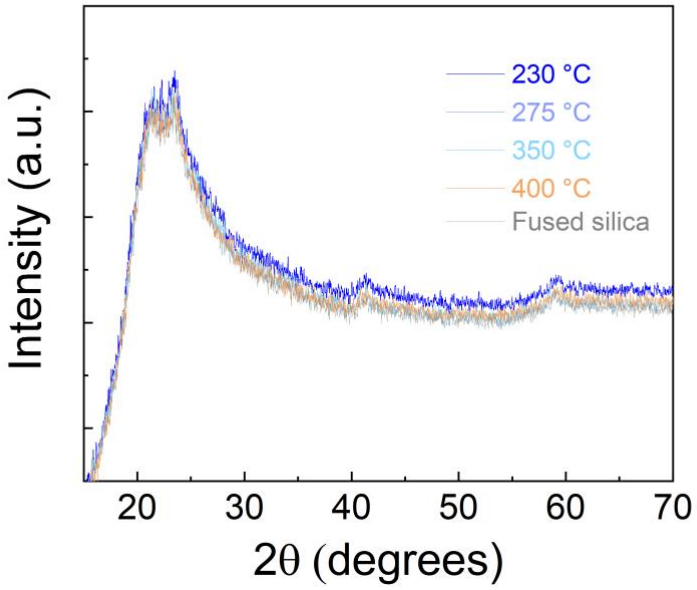

Figure 5.6 Theta-theta XRD on LAPO films annealed at 230, 275, 350, 400 °C. No detectable signal from the films is seen above that from the fused silica substrate.

5.3.3 X-ray Photoelectron Spectroscopy

XPS was used to quantify the elemental composition and oxidation states of the films. Representative region scans are shown in Figure 5.7. All films contained chemical species in the expected charge states: Li^{+}, Al^{3+}, P^{5+} and O^{2-} with a higher binding energy shoulder peak in the latter indicative of defective oxygen or surface hydroxides.[152,153] No N signal was detected, consistent with the loss of nitrates during annealing.

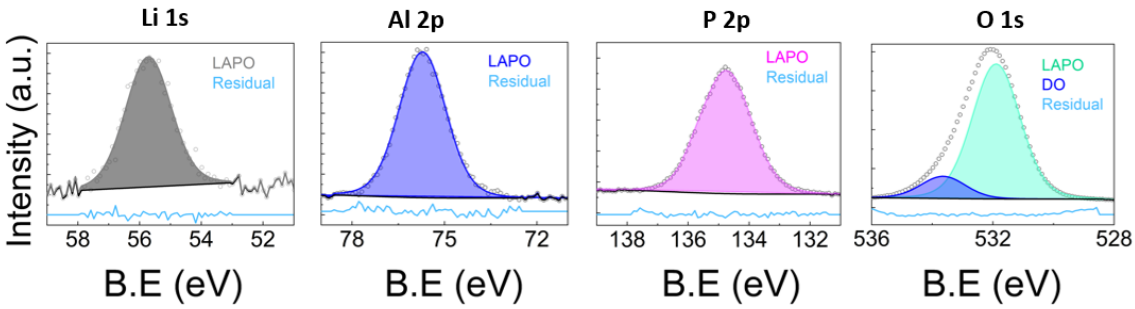

Figure 5.7 Representative XPS region spectra for a $Li_{2.8}AlP_{1.25}O_x$ film.

Table 5.2 contains the surface compositions of LAPO films annealed at different temperatures. At the intermediate T_{anneal} values of 275 and 350 °C, the measured values were in good agreement with stoichiometries expected based on the precursor solution composition. XPS is a surface sensitive technique, therefore this result implies chemical homogeneity throughout the film thickness. At 400 °C, the XPS results show greater Li and O contents at the film surface Li-O species would be expected to be ionically insulating and consistent with the lower $\boldsymbol{\sigma_{ion}}$ observed in Figure 5.5 On the other hand, at 230 °C greater relative Li and P concentrations were observed in addition to the highest $\boldsymbol{\sigma_{ion}}$. Future work will investigate controlling the chemical inhomogeneity of the films during synthesis, e.g., by intentionally depositing layers of dissimilar composition, in addition to further exploration of the Li-Al-P-O phase space.

Table 5.2: *Film surface composition determined by XPS*

T_{anneal} (°C)	Stoichiometry in $Li_aAl_bP_cO_x$			
	a	*b*	*c*	*x*
230	3.0	1	1.4	5.2
275	2.8	1	1.3	5.1

350	2.7	1	1.3	5.2
400	2.9	1	1.2	5.6

The film surface morphology as a function of annealing temperature was determined with AFM (Figure 5.8a). All films exhibited low average surface roughness (R_a) < 10 nm, with T_{anneal} = 275 °C exhibiting the lowest R_a of ≈1 nm. A complex relationship was evident and reproducible across multiple samples – likely due to competing processes, such as evaporation and surface reorganization, occurring during annealing.

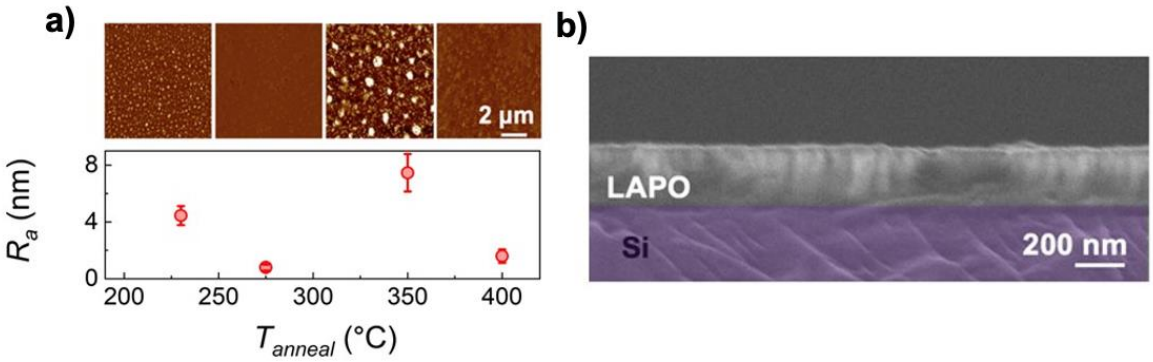

Figure 5.8 a) AFM of the surface of single layer films and their average roughness (R_a) as a function of annealing temperature displayed underneath. **b)** Cross-sectional SEM image of a 4-layer $Li_{2.8}AlP_{1.25}O_x$ film on an Si substrate annealed at 275 °C.

The Young's modulus was determined by nanoindentation in the AFM to be 54(4) GPa. This value is greater than that of sulfide SEs (≈15-20 GPa)[154–156] and close to that of LiPON (77 GPa),[157] suggestive of LAPO being sufficiently tough to suppress Li dendrite propagation. Due to the combination of low surface roughness, chemical homogeneity and near-peak ionic conductivity, 275 °C was chosen as the optimal annealing temperature for subsequent investigations – the abbreviation LAPO will refer to this film composition annealed under these conditions for the remainder of the manuscript. SEM imaging confirmed these SE

films were continuous and dense (Figure 5.8b), with a single layer thickness of ≈75 nm.

5.3.4 Activation energy analysis

The activation energy, E_a of optimised LAPO was determined using an Arrhenius relationship (Equation 5.7, Figure 5.9) as 0.42(1) eV for the film annealed at 275 °C. All LAPO films displayed activation energies in the range 0.39-0.47 eV. A general trend was observed that the activation energy increased as the room temperature ionic conductivity decreased, consistent with more facile ion transport leading to higher ionic conductivity. Table 5.3 shows the activation energy values (plot of temperature dependent ionic conductivity measurements for 230, 350 and 400 °C in the Appendix, A.4).

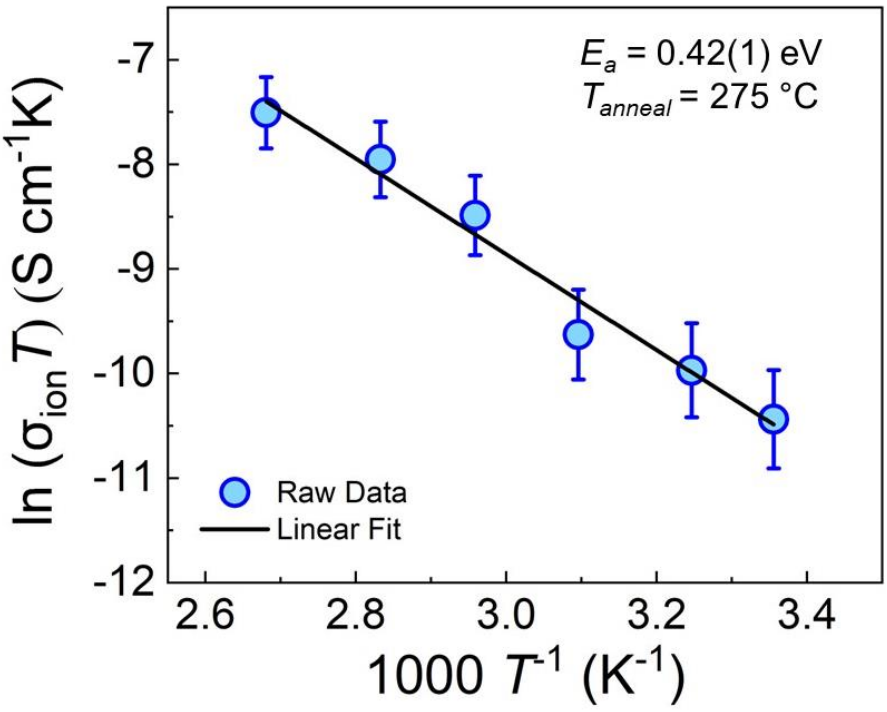

Figure 5.9 Temperature-dependent $\boldsymbol{\sigma_{ion}}$ measurements and activation energy analysis.

This value is lower than those reported for thin film and bulk $Li_{2.5}AlP_{1.5}O_{5.5}$ glasses, 0.67 and ≈0.6 eV respectively,[133,148] and even lower than that reported for LiPON (≈0.55 eV),[157] despite the latter's higher room temperature conductivity.

This can be rationalised by considering the greater Li content of LiPON[158] compared to LAPO, which is incorporated in the conductivity pre-factor term in Equation 5.7. Additional differences in pre-factor parameters, e.g., hopping frequency, may also contribute. Returning to the other LAPO phases, additional Li in the structure could provide additional charge carriers. However, the optimised composition contains only slightly more Li (≈10%) than those reported previously.

Table 5.3 *Activation Energy values calculated from Temperature-dependent* $\boldsymbol{\sigma_{ion}}$ *measurements.*

T_{anneal} (°C)	Activation Energy (eV)
	E_a (eV)
230	0.39(7)
275	0.42(1)
350	0.44(6)
400	0.47(3)

It is therefore likely that by altering the Li:Al:P ratios has modified the glassy network of Al-O and P-O units, creating a more favourable pathways for Li^+-ion transport. No significant differences were observed in XPS spectra and no structural information could be obtained by XRD (Figure 5.6).

5.3.5 Electronic conductivity

The bulk electronic conductivity (σ_e) of SEs has been suggested to be an important factor in the prevention of Li dendrites.[7] To determine the σ_e, a DC voltage was applied, and the subsequent current decay monitored (Figure 5.10). From this steady-state current value, the $\sigma_e$of LAPO was calculated as ≈10^{-11} S cm^{-1}, ≈4 orders of magnitude lower than the σ_{ion} and yielding a transference number of ≈1 assuming only the Li^+ ions are mobile. This value for LAPO compares well to that reported for LiPON (≈10^{-11}-10^{-14} S cm^{-1}),[7,159] and is significantly lower than those for $Li_7La_3Zr_2O_{12}$ (LLZO) and Li_3PS_4 (LPS) SEs (Figure 5.10, inset).

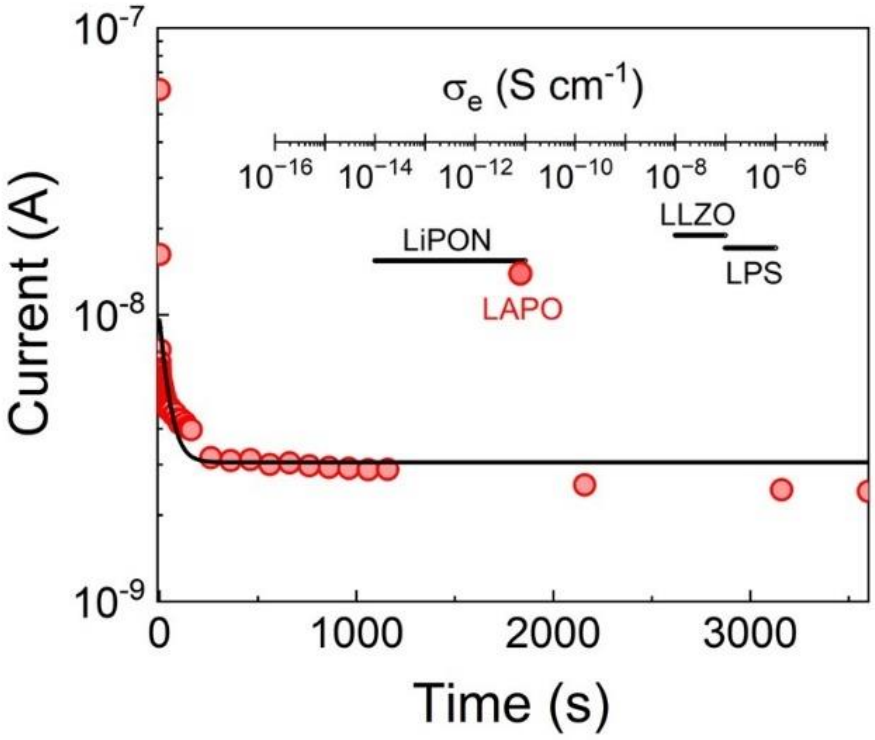

Figure 5.10 Current-voltage decay curve for a $Li_{2.8}AlP_{1.25}O_x$ film annealed at 275 °C. Comparison of the $\boldsymbol{\sigma_e}$ of LAPO against SEs in literature (inset).

5.3.6 Stability against Li metal

The electrochemical stability of LAPO was tested against Li metal using time dependent EIS (Figure 5.11a). The EIS data were fit using 3 *R*|*CPE* units[160] (ECM inset in Figure 5.11 a and zoomed in scale to resolve 0 h in Figure 5.11 b). Here, R_1 represented the bulk SE impedance (R_b), R_2 the passivation layer (R_p) due to LAPO decomposition and R_3 the charge transfer at the Li interface. DRT analysis[147,161] was used to deconvolute the different polarisation processes. To test the linearity, stability, and causality of the EIS data, the Kramers-Kroning relation was first applied. The residuals were fixed to be ±1% for the processes occurring at high-to-mid frequencies corresponding to the passivation and bulk SE resistances R_b and R_p, respectively. However, at mid-to-low frequencies the DRT residuals were outside the set range, possibly due to the non-linear nature of the charge transfer reactions occurring at the Li interface.

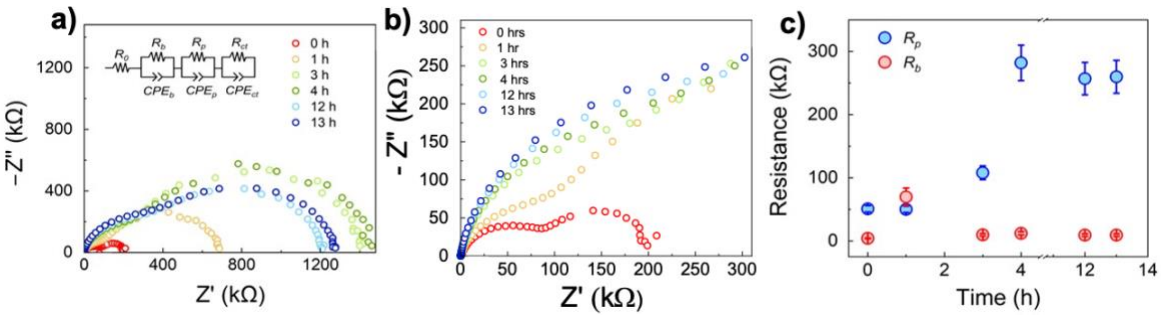

Figure 5.11 a) EIS Nyquist spectra of $Li_{2.8}AlP_{1.25}O_x$ against Li metal over 13 hrs, **b)** zoomed in to resolve the 0hr semi-circles. **c)** Comparison of R_b and R_p vs. time. The resistance values were extracted from DRT analysis (Figure S5 in the SI).

Therefore, it was not possible to meaningfully quantify the R_{ct} values. The non-linearity of the R_{ct} and shift in time processes can be observed in the DRT plot (Figure 5.12) Figure 11 c shows that R_b was fairly invariant with time, with an anomaly at 1 h which is attributed to the decomposition reaction of LAPO with Li.

The characteristic frequencies (time constants) for R_b, R_p and R_{ct} were ≈50 kHz (20 μs), ≈5 kHz (0.2 ms) and ≈100-1000 Hz (1-10 ms) respectively. A stable passivation layer or interphase was formed after ≈4 hours with a ≈25× greater impedance than the bulk SE. Reactivity with Li is true of all known SEs, with only LLZO and LiPON forming stable, low impedance interphases against Li to the authors' knowledge.[162–164] The result that the native LAPO-Li interphase is stable is promising for future surface modification and composition engineering efforts to reduce or eliminate impedance due to the formed interphase.

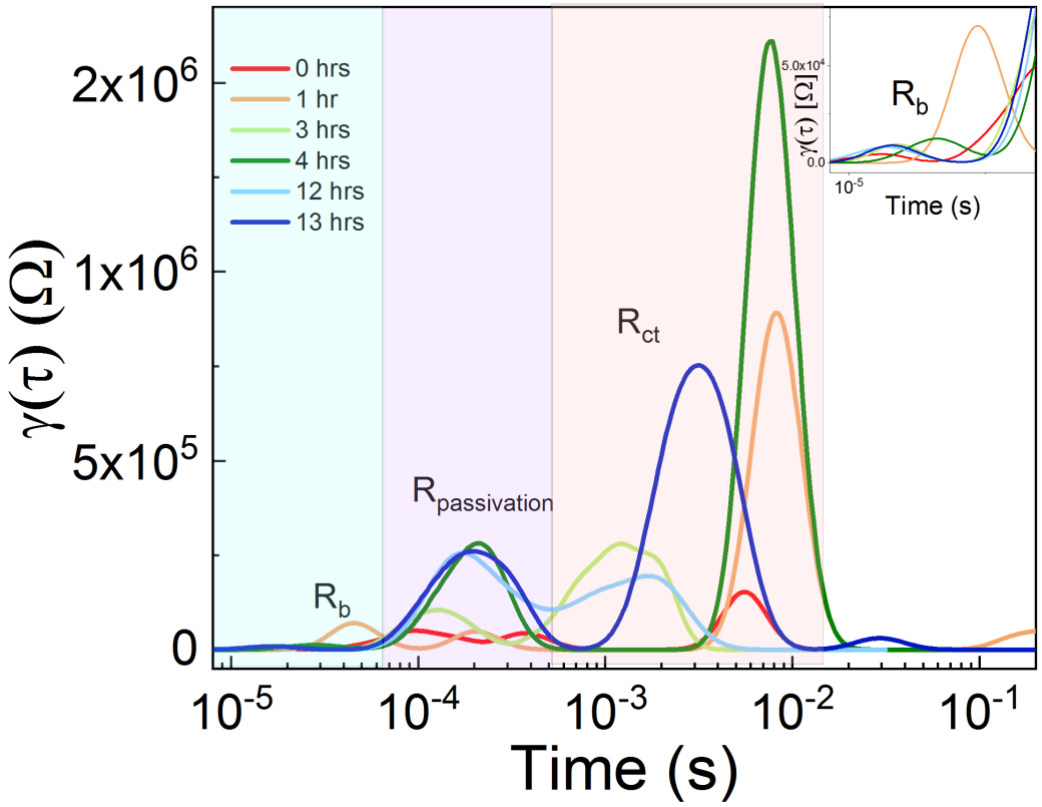

Figure 5.12 DRT analysis of EIS data vs. time for LAPO|Li from which R_b, R_p and R_{ct} can be determined. The inset shows the R_b at different times.

5.3.7 In situ XPS during Li deposition

To elucidate the interphase composition, in situ XPS was performed, monitoring the core-level photoemission spectra Li 1s, Al 2p, P 2p and O 1s during Li deposition (Figure 5.13). In all cases, the pristine components remained in addition to new features caused by reaction with Li, suggesting either that LAPO exists as part of the passivation layer or that this layer is thin enough to permit sampling of the underlying SE. In the case of Li 1s, a new feature appeared at lower BE (≈53.7 eV). This was likely due to the formation of Li-containing decomposition products, such as Li_2O, Li_3P, Li_xP and surface-absorbed contaminants such as Li_2CO_3, etc. After 60 min, an additional peak at lower BE emerged (≈52.7 eV) associated with Li^0. A significant fraction of the Al^{3+} initially present was reduced to Al^0 during Li deposition, whilst P^{5+} was reduced to Li_3P (126.5 eV) and partially reduced Li_xP species (131.0 eV). A very similar evolution of the P 2p spectra was observed during in situ XPS of LiPON.[165] Finally, a new feature at lower BE was detected in the O 1s spectra, which grew to dominate with time and could be assigned to Li_2O. Although there will be some Li_2O present due to the deposited Li reacting with surface contaminants and trace O_2/H_2O present inside the XPS chamber,[166] it is likely that a majority of the Li_2O formed as a result of direct reaction with LAPO considering the greater impedance of the interphase. Therefore, the passivation layer was found to be a mixture of Li_2O, Li_3P, Li_xP and Al^0 species. A stable interphase should contain ionically conducting and electronically insulating decomposition products.[167] Considering the chemical information from XPS and the resistive interphase revealed by EIS, it is speculated that the electrically

conductive components (Li_3P, Li_xP, Al^0) were isolated in a matrix of Li_2O, which is a known electronic insulator.[168]

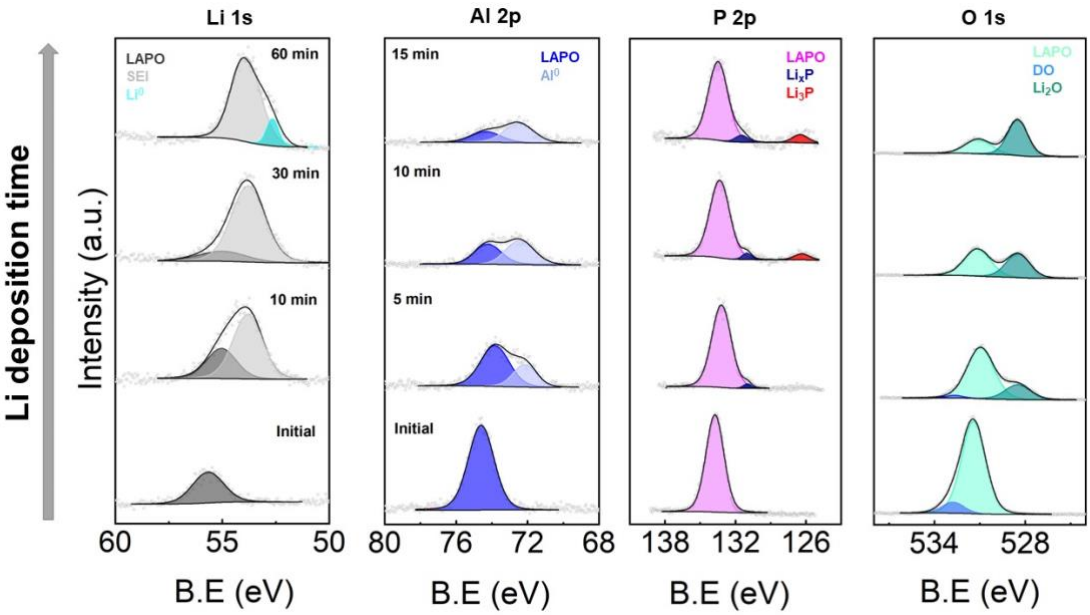

Figure 5.13 Evolution of core level XPS spectra during Li deposition on the $Li_{2.8}AlP_{1.25}O_x$ surface. Note that the deposition times given for the Al 2p spectra also apply for P 2p and O 1s panels.

5.4 Conclusion

In summary, NC Li^+-ion SE thin films are synthesised from aqueous solutions. Through systematic exploration of the Li-Al-P-O phase space, an optimal composition of $Li_{2.8}AlP_{1.25}O_x$ was identified with an σ_{ion} >10^{-7} S cm^{-1} at room temperature. Both increased Li and decreased P content were required to maximise the ionic conductivity. Higher annealing temperatures led to decreased σ_{ion} between 230 and 400 °C in this system. Film surface roughness exhibited a complex dependence on annealing temperature, with the smoothest films being produced at 275 °C. Temperature-dependent σ_{ion} measurements yielded a low activation energy of 0.42(1) eV, indicating facile Li^+-ion transport in this non-crystalline SE. DC

polarisation experiments revealed a low σ_e (≈10^{-11} S cm^{-1}) and a moderate Young's modulus of ≈54 GPa was also determined. In contact with Li metal, LAPO formed a stable, but resistive passivation layer and in situ XPS showed this to consist of Li_2O, Li_3P, Li_xP and Al^0 species. Reactivity with Li is true of all known SEs, with only LLZO and LiPON forming stable, low impedance interphases against Li to the authors' knowledge. The result that the native LAPO-Li interphase is stable is promising for future surface modification and composition engineering efforts to reduce or eliminate impedance due to the formed interphase. These findings should motivate future investigations into solution-processed NC materials.

Chapter 6

Conclusion and Outlook

6.1 Thesis Conclusions

This thesis has focused on probing the NE|SE interface in SSBs to enable high cycle life SSBs. It was shown that Si could be a promising NE in a SSB by providing high-rate capability in thin film SSBs. However, the Si diffusion and mechanical properties greatly influence cycle life due to the large stress-strains in this system as a result of the large volumetric expansion of Si during cycling.

In Chapter 3, an 2D echem-mech model was first constructed and experimentally validated using steady-state, transient and pulsed electrochemical methods. The model geometry was taken as a representative cross-section of a non-porous, thin-film solid-state battery with an amorphous Si (*a*-Si) NE, LiPON SE and LCO PE. A viscoplastic model was used to predict the build-up of strains and plastic deformation of *a*-Si as a result of (de)lithiation during cycling. A suite of electrochemical tests, including EIS, GITT and HPPC was carried out to establish key parameters for model validation. Thereafter, the validated model was used to explore the peak interfacial (*a*-Si|LiPON) stress and strain as a function of the

relative electrode thickness (up to a factor of 4), revealing a peak volumetric expansion from 69% to 104% during cycling at 1C. The understanding of electrode thickness on the stress and strain response was a key outcome of the model as well as the model validation using load and pulsed (not routine for SSBs) operating conditions which will aid in the cell design and optimisation of SSB technologies.

Next, in Chapter 4, the objective of the validated 2D echem-mech model was to understand the effect of applied pressure and C-rate on the stress-strain response of the cell. This study looked to probe the evolution of stresses at the solid-solid interfaces. Although the validation and implementation of the model in the previous chapter is important, it was only in this chapter that the interplay of the internal electrochemistry and mechanics within the SSB domains was investigated. The usefulness of having a model to probe these internal effects was highlighted when a complex concentration gradient was generated within the Si electrode due to slow Li diffusion in Si which led to localised strains. Of particular concern was that at the end of discharge, at high C-rates (5C) under low applied pressure, the maximum stress generated was tensile and occurred at a distance (0.9 normalised distance from the negative CC) into the Si electrode.

These tensile stresses are of concern as fracture could occur here, and it is non-trivial that the fracture propagation could occur at a distance within the Si electrode, rather than at the Si|LiPON interface. Additionally, the simulated results showed that to reduce the interfacial stress and strain at 100% SOC, low to moderate C-rates and applied pressure is desirable. Following this, the mechanical properties of the SE was tailored for optimal cell performance. To reduce Si stress, a moderate Young's modulus similar to that of lithium phosphorous oxynitride (≈77GPa) with a low yield strength comparable to sulfides (≈0.67 GPa) should be selected. However, if the reduction in SE stress is of greater concern, then a compliant Young's modulus (≈29 GPa) with a moderate yield strength (1-3 GPa) should be adopted. The importance of a validated echem-mech model is shown in this work and is a useful tool when optimising cell material design for high rate and long cycle life. This study also emphasises the need for experiments on the characterisation of post-yield SE behaviour to improve model accuracy and the

need for SE material selection and design to optimise the performance of thin film SSBs.

When considering the scalable synthesis and manufacturing of large format SSBs, the LiPON SE whilst enabling a high cycle life in thin film format and its superior stability against Li metal (for use in Li metal batteries), is not scalable. One of the aims of this thesis was to discover a material similar to LiPON in its electrochemical and mechanical properties, whilst being low cost and highly scalable. Chapter 5 looked beyond LiPON to another NC material, LAPO which was synthesised using scalable methods and its phase space explored consisting of seven different compositions. It exhibited an ionic conductivity $>10^{-7}$ S cm^{-1} at RT by spin coating from aqueous solutions and subsequent annealing in air. Homogenous, dense, flat layers were synthesised with sub-micron thickness at temperatures as low as 230 °C. Control of the composition was shown to significantly affect the ionic conductivity, with increased Li and decreased P content being optimal, while higher annealing temperatures result in decreased ionic conductivity. Activation energy analysis revealed a Li^+ ion hopping barrier of 0.42(1) eV. Additionally, LAPO exhibited a low room temperature electronic conductivity ($<10^{-11}$ S cm^{-1}) and moderate Young's modulus of ≈54 GPa, which may be beneficial in preventing Li dendrite formation. In contact with Li metal, LAPO is found to form a stable, but high impedance passivation layer comprised of Al metal, Li-P and Li-O species. These findings should be of value when engineering NE SEs for Si or Li-metal batteries with high energy and power densities. In this work, a foundation has been established which can be used to further improve NC materials' interfacial properties for use in advanced energy storage devices.

The cumulative sum of the electrochemical and mechanical techniques used in this thesis, although not completely comprehensive, is rarely reported in the field of SSBs. Techniques such as pulse-power characterisation, EIS and DRT analysis to assign the Li-Si alloy interface contribution, continuum-scale modelling of a thin film Si based SSB with experimental validation, investigation of the SE (LAPO) conductivity-structure relationship and its stability with Li using in-situ XPS and

time-dependent EIS and DRT analysis, are uncommon and will expand understanding of the NE|SE interface. The methods described here, have been applied to a multitude of different SEs (experimental and simulated) and NE (Si and Li) chemistries to gain a deeper insight into the high interfacial resistance which is one of the main drawbacks for SSBs. These techniques and insights should help to motivate further studies towards commercialisation of SSBs with superior cycling performance.

6.2 Limitations

6.2.1 Cell Format

The focus of this work is mainly on thin film systems and the echem-mech model simulated for a thin film SSB (Chapters 3 & 4). The simplistic, planar geometry provides a useful learning tool to understand the cell strain-strain response and the suite of electrochemical testing applied to the SSB (albeit thin film) can be applied to extract parameters for a porous SSB as we shift towards the commercialisation of these larger form factor SSBs (not commercially available today). Although experimental visualisation of the expansion of Si could not be measured on the thin film system, on a large format system this is made easier. For instance, X-ray computed tomography (X-ray CT) was unsuccessful on the thin film SSB, due to the high aspect ratio of these thin films, submicron thickness and low X-ray attenuation of Si, the resolution and pixel size was not able to identify Si expansion. However, with large format cells (~100 s micron thickness), X-ray CT is more successful and has been used in studies to visualise dendrite formation and for modelling electrode particles. Experimental parameters such as electrode diffusion can also be extracted from X-ray CT to improve model validation. 3D microstructure resolved SSB models have recently emerged[98,115] though only on the scale of a few particles not full electrode level and the inclusion of degradation mechanisms such as fracture and loss of contact between the SE and electrode have not been as thoroughly modelled.

Both experimental and modelling efforts on large format cells during cell cycling and applied pressure should be conducted to improve model accuracy and increase understanding of applied pressure on these large format 3D systems. The map of applied pressure, C-rate and capacity produced in Chapter 4 is very useful for not only understanding the internal stress-strain response of the cell but also for cell design. A thorough characterisation of a large format SSB to create a similar map would be highly useful.

6.2.2 Plastic Behaviour

The echem-mech model (Chapters 3 and 4) assumed perfectly plastic yield behaviour for LiPON as the post yield behaviour and fracture toughness of LiPON is lacking in literature and future studies should look at extracting this.[169] It will improve model accuracy and enable models to predict fracture modes in SSBs. In addition, the creep behaviour of the oxide and sulfide SEs in this study (LLZTO and LPSCl), did not take into consideration hardening of these materials which could occur as the stress is increased and would alter the strain rate. The reason for not simulating this response is due to the lack of experimental studies on post-yield behaviour even for these commonly used SEs. Moreover, due to the planar nature of the thin film SSB, elastic isotropy was modelled which would not be the case for systems with electrode microstructure and composite NEs/PEs (e.g., large format SSBs), therefore the model would need to be adjusted for these cases.

6.2.3 Half-Cells

The Si plastic stress and strain fitting parameters were taken from literature using curvature measurements that had been performed on *a*-Si half cells with LEs.[16, 17] It would be beneficial for future SSB modelling efforts if such studies could be conducted on *a*-Si half cells with SEs. More experimental studies should focus on reporting OCV curves and diffusion coefficients for *a*-Si and PE half cells with SEs to improve model accuracy rather than relying on data from LE half cells in

literature. The findings in Chapter 3 showed better cell capacity agreement (during 1C cycling) using Si and LCO solid-state diffusion coefficients determined using GITT on the full cell SSB rather than LE data. However, the model could be further improved by a more accurate OCV, and diffusion coefficient obtained using representative SE half-cell data.

6.2.4 Applied Pressure

This work acknowledges that the applied stack pressure in Chapter 4 was simulated between 0 to 500 MPa which is a little higher than used experimentally. Typically, fabrication pressures of large format SSBs are a few hundred MPa with typical stack pressures $\leq$100 MPa[170–172] and in rare cases up to 250 MPa.[173] However, this work wanted to understand the relationship between applied pressure and C-rate on the cell stress-strain response and capacity. Therefore, the applied pressure range was extended to 500 MPa to better display the complex relationship and visualisation of any trends that emerged, for example the C-rate was found to influence the cell average capacity much more than the applied pressure (Figure 4.6 and 4.7).

6.2.5 Contact Resistance

It is recognised that the variable contact resistance of the gold screw when conducting EIS measurements on LAPO influences the ionic conductivity values between samples (~16%). Due to the small contact area of the gold tip (0.20 mm^2) it is extremely difficult to control the pressure by hand, therefore an automated method could be deployed to apply a controlled and quantified amount of pressure for each sample measurement. Alternatively, a torque meter could be calibrated and used to measure the applied pressure to the screw if an automated EIS set-up is not available.

6.2.6 Spin coating

The synthesis process used for LAPO whilst using low-cost precursor materials and aqueous processing methods with a low annealing temperature, does not use a highly scalable deposition technique. The use of spin coating is not thought to be scalable for large scale manufacturing processes. Spin coating has been used in this thesis as a platform to enable the deposition of these films and enable investigation of the electrochemical and mechanical properties. Spin coating provides a quick and simple method to tweak the chemistry of the films and provide feedback on film properties as a result. When these films are ready for employment in device level systems, more scalable routes should be investigated for scale-up. Methods such as spray coating should be studied, and the film's properties characterised to confirm similarity with those synthesised using the spin coating technique.

6.3 Future Work

6.3.1 Fracture Model

Mechanical properties of the SE such as its Young's modulus, yield and fracture strength were found to play a role in the SSB performance (Chapter 4). It is likely that these properties influence whether fracture will occur within the Si and SE due to defects within these materials. Defects are common during the manufacturing process[53,174] and future work should look at probing whether fracture will occur. Chapter 4 (Figure 4.7) highlighted areas of high tensile stress at the Si|LiPON interface which occurred at the end of discharge. This high tensile stress could provide sites for fracture; however, it is possible that a certain amount of applied pressure could mitigate it. Future work should look at probing possible fracture sites and under which conditions it could be prevented. Modelling a defect at the Si|SE interface as well as within the Si and SE could be of interest. Further, the effect of applied pressure on the electrochemical properties of the SE such as its ionic conductivity and the interfacial resistance (SE|Si interface) was not simulated, yet literature points to increased SE ionic conductivity and reduction in interfacial

resistance with applied pressure.[172] The relationship between applied pressure on ionic conductivity and interfacial resistance should be implemented into the model for increased accuracy. Mechanical integrity is one of the main issues for thin film SSBs [175] and by building a more robust echem-mech model to better understand the electrochemical and mechanical interplay, it can provide as a useful tool for the creation of high cycle-life thin film SSBs.

6.3.2 Non-crystalline Solid Electrolytes

It is difficult to see how expensive and slow throughput vacuum processing of SEs such as LiPON will enable the scale-up of large format SSBs.[53,176,177] Vacuum processing of thin films on large areas as required for large format cells will not be cost competitive and are limited in their applications as small format devices consisting of microbatteries and microelectronic chips. Therefore, scalable solution-based processing of a NC material with similar properties to LiPON is highly desirable. In Chapter 5, such a NC material has been synthesised; LAPO, and the phase space of this class of materials should be further expanded. Spray coating would be more suited to large scale synthesise of these films compared to spin coating and should be explored as a route for scaling. LAPO produced a stable but high impedance interface with Li and future work should focus on producing a stable and low impedance interfacial contact. This could be achieved by doping the films with nitrogen which has increased the stability of LiPON against Li.[178]

Future work should also look at integrating the LAPO films into devices by either spin-coating the film in an "anode-free" configuration or coating directly on to a PE to provide better contact at the SE|PE interface. In the former configuration, the LAPO film would be spin coated onto the negative CC and assembled with a lithium containing PE. The lithium NE would be formed from the lithium contained in the PE which would deposit in-situ at the negative CC interface during charging (Figure 6.1a). The LAPO film would enable stable plating and stripping of Li at the negative CC in a thin film SSB or in a Li metal battery containing a LE or SE (Figure 6.1b and Figure 6.1Figure 6.1c respectively). Coating LAPO directly onto a PE to help improve the stability of the PE at higher voltages could be paired with

either a Li or Si NE. However, this configuration is dependent upon whether the electrochemical stability window of LAPO encompasses a large voltage range and should be investigated in future experiments.

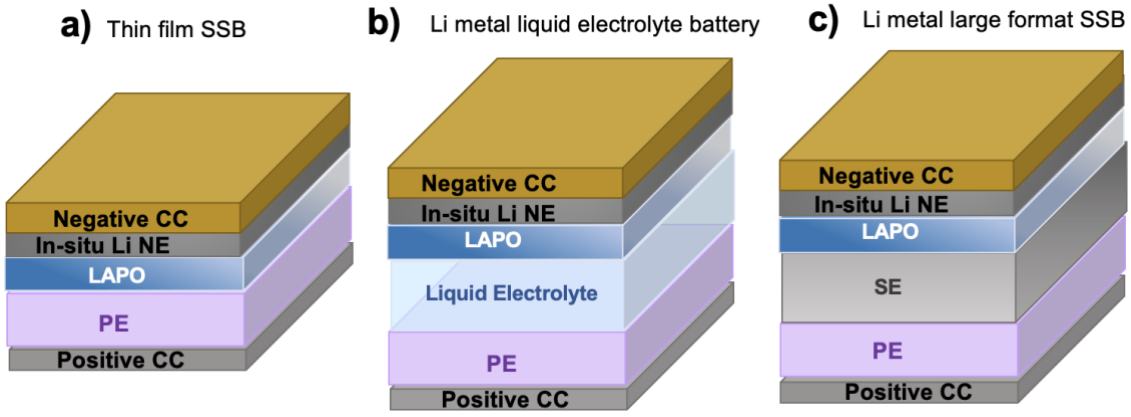

Figure 6.1 a) LAPO SE used to enable stable plating and stripping of Li (formed in-situ) at the negative CC in a thin film SSB, **b)** in a Li metal LE battery and **c)** a Li metal all solid-state large format battery.

Previous work has looked at the ability of LiPON to increase the wettability of different SEs against the Li electrode thereby improving interfacial contact, whilst increasing the SE's electrochemical stability window and its critical current density thus prolonging cycle life. [179–181] Using LAPO in a similar fashion to increase the wettability of a bulk SE in a large format SSB could be similarly demonstrated to see whether the interfacial contact is improved with its addition. Finally, the SE phase space should be expanded to include the discovery of other NC materials synthesised using similar scalable methods in the pursuit of high ionic conductivity SEs with desirable electrochemical and mechanical properties.

Appendix

DRT Residuals

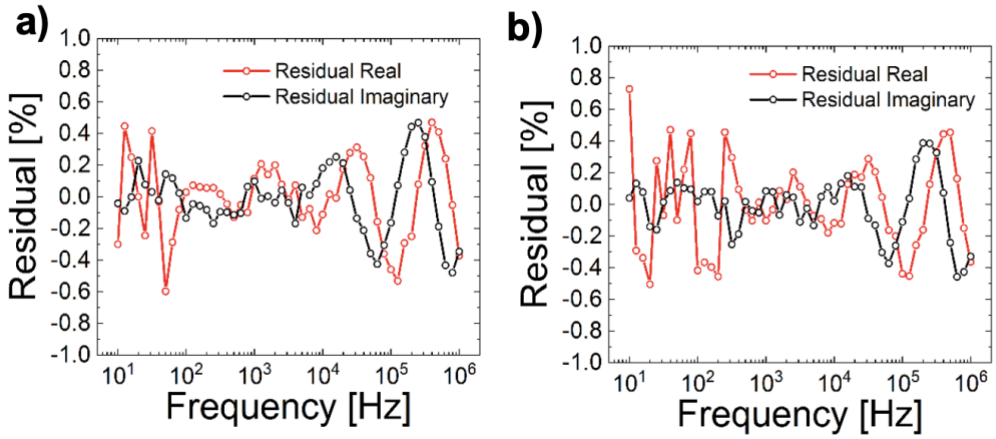

Figure A.1 Residuals for discharge EIS at **a)** 90% and **b)** 10% SoC.

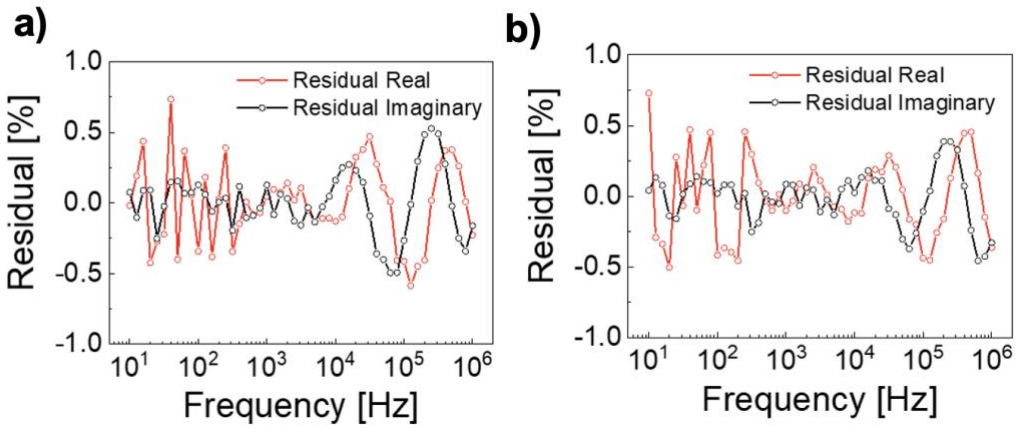

Figure A.2 Residuals for charge EIS at **a)** 90% and **b)** 10% SoC.

LAPO Pouch cell set up for time dependent EIS tests

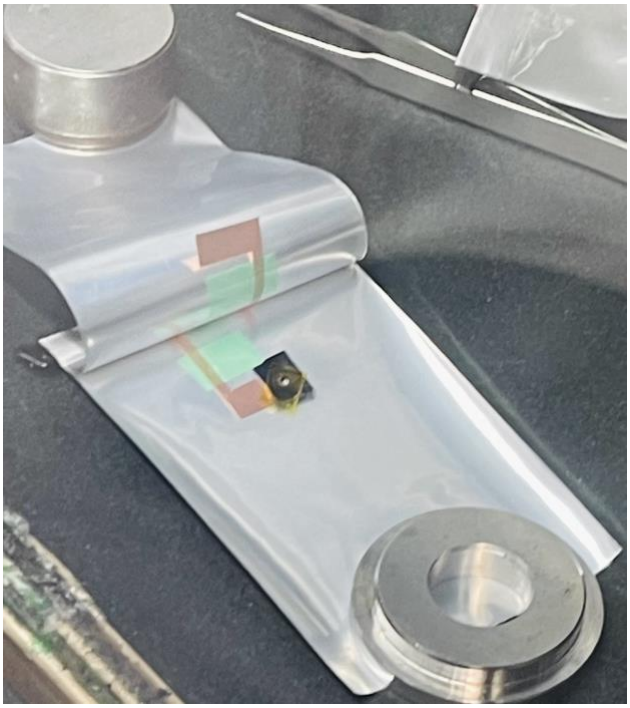

Figure A.3 LAPO spin coated onto the Si substrate with the Li "silver" spot thermally evaporated onto the film. Kapton tape was placed around the rest of the film to ensure the Cu contacts did not touch it.

Temperature dependent conductivity for activation energy analysis of LAPO

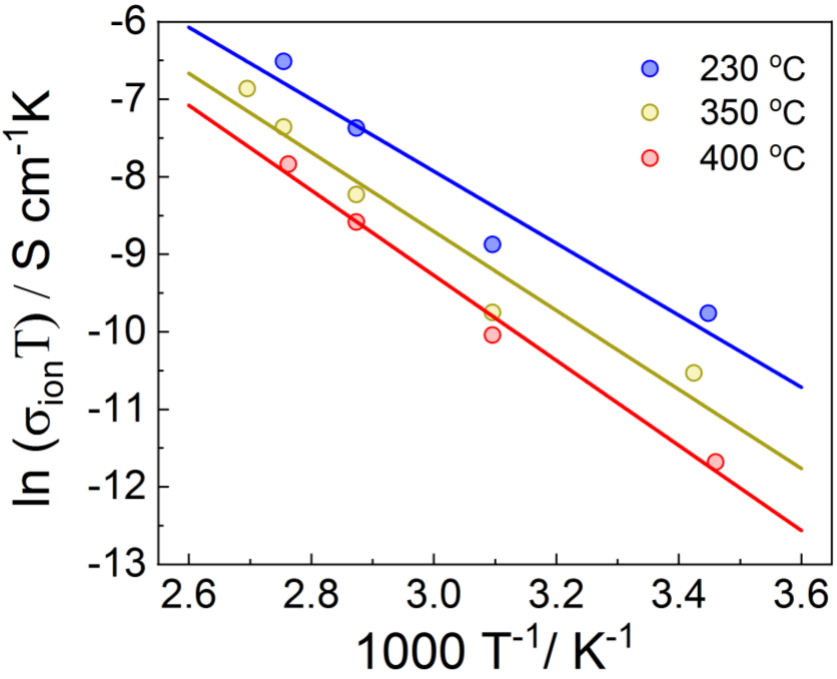

Figure A.4 Temperature-dependent ionic conductivity measurements and activation energy analysis on $Li_{2.8}AlP_{1.25}O_x$ films annealed at 230, 350 and 400 ºC.

Publications, Conferences, Awards, and Internships

Conferences:

1. Oral presentation at the Climate Change Conference organised by National Battery Research Institute (NBRI), 2021, *virtual*
2. Poster presentation at Materials Research Society, May 2022 at Honolulu, Hawaii
3. Oral presentation at the Royal Institute London, on work conducted as part of the STFC award recipient, November 2022, at London, U.K.
4. Poster presentation acceptance at the Solid-State Batteries - From Fundamentals to Application (SSB V), November 2022 at Frankfurt, Germany (could not attend due to personal circumstances).
5. Oral presentation acceptance at the Electrochemical Society (ECS), May 2023, Boston, U.S.A.

Publications:

1. First author review paper on electrochemical impedance spectroscopy for solid-state batteries, 2021 (published):

   Vadhva, P.; Hu, J.; Johnson, M. J.; Stocker, R.; Braglia, M.; Brett, D. J. L.; Rettie, A. J. E. Electrochemical Impedance Spectroscopy for All-Solid-State Batteries: Theory, Methods and Future Outlook. *ChemElectroChem* **2021**, *8* (11), 1930–1947. https://doi.org/10.1002/CELC.202100108.

2. First author research paper on a thin film Si NE solid-state battery, 2022 (published):

   Vadhva, P.; Boyce, A.; Hales, A.; Pang, M.-C.; Patel, A.; Shearing, P. R.; Offer, G. J.; Rettie, A. Towards Optimised Cell Design of Thin Film Silicon-Based Solid-State Batteries via Modelling and Experimental Characterisation. *J Electrochem Soc* **2022**. https://doi.org/10.1149/1945-7111/AC9552.

3. First author experimental paper on a non-crystalline thin film solid electrolyte, 2023 (published):

   Vadhva, P.; Gill, T. E.; Cruddos, J. H.; Said, S.; Siniscalchi, M.; Narayanan, S.; Pasta, M.; Miller, T. S.; Rettie, A. J. E. Engineering Solution-Processed Non-Crystalline Solid Electrolytes for Li Metal Batteries. *Chemistry of Materials* **2023**. https://doi.org/10.1021/ACS.CHEMMATER.2C03071.

4. First author research paper on electrochemical and mechanical coupling of a Si NE solid-state battery, 2023 (submitted):

   Vadhva P, Boyce A, Patel A, Shearing P, Offer G, Rettie A. Silicon-based Solid-State Batteries: Electrochemistry and Mechanics to Guide Design and Operation. ChemRxiv. Cambridge: Cambridge Open Engage; 2023. DOI: 10.26434/chemrxiv-2023-zq6zb

Awards

1. Experimental Design Award Winner from Scientific Technology Facilities Council (STFC) - £8,000
2. Climate Change Dissemination Award Winner (best presenter at the conference) - £2,000
3. The Electrochemical Society (ECS) travel grant award recipient - $250

Internship and Training

1. Cell engineer 8-month internship at Tesla in Palo Alto, California 2022.
2. Battery consultant for Intercalation Station (part-time/freelance), working on due diligence reports for a solid-state battery company and recycling battery project and writing battery technology articles.
3. Battery Ambassador for Battery Associates, lead author on solid-state whitepaper (freelance): https://www.battery.associates/battery-whitepapers
4. Battery School WMG (Warrick University) – 1 week course learning about battery testing, manufacturing and industry and academic collaborations in UK. Run through the Faraday Institution.
5. Battery MBA – 12-week course run by Battery Associates covering battery lectures on industry and academia by experts in these areas. CPD accredited course.
6. Beamline training and experimental research at the German synchrotron (DESY) taking GI-XRD thin film measurements for pair distribution function (PDF) analysis (October 2022).
7. Training/field trip to Tokyo Institute of Technology– learning how to synthesise thin film solid electrolytes and PEs using vacuum deposition methods for 2 weeks.

References

(1) Reddy, M. v.; Mauger, A.; Julien, C. M.; Paolella, A.; Zaghib, K. Brief History of Early Lithium-Battery Development. *Materials* **2020**, *13* (8). https://doi.org/10.3390/MA13081884.

(2) Nishi, Y. Lithium Ion Secondary Batteries; Past 10 Years and the Future. *J Power Sources* **2001**, *100* (1–2), 101–106. https://doi.org/10.1016/S0378-7753(01)00887-4.

(3) Janek, J.; Zeier, W. G. A Solid Future for Battery Development. *Nat Energy* **2016**, *1* (9), 16141. https://doi.org/10.1038/nenergy.2016.141.

(4) Albertus, P.; Anandan, V.; Ban, C.; Balsara, N.; Belharouak, I.; Buettner-Garrett, J.; Chen, Z.; Daniel, C.; Doeff, M.; Dudney, N. J.; Dunn, B.; Harris, S. J.; Herle, S.; Herbert, E.; Kalnaus, S.; Libera, J. A.; Lu, D.; Martin, S.; McCloskey, B. D.; McDowell, M. T.; Meng, Y. S.; Nanda, J.; Sakamoto, J.; Self, E. C.; Tepavcevic, S.; Wachsman, E.; Wang, C.; Westover, A. S.; Xiao, J.; Yersak, T. Challenges for and Pathways toward Li-Metal-Based All-Solid-State Batteries. *ACS Energy Lett* **2021**, *6* (4), 1399–1404. https://doi.org/10.1021/ACSENERGYLETT.1C00445.

(5) Randau, S.; Weber, D. A.; Kötz, O.; Koerver, R.; Braun, P.; Weber, A.; Ivers-Tiffée, E.; Adermann, T.; Kulisch, J.; Zeier, W. G.; Richter, F. H.; Janek, J. Benchmarking the Performance of All-Solid-State Lithium Batteries. *Nat Energy* **2020**, *5* (3), 259–270. https://doi.org/10.1038/s41560-020-0565-1.

(6) Kim, K. J.; Balaish, M.; Wadaguchi, M.; Kong, L.; Rupp, J. L. M.; Kim, K. J.; Balaish, M.; Kong, L.; Rupp, L. M.; Wadaguchi, M. Solid-State Li–Metal Batteries: Challenges and Horizons of Oxide and Sulfide Solid Electrolytes and Their Interfaces. *Adv Energy Mater* **2021**, *11* (1), 2002689. https://doi.org/10.1002/AENM.202002689.

(7) Han, F.; Westover, A. S.; Yue, J.; Fan, X.; Wang, F.; Chi, M.; Leonard, D. N.; Dudney, N. J.; Wang, H.; Wang, C. High Electronic Conductivity as the Origin of Lithium Dendrite Formation within Solid Electrolytes. *Nat Energy* **2019**, *4* (3), 187–196. https://doi.org/10.1038/s41560-018-0312-z.

(8) Yoo, H. D.; Shterenberg, I.; Gofer, Y.; Gershinsky, G.; Pour, N.; Aurbach, D. Mg Rechargeable Batteries: An on-Going Challenge. *Energy Environ Sci* **2013**, *6* (8), 2265. https://doi.org/10.1039/c3ee40871j.

(9) Ping, W.; Yang, C.; Bao, Y.; Wang, C.; Xie, H.; Hitz, E.; Cheng, J.; Li, T.; Hu, L. A Silicon Anode for Garnet-Based All-Solid-State Batteries: Interfaces and Nanomechanics. *Energy Storage Mater* **2019**, *21*, 246–252. https://doi.org/10.1016/j.ensm.2019.06.024.

(10) Yue, F.; Xia, Q.; Gong, Y.; Wang, M.; Xia, H.; Huang, X. A Fully Coupled Electrochemical-Mechanical-Thermal Model of All-Solid-State Thin-Film Li-Ion Batteries. *J Power Sources* **2022**, *539*, 231614. https://doi.org/10.1016/J.JPOWSOUR.2022.231614.

(11) Shao, Y.; Shao, X.; Sang, L.; Liu, H. A Fully Coupled Mechano-Electrochemical Model for All-Solid-State Thin-Film Li-Ion Batteries with Non-Porous Electrodes: Effects of Chemo-Mechanical Expansions on Battery Performance and Optimization Strategies for Stress Evolution. *J Electrochem Soc* **2022**, *169* (8), 080529. https://doi.org/10.1149/1945-7111/AC8B3A.

(12) Zhang, W.; Schröder, D.; Arlt, T.; Manke, I.; Koerver, R.; Pinedo, R.; Weber, D. A.; Sann, J.; Zeier, W. G.; Janek, J. (Electro)Chemical Expansion during Cycling: Monitoring the Pressure Changes in Operating Solid-State Lithium Batteries. *J Mater Chem A Mater* **2017**, *5* (20), 9929–9936. https://doi.org/10.1039/C7TA02730C.

(13) Boaretto, N.; Garbayo, I.; Valiyaveettil-SobhanRaj, S.; Quintela, A.; Li, C.; Casas-Cabanas, M.; Aguesse, F. Lithium Solid-State Batteries: State-of-the-Art and Challenges for Materials, Interfaces and Processing. *Journal of Power Sources*. Elsevier B.V. August 1, 2021, p 229919. https://doi.org/10.1016/j.jpowsour.2021.229919.

(14) Tan, D. H. S.; Chen, Y.-T.; Yang, H.; Bao, W.; Sreenarayanan, B.; Doux, J.-M.; Li, W.; Lu, B.; Ham, S.-Y.; Sayahpour, B.; Scharf, J.; Wu, E. A.; Deysher, G.; Han, H. E.; Hah, H. J.; Jeong, H.; Chen, Z.; Meng, Y. S. Carbon Free High Loading Silicon Anodes Enabled by Sulfide Solid Electrolytes for Robust All Solid-State Batteries. **2021**.

(15) McGrogan, F. P.; Swamy, T.; Bishop, S. R.; Eggleton, E.; Porz, L.; Chen, X.; Chiang, Y. M.; Van Vliet, K. J. Compliant Yet Brittle Mechanical Behavior of Li2S–P2S5 Lithium-Ion-Conducting Solid Electrolyte. *Adv Energy Mater* **2017**, *7* (12), 1602011. https://doi.org/10.1002/AENM.201602011.

(16) Ke, X.; Wang, Y.; Ren, G.; Yuan, C. Towards Rational Mechanical Design of Inorganic Solid Electrolytes for All-Solid-State Lithium Ion Batteries. *Energy Storage Mater* **2020**, *26*, 313–324. https://doi.org/10.1016/J.ENSM.2019.08.029.

(17) Liu, J.; Bao, Z.; Cui, Y.; Dufek, E. J.; Goodenough, J. B.; Khalifah, P.; Li, Q.; Liaw, B. Y.; Liu, P.; Manthiram, A.; Meng, Y. S.; Subramanian, V. R.; Toney, M. F.; Viswanathan, V. v.; Whittingham, M. S.; Xiao, J.; Xu, W.; Yang, J.; Yang, X. Q.; Zhang, J. G. Pathways for Practical High-Energy Long-Cycling Lithium Metal Batteries. *Nature Energy*. Nature Publishing Group March 1, 2019, pp 180–186. https://doi.org/10.1038/s41560-019-0338-x.

(18) Gao, Z.; Sun, H.; Fu, L.; Ye, F.; Zhang, Y.; Luo, W.; Huang, Y. Promises, Challenges, and Recent Progress of Inorganic Solid-State Electrolytes for All-Solid-State Lithium Batteries. *Advanced Materials* **2018**, *30* (17), 1705702. https://doi.org/10.1002/adma.201705702.

(19) Du, M.; Liao, K.; Lu, Q.; Shao, Z. Recent Advances in the Interface Engineering of Solid-State Li-Ion Batteries with Artificial Buffer Layers: Challenges, Materials, Construction, and Characterization. *Energy Environ Sci* **2019**, *12* (6), 1780–1804. https://doi.org/10.1039/C9EE00515C.

(20) Wang, L.; Li, J.; Lu, G.; Li, W.; Tao, Q.; Shi, C.; Jin, H.; Chen, G.; Wang, S. Fundamentals of Electrolytes for Solid-State Batteries: Challenges and Perspectives. *Front Mater* **2020**, *7*, 111. https://doi.org/10.3389/FMATS.2020.00111

(21) Nie, K.; Hong, Y.; Qiu, J.; Li, Q.; Yu, X.; Li, H.; Chen, L. Interfaces Between Cathode and Electrolyte in Solid State Lithium Batteries: Challenges and Perspectives. *Front Chem* **2018**, *6*, 616. https://doi.org/10.3389/fchem.2018.00616.

(22) Fabre, S. D.; Guy-Bouyssou, D.; Bouillon, P.; Le Cras, F.; Delacourt, C. Charge/Discharge Simulation of an All-Solid-State Thin-Film Battery Using a One-Dimensional Model. *J Electrochem Soc* **2011**, *159* (2), A104–A115. https://doi.org/10.1149/2.041202jes.

(23) Pang, M.-C.; Hao, Y.; Marinescu, M.; Wang, H.; Chen, M.; Offer, G. J. Experimental and Numerical Analysis to Identify the Performance Limiting Mechanisms in Solid-State Lithium Cells under Pulse Operating Conditions. *Physical Chemistry Chemical Physics* **2019**. https://doi.org/10.1039/C9CP03886H.

(24) Cangaz, S.; Hippauf, F.; Reuter, F. S.; Doerfler, S.; Abendroth, T.; Althues, H.; Kaskel, S. Enabling High-Energy Solid-State Batteries with Stable Anode Interphase by the Use of Columnar Silicon Anodes. *Adv Energy Mater* **2020**, *10* (34), 2001320. https://doi.org/10.1002/aenm.202001320.

(25) Tian, Y.; An, Y.; Wei, C.; Jiang, H.; Xiong, S.; Feng, J.; Qian, Y. Recently Advances and Perspectives of Anode-Free Rechargeable Batteries. *Nano Energy*. Elsevier Ltd December 1, 2020, p 105344. https://doi.org/10.1016/j.nanoen.2020.105344.

(26) Baggetto, L.; Niessen, R. A. H.; Roozehoom, F.; Notten, P. H. L. High Energy Density All-Solid-State Batteries: A Challenging Concept towards 3D Integration. *Adv Funct Mater* **2008**, *18* (7), 1057–1066. https://doi.org/10.1002/adfm.200701245.

(27) Ping, W.; Yang, C.; Bao, Y.; Wang, C.; Xie, H.; Hitz, E.; Cheng, J.; Li, T.; Hu, L. A Silicon Anode for Garnet-Based All-Solid-State Batteries: Interfaces and Nanomechanics. *Energy Storage Mater* **2019**, *21*, 246–252. https://doi.org/10.1016/j.ensm.2019.06.024.

(28) Chen, C.; Oudenhoven, J. F. M.; Danilov, D. L.; Vezhlev, E.; Gao, L.; Li, N.; Mulder, F. M.; Eichel, R.-A.; Notten, P. H. L. Origin of Degradation in Si-Based All-Solid-State Li-Ion Microbatteries. *Adv Energy Mater* **2018**, *8* (30), 1801430. https://doi.org/10.1002/aenm.201801430.

(29) Reyes Jiménez, A.; Nölle, R.; Wagner, R.; Hüsker, J.; Kolek, M.; Schmuch, R.; Winter, M.; Placke, T. A Step towards Understanding the Beneficial Influence of a LIPON-Based Artificial SEI on Silicon Thin Film Anodes in Lithium-Ion Batteries. *Nanoscale* **2018**, *10* (4), 2128–2137. https://doi.org/10.1039/C7NR06568J.

(30) Tian, H.-K.; Chakraborty, A.; Talin, A. A.; Eisenlohr, P.; Qi, Y. Evaluation of The Electrochemo-Mechanically Induced Stress in All-Solid-State Li-Ion Batteries. *J Electrochem Soc* **2020**, *167* (9), 090541. https://doi.org/10.1149/1945-7111/ab8f5b.

(31) Sakabe, J.; Ohta, N.; Ohnishi, T.; Mitsuishi, K.; Takada, K. Porous Amorphous Silicon Film Anodes for High-Capacity and Stable All-Solid-State Lithium Batteries. *Communications Chemistry 2018 1:1* **2018**, *1* (1), 1–9. https://doi.org/10.1038/s42004-018-0026-y.

(32) Cras, F. le; Pecquenard, B.; Dubois, V.; Phan, V. P.; Guy-Bouyssou, D. All-Solid-State Lithium-Ion Microbatteries Using Silicon Nanofilm Anodes: High Performance and Memory Effect. *Adv Energy Mater* **2015**, *5* (19), 1501061. https://doi.org/10.1002/AENM.201501061.

(33) Vadhva, P.; Boyce, A.; Hales, A.; Pang, M.-C.; Patel, A.; Shearing, P. R.; Offer, G. J.; Rettie, A. Towards Optimised Cell Design of Thin Film Silicon-Based Solid-State Batteries via Modelling and Experimental Characterisation. *J Electrochem Soc* **2022**. https://doi.org/10.1149/1945-7111/AC9552.

(34) Di Leo, C. V.; Rejovitzky, E.; Anand, L. Diffusion–Deformation Theory for Amorphous Silicon Anodes: The Role of Plastic Deformation on Electrochemical Performance. *Int J Solids Struct* **2015**, *67–68*, 283–296. https://doi.org/10.1016/J.IJSOLSTR.2015.04.028.

(35) Bucci, G.; Talamini, B.; Renuka Balakrishna, A.; Chiang, Y. M.; Carter, W. C. Mechanical Instability of Electrode-Electrolyte Interfaces in Solid-State Batteries. *Phys Rev Mater* **2018**, *2* (10), 105407. https://doi.org/10.1103/PHYSREVMATERIALS.2.105407/FIGURES/8/MEDIUM.

(36) Bucci, G.; Swamy, T.; Chiang, Y. M.; Carter, W. C. Modeling of Internal Mechanical Failure of All-Solid-State Batteries during Electrochemical Cycling, and Implications for Battery Design. *J Mater Chem A Mater* **2017**, *5* (36), 19422–19430. https://doi.org/10.1039/C7TA03199H.

(37) Bucci, G.; Swamy, T.; Bishop, S.; Sheldon, B. W.; Chiang, Y.-M.; Carter, W. C. The Effect of Stress on Battery-Electrode Capacity. *J Electrochem Soc* **2017**, *164* (4), A645–A654. https://doi.org/10.1149/2.0371704JES/XML.

(38) Huo, H.; Sun, J.; chen, C.; Meng, X.; He, M.; Zhao, N.; Guo, X. Flexible Interfaces between Si Anodes and Composite Electrolytes Consisting of Poly(Propylene Carbonates) and Garnets for Solid-State Batteries. *J Power Sources* **2018**, *383*, 150–156. https://doi.org/10.1016/J.JPOWSOUR.2018.02.026.

(39) Miyazaki, R.; Ohta, N.; Ohnishi, T.; Sakaguchi, I.; Takada, K. An Amorphous Si Film Anode for All-Solid-State Lithium Batteries. *J Power Sources* **2014**, *272*, 541–545. https://doi.org/10.1016/J.JPOWSOUR.2014.08.109.

(40) Wu, J.; Liu, S.; Han, F.; Yao, X.; Wang, C. Lithium/Sulfide All-Solid-State Batteries Using Sulfide Electrolytes. *Advanced Materials* **2021**, *33* (6). https://doi.org/10.1002/ADMA.202000751.

(41) Latz, A.; Zausch, J. Thermodynamic Consistent Transport Theory of Li-Ion Batteries. *J Power Sources* **2011**, *196*, 3296–3302. https://doi.org/10.1016/j.jpowsour.2010.11.088.

(42) Grady, Z. A.; Wilkinson, C. J.; Randall, C. A.; Mauro, J. C. Emerging Role of Non-Crystalline Electrolytes in Solid-State Battery Research. *Front Energy Res* **2020**, *8*, 218. https://doi.org/10.3389/FENRG.2020.00218
(43) Strangmüller, S.; Eickhoff, H.; Müller, D.; Klein, W.; Raudaschl-Sieber, G.; Kirchhain, H.; Sedlmeier, C.; Baran, V.; Senyshyn, A.; Deringer, V. L.; van Wüllen, L.; Gasteiger, H. A.; Fässler, T. F. Fast Ionic Conductivity in the Most Lithium-Rich Phosphidosilicate Li14SiP6. *J Am Chem Soc* **2019**, jacs.9b05301. https://doi.org/10.1021/jacs.9b05301.
(44) Munshi, M. Z. A.; Ratnakumar, B. V.; Narayanan, S. R. Fundamental Aspects of Ion Transport in Solid Electrolytes. *Handbook of Solid State Batteries and Capacitors* **1995**, 1–40. https://doi.org/10.1142/9789812831828_0001.
(45) Famprikis, T.; Canepa, P.; Dawson, J. A.; Islam, M. S.; Masquelier, C. Fundamentals of Inorganic Solid-State Electrolytes for Batteries. *Nat Mater* **2019**. https://doi.org/10.1038/s41563-019-0431-3.
(46) Kazemi, N.; Danilov, D. L.; Haverkate, L.; Dudney, N. J.; Unnikrishnan, S.; Notten, P. H. L. Modeling of All-Solid-State Thin-Film Li-Ion Batteries: Accuracy Improvement. *Solid State Ion* **2019**, *334*, 111–116. https://doi.org/10.1016/J.SSI.2019.02.003.
(47) Glass, A. M.; Nassau, K. Lithium Ion Conduction in Rapidly Quenched Li $_2$ O-Al $_2$ O $_3$, Li $_2$ O-Ga $_2$ O $_3$, and Li $_2$ O-Bi $_2$ O $_3$ Glasses. *J Appl Phys* **1980**, *51* (7), 3756–3761. https://doi.org/10.1063/1.328164.
(48) Westover, A. S.; Kornbluth, M.; Egami, T.; Liu, J.; Kalnaus, S.; Ma, D.; Kercher, A. K.; Neuefeind, J. C.; Everett, M.; Torres, V.; Martin, S. W.; Kozinsky, B.; Dudney, N. J. Medium-Range Ordering in the Ionic Glass Electrolytes LiPON and LiSiPON. *Chemistry of Materials* **2022**. https://doi.org/10.1021/ACS.CHEMMATER.2C02380.
(49) Bates, J. B.; Dudney, N. J.; Gruzalski, G. R.; Zuhr, R. A.; Choudhury, A.; Luck, C. F.; Robertson, J. D. Electrical Properties of Amorphous Lithium Electrolyte Thin Films. *Solid State Ion* **1992**, *53–56* (PART 1), 647–654. https://doi.org/10.1016/0167-2738(92)90442-R.
(50) Fabre, S. D.; Guy-Bouyssou, D.; Bouillon, P.; le Cras, F.; Delacourt, C. Charge/Discharge Simulation of an All-Solid-State Thin-Film Battery Using a One-Dimensional Model. *J Electrochem Soc* **2011**, *159* (2), A104–A115. https://doi.org/10.1149/2.041202jes.
(51) Westover, A. S.; Dudney, N. J.; Sacci, R. L.; Kalnaus, S. Deposition and Confinement of Li Metal along an Artificial Lipon-Lipon Interface. *ACS Energy Lett* **2019**, *4* (3), 651–655. https://doi.org/10.1021/acsenergylett.8b02542.
(52) Materials Futures TOPICAL REVIEW • OPEN ACCESS. **2022**. https://doi.org/10.1088/2752-5724/ac7db2.
(53) Hatzell, K. B.; Zheng, Y. Prospects on Large-Scale Manufacturing of Solid State Batteries. *MRS Energy & Sustainability* **2021**, *8* (1), 33–39. https://doi.org/10.1557/s43581-021-00004-w.
(54) Zhang, Y.; Zheng, Z.; Liu, X.; Chi, M.; Wang, Y. Fundamental Relationship of Microstructure and Ionic Conductivity of Amorphous

LLTO as Solid Electrolyte Material. *J Electrochem Soc* **2019**, *166* (4), A515–A520. https://doi.org/10.1149/2.0161904JES/XML.

(55) Chen, R. J.; Huang, M.; Huang, W. Z.; Shen, Y.; Lin, Y. H.; Nan, C. W. Sol–Gel Derived Li–La–Zr–O Thin Films as Solid Electrolytes for Lithium-Ion Batteries. *J Mater Chem A Mater* **2014**, *2* (33), 13277–13282. https://doi.org/10.1039/C4TA02289K.

(56) Kim, J. S.; Kim, H.; Badding, M.; Song, Z.; Kim, K.; Kim, Y.; Yun, D. J.; Lee, D.; Chang, J.; Kim, S.; Im, D.; Park, S.; Kim, S. H.; Heo, S. Origin of Intergranular Li Metal Propagation in Garnet-Based Solid Electrolyte by Direct Electronic Structure Analysis and Performance Improvement by Bandgap Engineering. *J Mater Chem A Mater* **2020**, *8* (33), 16892–16901. https://doi.org/10.1039/D0TA04947F.

(57) Samson, A. J.; Hofstetter, K.; Bag, S.; Thangadurai, V. A Bird's-Eye View of Li-Stuffed Garnet-Type Li7La3Zr2O12 Ceramic Electrolytes for Advanced All-Solid-State Li Batteries. *Energy Environ Sci* **2019**, *12* (10), 2957–2975. https://doi.org/10.1039/C9EE01548E.

(58) Sastre, J.; Futscher, M. H.; Pompizi, L.; Aribia, A.; Priebe, A.; Overbeck, J.; Stiefel, M.; Tiwari, A. N.; Romanyuk, Y. E. Blocking Lithium Dendrite Growth in Solid-State Batteries with an Ultrathin Amorphous Li-La-Zr-O Solid Electrolyte. *Communications Materials 2021 2:1* **2021**, *2* (1), 1–10. https://doi.org/10.1038/s43246-021-00177-4.

(59) Raijmakers, L. H. J.; Danilov, D. L.; Eichel, R.-A.; Notten, P. H. L. An Advanced All-Solid-State Li-Ion Battery Model. *Electrochim Acta* **2020**, *330*, 135147. https://doi.org/10.1016/J.ELECTACTA.2019.135147.

(60) Sepúlveda, A.; Criscuolo, F.; Put, B.; Vereecken, P. M. Effect of High Temperature LiPON Electrolyte in All Solid State Batteries. *Solid State Ion* **2019**, *337*, 24–32. https://doi.org/10.1016/j.ssi.2019.03.023.

(61) Choi, C. H.; Cho, W. I.; Cho, B. W.; Kim, H. S.; Yoon, Y. S.; Tak, Y. S. Radio-Frequency Magnetron Sputtering Power Effect on the Ionic Conductivities of Lipon Films. *Electrochemical and Solid-State Letters* **2002**, *5* (1). https://doi.org/10.1149/1.1420926.

(62) Clayton, D. R.; Lepage, D.; Plassmeyer, P. N.; Page, C. J.; Lonergan, M. C. Low-Temperature Fabrication of Lithium Aluminum Oxide Phosphate Solid Electrolyte Thin Films from Aqueous Precursors. *RSC Adv.* **2017**, *7* (12), 7046–7051. https://doi.org/10.1039/C6RA27857D.

(63) Sakuda, A.; Hayashi, A.; Ohtomo, T.; Hama, S.; Tatsumisago, M. All-Solid-State Lithium Secondary Batteries Using LiCoO2 Particles with Pulsed Laser Deposition Coatings of Li2S–P2S5 Solid Electrolytes. *J Power Sources* **2011**, *196* (16), 6735–6741. https://doi.org/10.1016/J.JPOWSOUR.2010.10.103.

(64) Grady, Z. A.; Wilkinson, C. J.; Randall, C. A.; Mauro, J. C. Emerging Role of Non-Crystalline Electrolytes in Solid-State Battery Research. *Front Energy Res* **2020**, *8*, 218. https://doi.org/10.3389/FENRG.2020.00218

(65) Lacivita, V.; Artrith, N.; Ceder, G. Structural and Compositional Factors That Control the Li-Ion Conductivity in LiPON Electrolytes. *Chemistry of Materials* **2018**, *30* (20), 7077–7090.

https://doi.org/10.1021/ACS.CHEMMATER.8B02812/SUPPL_FILE/CM8B02812_SI_001.PDF.
(66) LaCoste, J. D.; Zakutayev, A.; Fei, L. A Review on Lithium Phosphorus Oxynitride. *Journal of Physical Chemistry C* **2021**, *125* (7), 3651–3667. https://doi.org/10.1021/ACS.JPCC.0C10001.
(67) le Van-Jodin, L.; Ducroquet, F.; Sabary, F.; Chevalier, I. Dielectric Properties, Conductivity and Li+ Ion Motion in LiPON Thin Films. *Solid State Ion* **2013**, *253*, 151–156. https://doi.org/10.1016/J.SSI.2013.09.031.
(68) Garbayo, I.; Struzik, M.; Bowman, W. J.; Pfenninger, R.; Stilp, E.; Rupp, J. L. M. Glass-Type Polyamorphism in Li-Garnet Thin Film Solid State Battery Conductors. *Adv Energy Mater* **2018**, *8* (12), 1702265. https://doi.org/10.1002/AENM.201702265.
(69) Hayashi, A.; Sakuda, A.; Tatsumisago, M. Development of Sulfide Solid Electrolytes and Interface Formation Processes for Bulk-Type All-Solid-State Li and Na Batteries. *Front Energy Res* **2016**, *4* (JUL), 25. https://doi.org/10.3389/FENRG.2016.00025
(70) Mizuno, F.; Hayashi, A.; Tadanaga, K.; Tatsumisago, M. New, Highly Ion-Conductive Crystals Precipitated from Li2S-P2S5 Glasses. *Advanced Materials* **2005**, *17* (7), 918–921. https://doi.org/10.1002/adma.200401286.
(71) Long, L.; Wang, S.; Xiao, M.; Meng, Y. Polymer Electrolytes for Lithium Polymer Batteries. *J Mater Chem A Mater* **2016**, *4* (26), 10038–10069. https://doi.org/10.1039/C6TA02621D.
(72) Zheng, F.; Kotobuki, M.; Song, S.; Lai, M. O.; Lu, L. Review on Solid Electrolytes for All-Solid-State Lithium-Ion Batteries. *J Power Sources* **2018**, *389*, 198–213. https://doi.org/10.1016/J.JPOWSOUR.2018.04.022.
(73) Fässler, T. F.; Restle, T. M. F.; Sedlmeier, C.; Kirchhain, H.; Klein, W.; Raudaschl-Sieber, G.; Deringer, V. L.; van Wüllen, L.; Gasteiger, H. A. Fast Lithium Ion Conduction in Lithium Phosphidoaluminates. *Angewandte Chemie International Edition* **2019**. https://doi.org/10.1002/anie.201914613.
(74) Lau, J.; DeBlock, R. H.; Butts, D. M.; Ashby, D. S.; Choi, C. S.; Dunn, B. S. Sulfide Solid Electrolytes for Lithium Battery Applications. *Adv Energy Mater* **2018**, *8* (27), 1800933. https://doi.org/10.1002/aenm.201800933.
(75) Pang, M.-C.; Yang, K.; Brugge, R.; Zhang, T.; Liu, X.; Pan, F.; Yang, S.; Aguadero, A.; Wu, B.; Marinescu, M.; Wang, H.; Offer, G. J. Interactions Are Important: Linking Multi-Physics Mechanisms to the Performance and Degradation of Solid-State Batteries. *Materials Today* **2021**, *49*, 145–183. https://doi.org/10.1016/J.MATTOD.2021.02.011.
(76) Krauskopf, T.; Dippel, R.; Hartmann, H.; Peppler, K.; Mogwitz, B.; Richter, F. H.; Zeier, W. G.; Janek, J. Lithium-Metal Growth Kinetics on LLZO Garnet-Type Solid Electrolytes. *Joule* **2019**, *3* (8), 2030–2049. https://doi.org/10.1016/j.joule.2019.06.013.
(77) Doux, J.; Nguyen, H.; Tan, D. H. S.; Banerjee, A.; Wang, X.; Wu, E. A.; Jo, C.; Yang, H.; Meng, Y. S. Stack Pressure Considerations for Room-Temperature All-Solid-State Lithium Metal Batteries. *Adv Energy Mater* **2020**, *10* (1), 1903253. https://doi.org/10.1002/aenm.201903253.

(78) Doux, J. M.; Yang, Y.; Tan, D. H. S.; Nguyen, H.; Wu, E. A.; Wang, X.; Banerjee, A.; Meng, Y. S. Pressure Effects on Sulfide Electrolytes for All Solid-State Batteries. *J Mater Chem A Mater* **2020**, *8* (10), 5049–5055. https://doi.org/10.1039/C9TA12889A.
(79) Sakka, Y.; Yamashige, H.; Watanabe, A.; Takeuchi, A.; Uesugi, M.; Uesugi, K.; Orikasa, Y. Pressure Dependence on the Three-Dimensional Structure of a Composite Electrode in an All-Solid-State Battery. *J Mater Chem A Mater* **2022**, *10* (31), 16602–16609. https://doi.org/10.1039/D2TA02378D.
(80) Kasemchainan, J.; Zekoll, S.; Jolly, D. S.; Ning, Z.; Hartley, G. O.; Marrow, J.; Bruce, P. G. Critical Stripping Current Leads to Dendrite Formation on Plating in Lithium Anode Solid Electrolyte Cells. *Nat Mater*. https://doi.org/10.1038/s41563-019-0438-9.
(81) Raj, V.; Aetukuri, N. P. B.; Nanda, J. Solid State Lithium Metal Batteries – Issues and Challenges at the Lithium-Solid Electrolyte Interface. *Curr Opin Solid State Mater Sci* **2022**, *26* (4), 100999. https://doi.org/10.1016/J.COSSMS.2022.100999.
(82) Nara, H.; Yokoshima, T.; Osaka, T. Technology of Electrochemical Impedance Spectroscopy for an Energy-Sustainable Society. *Current Opinion in Electrochemistry*. April 2020, pp 66–77. https://doi.org/10.1016/j.coelec.2020.02.026.
(83) Pastor-Fernández, C.; Uddin, K.; Chouchelamane, G. H.; Widanage, W. D.; Marco, J. A Comparison between Electrochemical Impedance Spectroscopy and Incremental Capacity-Differential Voltage as Li-Ion Diagnostic Techniques to Identify and Quantify the Effects of Degradation Modes within Battery Management Systems. *J Power Sources* **2017**, *360*, 301–318. https://doi.org/10.1016/j.jpowsour.2017.03.042.
(84) Choi, W.; Shin, H.-C.; Kim, J. M.; Choi, J.-Y.; Yoon, W.-S. Modeling and Applications of Electrochemical Impedance Spectroscopy (EIS) for Lithium-Ion Batteries. *Journal of Electrochemical Science and Technology* **2020**, *11* (1), 1–13. https://doi.org/10.33961/jecst.2019.00528.
(85) Orazem, M. E.; Tribollet, B. *Electrochemical Impedance Spectroscopy*; John Wiley & Sons, Inc.: Hoboken, NJ, USA, 2008. https://doi.org/10.1002/9780470381588.
(86) W.H.Mulder; Sluyters, J. H.; T.Pajkossy; L.Nylkos. Tafel Current at Fractal Electrodes Coneection with Admittance Spectra. *J.Electroanal. Chem.* **1990**, *285*.
(87) Lasia, A. Impedance of the Faradaic Reactions in the Presence of Mass Transfer. In *Electrochemical Impedance Spectroscopy and its Applications*; Springer New York: New York, NY, 2014; pp 85–125. https://doi.org/10.1007/978-1-4614-8933-7_4.
(88) Nguyen, T. Q.; Breitkopf, C. Determination of Diffusion Coefficients Using Impedance Spectroscopy Data. *J Electrochem Soc* **2018**, *165* (14), E826–E831. https://doi.org/10.1149/2.1151814jes.

(89) Cooper, S. J.; Bertei, A.; Finegan, D. P.; Brandon, N. P. Simulated Impedance of Diffusion in Porous Media. *Electrochim Acta* **2017**, *251*, 681–689. https://doi.org/10.1016/j.electacta.2017.07.152.
(90) Kraft, M. A.; Ohno, S.; Zinkevich, T.; Koerver, R.; Culver, S. P.; Fuchs, T.; Senyshyn, A.; Indris, S.; Morgan, B. J.; Zeier, W. G. Inducing High Ionic Conductivity in the Lithium Superionic Argyrodites Li6+xP1-XGexS5I for All-Solid-State Batteries. *J Am Chem Soc* **2018**, *140* (47), 16330–16339. https://doi.org/10.1021/jacs.8b10282.
(91) Woo, J. H.; Trevey, J. E.; Cavanagh, A. S.; Choi, Y. S.; Kim, S. C.; George, S. M.; Oh, K. H.; Lee, S.-H. Nanoscale Interface Modification of LiCoO 2 by Al 2 O 3 Atomic Layer Deposition for Solid-State Li Batteries . *J Electrochem Soc* **2012**, *159* (7), A1120–A1124. https://doi.org/10.1149/2.085207jes.
(92) Zhang, Z.; Chen, S.; Yang, J.; Wang, J.; Yao, L.; Yao, X.; Cui, P.; Xu, X. Interface Re-Engineering of Li10GeP2S12 Electrolyte and Lithium Anode for All-Solid-State Lithium Batteries with Ultralong Cycle Life. *ACS Appl Mater Interfaces* **2018**, *10* (3), 2556–2565. https://doi.org/10.1021/acsami.7b16176.
(93) Zhang, W.; Weber, D. A.; Weigand, H.; Arlt, T.; Manke, I.; Schröder, D.; Koerver, R.; Leichtweiss, T.; Hartmann, P.; Zeier, W. G.; Janek, J. Interfacial Processes and Influence of Composite Cathode Microstructure Controlling the Performance of All-Solid-State Lithium Batteries. *ACS Appl Mater Interfaces* **2017**, *9* (21), 17835–17845. https://doi.org/10.1021/acsami.7b01137.
(94) Cheng, L.; Crumlin, E. J.; Chen, W.; Qiao, R.; Hou, H.; Franz Lux, S.; Zorba, V.; Russo, R.; Kostecki, R.; Liu, Z.; Persson, K.; Yang, W.; Cabana, J.; Richardson, T.; Chen, G.; Doeff, M. The Origin of High Electrolyte–Electrode Interfacial Resistances in Lithium Cells Containing Garnet Type Solid Electrolytes. *Physical Chemistry Chemical Physics* **2014**, *16* (34), 18294–18300. https://doi.org/10.1039/C4CP02921F.
(95) Krauskopf, T.; Hartmann, H.; Zeier, W. G.; Janek, J. Toward a Fundamental Understanding of the Lithium Metal Anode in Solid-State Batteries - An Electrochemo-Mechanical Study on the Garnet-Type Solid Electrolyte Li 6.25 Al 0.25 La 3 Zr 2 O 12. *ACS Appl Mater Interfaces* **2019**, *11* (15), 14463–14477. https://doi.org/10.1021/ACSAMI.9B02537/ASSET/IMAGES/LARGE/AM-2019-02537N_0003.JPEG.
(96) Tan, D. H. S.; Meng, Y. S.; Jang, J. Scaling up High-Energy-Density Sulfidic Solid-State Batteries: A Lab-to-Pilot Perspective. *Joule* **2022**, *6* (8), 1755–1769. https://doi.org/10.1016/J.JOULE.2022.07.002.
(97) Han, S. Y.; Lee, C.; Lewis, J. A.; Yeh, D.; Liu, Y.; Lee, H. W.; McDowell, M. T. Stress Evolution during Cycling of Alloy-Anode Solid-State Batteries. *Joule* **2021**, *5* (9), 2450–2465. https://doi.org/10.1016/J.JOULE.2021.07.002.
(98) Fathiannasab, H.; Zhu, L.; Chen, Z. Chemo-Mechanical Modeling of Stress Evolution in All-Solid-State Lithium-Ion Batteries Using Synchrotron

Transmission X-Ray Microscopy Tomography. *J Power Sources* **2021**, *483*, 229028. https://doi.org/10.1016/j.jpowsour.2020.229028.
(99) Sitinamaluwa, H.; Nerkar, J.; Wang, M.; Zhang, S.; Yan, C. Deformation and Failure Mechanisms of Electrochemically Lithiated Silicon Thin Films. *RSC Adv* **2017**, *7* (22), 13487–13497. https://doi.org/10.1039/c7ra01399j.
(100) Herbert, E. G.; Dudney, N. J.; Rochow, M.; Thole, V.; Hackney, S. A. On the Mechanisms of Stress Relaxation and Intensification at the Lithium/Solid-State Electrolyte Interface. *J Mater Res* **2019**, *34* (21), 3593–3616. https://doi.org/10.1557/jmr.2019.313.
(101) Xie, Z.; Ma, Z.; Wang, Y.; Zhou, Y.; Lu, C.; Pharr, M.; Suo, Z.; Vlassak, J. J. Variation of Stress with Charging Rate Due to Strain-Rate Sensitivity of Silicon Electrodes of Li-Ion Batteries. *RSC Adv* **2016**, *270* (27), 569–575. https://doi.org/10.1016/j.jpowsour.2014.07.153.
(102) Bucci, G.; Nadimpalli, S. P. V.; Sethuraman, V. A.; Bower, A. F.; Guduru, P. R. Measurement and Modeling of the Mechanical and Electrochemical Response of Amorphous Si Thin Film Electrodes during Cyclic Lithiation. *J Mech Phys Solids* **2014**, *62* (1), 276–294. https://doi.org/10.1016/j.jmps.2013.10.005.
(103) Pharr, M.; Suo, Z.; Vlassak, J. J. Variation of Stress with Charging Rate Due to Strain-Rate Sensitivity of Silicon Electrodes of Li-Ion Batteries. *J Power Sources* **2014**, *270*, 569–575. https://doi.org/10.1016/j.jpowsour.2014.07.153.
(104) Wang, M.; Wang; Miao. Simulation of Amorphous Silicon Anode in Lithium-Ion Batteries. *PhDT* **2017**, 144.
(105) K A, T.-A.; Newman, J. *Electrochemical Systems*, 3rd ed.; Wiley, 2004.
(106) Sethuraman, V. A.; Srinivasan, V.; Bower, A. F.; Guduru, P. R. In Situ Measurements of Stress-Potential Coupling in Lithiated Silicon. *J Electrochem Soc* **2010**, *157* (11), A1253. https://doi.org/10.1149/1.3489378.
(107) Qiu, X.-Y.; Zhuang, Q.-C.; Zhang, Q.-Q.; Cao, R.; Ying, P.-Z.; Qiang, Y.-H.; Sun, S.-G. Electrochemical and Electronic Properties of LiCoO2 Cathode Investigated by Galvanostatic Cycling and EIS. *Physical Chemistry Chemical Physics* **2012**, *14* (8), 2617–2630. https://doi.org/10.1039/C2CP23626E.
(108) Xu, R.; Yang, Y.; Yin, F.; Liu, P.; Cloetens, P.; Liu, Y.; Lin, F.; Zhao, K. Heterogeneous Damage in Li-Ion Batteries: Experimental Analysis and Theoretical Modeling. *J Mech Phys Solids* **2019**, *129*, 160–183. https://doi.org/10.1016/J.JMPS.2019.05.003.
(109) Raijmakers, L. H. J.; Danilov, D. L.; Eichel, R. A.; Notten, P. H. L. An Advanced All-Solid-State Li-Ion Battery Model. *Electrochim Acta* **2020**, *330*, 135147. https://doi.org/10.1016/j.electacta.2019.135147.
(110) Chandrasekaran, R.; Magasinski, A.; Yushin, G.; Fuller, T. F. Analysis of Lithium Insertion/Deinsertion in a Silicon Electrode Particle at Room Temperature. *J Electrochem Soc* **2010**, *157* (10), A1139. https://doi.org/10.1149/1.3474225.

(111) Herbert, E. G.; Tenhaeff, W. E.; Dudney, N. J.; Pharr, G. M. Mechanical Characterization of LiPON Films Using Nanoindentation. *Thin Solid Films* **2011**, *520* (1), 413–418. https://doi.org/10.1016/J.TSF.2011.07.068.
(112) Koerver, R.; Zhang, W.; Biasi, L. de; Schweidler, S.; Kondrakov, A. O.; Kolling, S.; Brezesinski, T.; Hartmann, P.; Zeier, W. G.; Janek, J. Chemo-Mechanical Expansion of Lithium Electrode Materials – on the Route to Mechanically Optimized All-Solid-State Batteries. *Energy Environ Sci* **2018**, *11* (8), 2142–2158. https://doi.org/10.1039/C8EE00907D.
(113) Bloom, I.; Jansen, A. N.; Abraham, D. P.; Knuth, J.; Jones, S. A.; Battaglia, V. S.; Henriksen, G. L. Differential Voltage Analyses of High-Power, Lithium-Ion Cells: 1. Technique and Application. *J Power Sources* **2005**, *139* (1–2), 295–303. https://doi.org/10.1016/J.JPOWSOUR.2004.07.021.
(114) Dose, W. M.; Xu, C.; Grey, C. P.; de Volder, M. F. L. Effect of Anode Slippage on Cathode Cutoff Potential and Degradation Mechanisms in Ni-Rich Li-Ion Batteries. *Cell Rep Phys Sci* **2020**, *1* (11), 100253. https://doi.org/10.1016/J.XCRP.2020.100253.
(115) Seitzman, N.; Bird, O. F.; Andrykowski, R.; Robbins, S.; Al-Jassim, M. M.; Pylypenko, S. Operando X-Ray Tomography Imaging of Solid-State Electrolyte Response to Li Evolution under Realistic Operating Conditions. *ACS Appl Energy Mater* **2021**, *4* (2), 1346–1355. https://doi.org/10.1021/ACSAEM.0C02607/ASSET/IMAGES/LARGE/AE0C02607_0010.JPEG.
(116) Loveridge, M. J.; Lain, M. J.; Johnson, I. D.; Roberts, A.; Beattie, S. D.; Dashwood, R.; Darr, J. A.; Bhagat, R. Towards High Capacity Li-Ion Batteries Based on Silicon-Graphene Composite Anodes and Sub-Micron V-Doped LiFePO4 Cathodes. *Scientific Reports 2016 6:1* **2016**, *6* (1), 1–11. https://doi.org/10.1038/srep37787.
(117) Vadhva, P.; Hu, J.; Johnson, M. J.; Stocker, R.; Braglia, M.; Brett, D. J. L.; Rettie, A. J. E. Electrochemical Impedance Spectroscopy for All-Solid-State Batteries: Theory, Methods and Future Outlook. *ChemElectroChem* **2021**, *8* (11), 1930–1947. https://doi.org/10.1002/CELC.202100108.
(118) Wan, T. H.; Saccoccio, M.; Chen, C.; Ciucci, F. Influence of the Discretization Methods on the Distribution of Relaxation Times Deconvolution: Implementing Radial Basis Functions with DRTtools. *Electrochim Acta* **2015**, *184*, 483–499. https://doi.org/10.1016/J.ELECTACTA.2015.09.097.
(119) Iriyama, Y.; Kako, T.; Yada, C.; Abe, T.; Ogumi, Z. Charge Transfer Reaction at the Lithium Phosphorus Oxynitride Glass Electrolyte/Lithium Cobalt Oxide Thin Film Interface. *Solid State Ion* **2005**, *176* (31–34), 2371–2376. https://doi.org/10.1016/J.SSI.2005.02.025.
(120) Huggins, R. A. Simple Method to Determine Electronic Conductivity and Ionic Components of the Conductors in Mixed a Review. *Ionics (Kiel)* **2002**, *8* (3–4), 300–313. https://doi.org/10.1007/BF02376083.
(121) Ahmed, R.; Gazzarri, J.; Onori, S.; Habibi, S.; Jackey, R.; Rzemien, K.; Tjong, J.; Lesage, J. Model-Based Parameter Identification of Healthy and Aged Li-Ion Batteries for Electric Vehicle Applications. *SAE International*

Journal of Alternative Powertrains **2015**, *4* (2), 233–247. https://doi.org/10.4271/2015-01-0252.
(122) *Generate Parameter Data for Equivalent Circuit Battery Block - MATLAB & Simulink - MathWorks United Kingdom*. https://uk.mathworks.com/help/autoblks/ug/generate-parameter-data-for-estimations-circuit-battery-block.html (accessed 2021-10-05).
(123) Jackey, R. A.; Plett, G. L.; Klein, M. J. Parameterization of a Battery Simulation Model Using Numerical Optimization Methods. *SAE Technical Papers* **2009**. https://doi.org/10.4271/2009-01-1381.
(124) Chen, C.; Oudenhoven, J. F. M.; Danilov, D. L.; Vezhlev, E.; Gao, L.; Li, N.; Mulder, F. M.; Eichel, R. A.; Notten, P. H. L. Origin of Degradation in Si-Based All-Solid-State Li-Ion Microbatteries. *Adv Energy Mater* **2018**, *8* (30), 1801430. https://doi.org/10.1002/AENM.201801430.
(125) Lu, B.; Song, Y.; Zhang, Q.; Pan, J.; Cheng, Y.-T.; Zhang, J. Voltage Hysteresis of Lithium Ion Batteries Caused by Mechanical Stress. *Physical Chemistry Chemical Physics* **2016**, *18* (6), 4721–4727. https://doi.org/10.1039/C5CP06179B.
(126) Papakyriakou, M.; Lu, M.; Liu, Y.; Liu, Z.; Chen, H.; McDowell, M. T.; Xia, S. Mechanical Behavior of Inorganic Lithium-Conducting Solid Electrolytes. *J Power Sources* **2021**, *516*, 230672. https://doi.org/10.1016/J.JPOWSOUR.2021.230672.
(127) Han, S. Y.; Lee, C.; Lewis, J. A.; Yeh, D.; Liu, Y.; Lee, H. W.; McDowell, M. T. Stress Evolution during Cycling of Alloy-Anode Solid-State Batteries. *Joule* **2021**, *5* (9), 2450–2465. https://doi.org/10.1016/J.JOULE.2021.07.002.
(128) Nie, Z.; Ong, S.; Hussey, D. S.; Lamanna, J. M.; Jacobson, D. L.; Koenig, G. M. Probing Transport Limitations in Thick Sintered Battery Electrodes with Neutron Imaging. *Mol Syst Des Eng* **2020**, *5* (1), 245–256. https://doi.org/10.1039/C9ME00084D.
(129) Tapia-Ruiz, N.; Robert Armstrong, A.; Alptekin, H.; -, al; Zhao, X.; Lehto, V.-P. Challenges and Prospects of Nanosized Silicon Anodes in Lithium-Ion Batteries. *Nanotechnology* **2020**, *32* (4), 042002. https://doi.org/10.1088/1361-6528/ABB850.
(130) Balaish, M.; Gonzalez-Rosillo, J. C.; Kim, K. J.; Zhu, Y.; Hood, Z. D.; Rupp, J. L. M. Processing Thin but Robust Electrolytes for Solid-State Batteries. *Nature Energy 2021 6:3* **2021**, *6* (3), 227–239. https://doi.org/10.1038/s41560-020-00759-5.
(131) Schnell, J.; Knörzer, H.; Imbsweiler, A. J.; Reinhart, G. Solid versus Liquid—A Bottom-Up Calculation Model to Analyze the Manufacturing Cost of Future High-Energy Batteries. *Energy Technology* **2020**, *8* (3), 1901237. https://doi.org/10.1002/ENTE.201901237.
(132) Chen, A.; Qu, C.; Shi, Y.; Shi, F. Manufacturing Strategies for Solid Electrolyte in Batteries. *Front Energy Res* **2020**, *8*, 226. https://doi.org/10.3389/FENRG.2020.571440
(133) Clayton, D. R.; Lepage, D.; Plassmeyer, P. N.; Page, C. J.; Lonergan, M. C. Low-Temperature Fabrication of Lithium Aluminum Oxide Phosphate

Solid Electrolyte Thin Films from Aqueous Precursors. *RSC Adv* **2017**, *7* (12), 7046–7051. https://doi.org/10.1039/C6RA27857D.
(134) Joy, D. C. Scanning Electron Microscopy: Theory, History and Development of the Field Emission Scanning Electron Microscope. In *Biological Field Emission Scanning Electron Microscopy*; John Wiley & Sons, Ltd: Chichester, UK, 2019; pp 1–6. https://doi.org/10.1002/9781118663233.ch1.
(135) Seiler, H. Secondary Electron Emission in the Scanning Electron Microscope. *J Appl Phys* **1983**, *54* (11), R1–R18. https://doi.org/10.1063/1.332840.
(136) Derjaguin, B. V.; Muller, V. M.; Toporov, YU. P. Effect of Contact Deformation on the Adhesion of Elastic Solids. *J Colloid Interface Sci* **1975**, *53* (2), 314–326.
(137) Rickman, J. T.; Linton, R. W. Surface and Depth Profiling Techniques Using XPS Applied to the Study of Nickel-Containing Environmental Particles. *Appl Surf Sci* **1993**, *68* (3), 375–393. https://doi.org/10.1016/0169-4332(93)90260-I.
(138) Greczynski, G.; Hultman, L. X-Ray Photoelectron Spectroscopy: Towards Reliable Binding Energy Referencing. *Progress in Materials Science*. Elsevier Ltd January 1, 2020, p 100591. https://doi.org/10.1016/j.pmatsci.2019.100591.
(139) Seah, M. P.; Gilmore, I. S.; Spencer, S. J. Quantitative XPS: I. Analysis of X-Ray Photoelectron Intensities from Elemental Data in a Digital Photoelectron Database. *J Electron Spectros Relat Phenomena* **2001**, *120* (1–3), 93–111. https://doi.org/10.1016/S0368-2048(01)00311-5.
(140) Wenzel, S.; Sedlmaier, S. J.; Dietrich, C.; Zeier, W. G.; Janek, J. Interfacial Reactivity and Interphase Growth of Argyrodite Solid Electrolytes at Lithium Metal Electrodes. *Solid State Ion* **2018**, *318*, 102–112. https://doi.org/10.1016/J.SSI.2017.07.005.
(141) Bragg, W. *The Crystalline State*,; Macmillan: New York, 1934.
(142) De Rooi, J. J.; Van Der Pers, N. M.; Hendrikx, R. W. A.; Delhez, R.; Böttger, A. J.; Eilers, P. H. C. Smoothing of X-Ray Diffraction Data and Kα2 Elimination Using Penalized Likelihood and the Composite Link Model. *J Appl Crystallogr* **2014**, *47* (3), 852–860. https://doi.org/10.1107/S1600576714005809.
(143) Lasia, A. Electrochemical Impedance Spectroscopy and Its Applications. *Electrochemical Impedance Spectroscopy and its Applications* **2014**, *9781461489*, 1–367. https://doi.org/10.1007/978-1-4614-8933-7/COVER.
(144) Westerhoff, U.; Kurbach, K.; Lienesch, F.; Kurrat, M. Analysis of Lithium-Ion Battery Models Based on Electrochemical Impedance Spectroscopy. *Energy Technology* **2016**, *4* (12), 1620–1630. https://doi.org/10.1002/ente.201600154.
(145) Gao, Y.; Nolan, A. M.; Du, P.; Wu, Y.; Yang, C.; Chen, Q.; Mo, Y.; Bo, S. H. Classical and Emerging Characterization Techniques for Investigation of Ion Transport Mechanisms in Crystalline Fast Ionic Conductors. *Chem*

Rev **2020**, *120* (13), 5954–6008. https://doi.org/10.1021/ACS.CHEMREV.9B00747.
(146) Priya, N. S. C.; Sandhya, K.; Rajendran, D. N. Study on Electrical Conductivity and Activation Energy of Doped Ceria Nanostructures. *Electrochemical Energy Technology* **2018**, *3* (1), 49–53. https://doi.org/10.1515/EETECH-2017-0004.
(147) Wan, T. H.; Saccoccio, M.; Chen, C.; Ciucci, F. Influence of the Discretization Methods on the Distribution of Relaxation Times Deconvolution: Implementing Radial Basis Functions with DRTtools. *Electrochim Acta* **2015**, *184*, 483–499. https://doi.org/10.1016/j.electacta.2015.09.097.
(148) Reddy, C. V. K.; Rao, R. B.; Mouli, K. C.; Koti Reddy, D. V. R.; Reddy, M. V. R. Studies on Lithium Alumino Phosphate Glasses Doped with Selenium Ions for Hard Electrolytes. *J Mater Sci* **2012**, *47* (17), 6254–6262. https://doi.org/10.1007/s10853-012-6545-5.
(149) Sharma, M. V. N. V. D.; Sarma, A. V.; Balaji Rao, R. Electrical Conductivity, Relaxation, and Scaling Analysis Studies of Lithium Alumino Phosphate Glasses and Glass Ceramics. *J Mater Sci* **2009**, *44* (20), 5557–5562. https://doi.org/10.1007/s10853-009-3778-z.
(150) Moreau, F.; Durán, A.; Muñoz, F. Structure and Properties of High Li2O-Containing Aluminophosphate Glasses. *J Eur Ceram Soc* **2009**, *29* (10), 1895–1902. https://doi.org/10.1016/j.jeurceramsoc.2008.12.016.
(151) Bates, J. B.; Dudney, N. J.; Gruzalski, G. R.; Zuhr, R. A.; Choudhury, A.; Luck, C. F.; Robertson, J. D. Electrical Properties of Amorphous Lithium Electrolyte Thin Films. *Solid State Ion* **1992**, *53–56*, 647–654. https://doi.org/10.1016/0167-2738(92)90442-R.
(152) Biesinger, M. C.; Lau, L. W. M.; Gerson, A. R.; Smart, R. S. C. Resolving Surface Chemical States in XPS Analysis of First Row Transition Metals, Oxides and Hydroxides: Sc, Ti, V, Cu and Zn. *Appl Surf Sci* **2010**, *257* (3), 887–898. https://doi.org/10.1016/J.APSUSC.2010.07.086.
(153) Biesinger, M. C.; Payne, B. P.; Grosvenor, A. P.; Lau, L. W. M.; Gerson, A. R.; Smart, R. S. C. Resolving Surface Chemical States in XPS Analysis of First Row Transition Metals, Oxides and Hydroxides: Cr, Mn, Fe, Co and Ni. *Appl Surf Sci* **2011**, *257* (7), 2717–2730. https://doi.org/10.1016/J.APSUSC.2010.10.051.
(154) Kato, A.; Nagao, M.; Sakuda, A.; Hayashi, A.; Tatsumisago, M. Evaluation of Young's Modulus of Li2S-P2S 5-P2O5 Oxysulfide Glass Solid Electrolytes. *Journal of the Ceramic Society of Japan* **2014**, *122* (1427), 552–555. https://doi.org/10.2109/jcersj2.122.552.
(155) Hayashi, A.; Sakuda, A.; Tatsumisago, M. Development of Sulfide Solid Electrolytes and Interface Formation Processes for Bulk-Type All-Solid-State Li and Na Batteries. *Front Energy Res* **2016**, *4*, 25. https://doi.org/10.3389/fenrg.2016.00025.
(156) Ke, X.; Wang, Y.; Ren, G.; Yuan, C. Towards Rational Mechanical Design of Inorganic Solid Electrolytes for All-Solid-State Lithium Ion Batteries.

Energy Storage Mater **2020**, *26*, 313–324. https://doi.org/10.1016/J.ENSM.2019.08.029.
(157) Lacivita, V.; Artrith, N.; Ceder, G. Structural and Compositional Factors That Control the Li-Ion Conductivity in LiPON Electrolytes. *Chemistry of Materials* **2018**, *30* (20), 7077–7090. https://doi.org/10.1021/acs.chemmater.8b02812.
(158) Fleutot, B.; Pecquenard, B.; Martinez, H.; Letellier, M.; Levasseur, A. Investigation of the Local Structure of LiPON Thin Films to Better Understand the Role of Nitrogen on Their Performance. *Solid State Ion* **2011**, *186* (1), 29–36. https://doi.org/10.1016/j.ssi.2011.01.006.
(159) Le Van-Jodin, L.; Ducroquet, F.; Sabary, F.; Chevalier, I. Dielectric Properties, Conductivity and Li+ Ion Motion in LiPON Thin Films. *Solid State Ion* **2013**, *253*, 151–156. https://doi.org/10.1016/J.SSI.2013.09.031.
(160) Riegger, L. M.; Schlem, R.; Sann, J.; Zeier, W. G.; Janek, J. Lithium-Metal Anode Instability of the Superionic Halide Solid Electrolytes and the Implications for Solid-State Batteries. *Angewandte Chemie - International Edition* **2021**, *60* (12), 6718–6723. https://doi.org/10.1002/anie.202015238.
(161) Wan, T. H.; Ciucci, F. Electro-Chemo-Mechanical Modeling of Solid-State Batteries. *Electrochim Acta* **2020**, *331*, 135355. https://doi.org/10.1016/j.electacta.2019.135355.
(162) Weiss, M.; Seidlhofer, B. K.; Geiß, M.; Geis, C.; Busche, M. R.; Becker, M.; Vargas-Barbosa, N. M.; Silvi, L.; Zeier, W. G.; Schröder, D.; Janek, J. Unraveling the Formation Mechanism of Solid-Liquid Electrolyte Interphases on LiPON Thin Films. *ACS Appl Mater Interfaces* **2019**, *11* (9), 9539–9547. https://doi.org/10.1021/acsami.8b19973.
(163) Zhao, W.; Yi, J.; He, P.; Zhou, H. Solid-State Electrolytes for Lithium-Ion Batteries: Fundamentals, Challenges and Perspectives. *Electrochemical Energy Reviews* **2019**, 1–32. https://doi.org/10.1007/s41918-019-00048-0.
(164) Janek, J.; Zeier, W. G. Challenges in Speeding up Solid-State Battery Development. *Nature Energy 2023 8:3* **2023**, *8* (3), 230–240. https://doi.org/10.1038/s41560-023-01208-9.
(165) Schwöbel, A.; Hausbrand, R.; Jaegermann, W. Interface Reactions between LiPON and Lithium Studied by In-Situ X-Ray Photoemission. *Solid State Ion* **2015**, *273*, 51–54. https://doi.org/10.1016/j.ssi.2014.10.017.
(166) Gibson, J. S.; Narayanan, S.; Swallow, J. E. N.; Kumar-Thakur, P.; Pasta, M.; Lee, T.-L.; Weatherup, R. S. Gently Does It!: In Situ Preparation of Alkali Metal–Solid Electrolyte Interfaces for Photoelectron Spectroscopy . *Faraday Discuss* **2022**, *236*, 267–287. https://doi.org/10.1039/d1fd00118c.
(167) Wenzel, S.; Leichtweiss, T.; Krüger, D.; Sann, J.; Janek, J. Interphase Formation on Lithium Solid Electrolytes—An in Situ Approach to Study Interfacial Reactions by Photoelectron Spectroscopy. *Solid State Ion* **2015**, *278*, 98–105. https://doi.org/10.1016/J.SSI.2015.06.001.
(168) Li, Y.; Canepa, P.; Gorai, P. Role of Electronic Passivation in Stabilizing the Lithium- Li x PO y N z Solid-Electrolyte Interphase. *PRX Energy* **2022**, *1* (2). https://doi.org/10.1103/prxenergy.1.023004.

(169) Kalnaus, S.; Westover, A. S.; Kornbluth, M.; Herbert, E.; Dudney, N. J. Resistance to Fracture in the Glassy Solid Electrolyte Lipon. *J Mater Res* **2021**, *36* (4), 787–796. https://doi.org/10.1557/S43578-020-00098-X.
(170) Hänsel, C.; Kumar, P. V.; Kundu, D. Stack Pressure Effect in Li3PS4 and Na3PS4 Based Alkali Metal Solid-State Cells: The Dramatic Implication of Interlayer Growth. *Chemistry of Materials* **2020**, *32* (24), 10501–10510. https://doi.org/10.1021/ACS.CHEMMATER.0C03444/ASSET/IMAGES/MEDIUM/CM0C03444_M001.GIF.
(171) Doux, J. M.; Yang, Y.; Tan, D. H. S.; Nguyen, H.; Wu, E. A.; Wang, X.; Banerjee, A.; Meng, Y. S. Pressure Effects on Sulfide Electrolytes for All Solid-State Batteries. *J Mater Chem A Mater* **2020**, *8* (10), 5049–5055. https://doi.org/10.1039/C9TA12889A.
(172) Sakka, Y.; Yamashige, H.; Watanabe, A.; Takeuchi, A.; Uesugi, M.; Uesugi, K.; Orikasa, Y. Pressure Dependence on the Three-Dimensional Structure of a Composite Electrode in an All-Solid-State Battery. *J Mater Chem A Mater* **2022**, *10* (31), 16602–16609. https://doi.org/10.1039/D2TA02378D.
(173) Gao, X.; Liu, B.; Hu, B.; Ning, Z.; Jolly, D. S.; Zhang, S.; Perera, J.; Bu, J.; Liu, J.; Doerrer, C.; Darnbrough, E.; Armstrong, D.; Grant, P. S.; Bruce, P. G. Solid-State Lithium Battery Cathodes Operating at Low Pressures. *Joule* **2022**, *6* (3), 636–646. https://doi.org/10.1016/J.JOULE.2022.02.008.
(174) Gorai, P.; Famprikis, T.; Singh, B.; Stevanović, V.; Canepa, P. Devil Is in the Defects: Electronic Conductivity in Solid Electrolytes. *Chemistry of Materials* **2021**, *33* (18), 7484–7498. https://doi.org/10.1021/ACS.CHEMMATER.1C02345/SUPPL_FILE/CM1C02345_SI_001.PDF.
(175) Wu, B.; Chen, C.; Danilov, D. L.; Eichel, R. A.; Notten, P. H. L. All-Solid-State Thin Film Li-Ion Batteries: New Challenges, New Materials, and New Designs. *Batteries 2023, Vol. 9, Page 186* **2023**, *9* (3), 186. https://doi.org/10.3390/BATTERIES9030186.
(176) Chen, A.; Qu, C.; Shi, Y.; Shi, F. Manufacturing Strategies for Solid Electrolyte in Batteries. *Front Energy Res* **2020**, *8*, 226. https://doi.org/10.3389/FENRG.2020.571440
(177) Schnell, J.; Knörzer, H.; Imbsweiler, A. J.; Reinhart, G. Solid versus Liquid—A Bottom-Up Calculation Model to Analyze the Manufacturing Cost of Future High-Energy Batteries. *Energy Technology* **2020**, *8* (3), 1901237. https://doi.org/10.1002/ENTE.201901237.
(178) Su, Y.; Falgenhauer, J.; Polity, A.; Leichtweiß, T.; Kronenberger, A.; Obel, J.; Zhou, S.; Schlettwein, D.; Janek, J.; Meyer, B. K. LiPON Thin Films with High Nitrogen Content for Application in Lithium Batteries and Electrochromic Devices Prepared by RF Magnetron Sputtering. *Solid State Ion* **2015**, *282*, 63–69. https://doi.org/10.1016/J.SSI.2015.09.022.
(179) Lee, S.; Jung, S.; Yang, S.; Lee, J. H.; Shin, H.; Kim, J.; Park, S. Revisiting the LiPON/Li Thin Film as a Bifunctional Interlayer for NASICON Solid Electrolyte-Based Lithium Metal Batteries. *Appl Surf Sci* **2022**, *586*, 152790. https://doi.org/10.1016/J.APSUSC.2022.152790.

(180) Belous, A. G.; V'Yunov, O. I.; Kovalenko, L. L.; Bohnke, O.; Bohnke, C. Synthesis of Thin-Film Electrodes Based on LiPON and LiPON-LLTO-LiPON. *Russian Journal of Electrochemistry 2014 50:6* **2014**, *50* (6), 523–530. https://doi.org/10.1134/S1023193514060020.
(181) Su, J.; Pasta, M.; Ning, Z.; Gao, X.; Bruce, P. G.; Grovenor, C. R. M. Interfacial Modification between Argyrodite-Type Solid-State Electrolytes and Li Metal Anodes Using LiPON Interlayers. *Energy Environ Sci* **2022**, *15* (9), 3805–3814. https://doi.org/10.1039/D2EE01390H.